

**Marine Magnetotellurics
on a Continental Margin:
Imaging the Hydration and Dehydration
Cycle of the Costa Rican Subduction Zone**

Dissertation
zur Erlangung des Doktorgrades
der Mathematisch-Naturwissenschaftlichen Fakultät
der Christian-Albrechts-Universität zu Kiel

vorgelegt von
Tamara W. D. Worzewski

Kiel, März 2011

Referent:	Dr. M. Jegen-Kulcsar
Koreferent:	Prof. Dr. H. Kopp
Tag der mündlichen Prüfung:	26.05.2011
Zum Druck genehmigt:	26.05.2011

Der Dekan

Abstract

At continental margins, the water content and its distribution play an important role in the subduction process. Water is released from the subducting slab in a series of metamorphic reactions and may trigger the onset of melting, cause crustal weakening and changes in the dynamics and thermal structure of subduction zones. However, the amount of water carried into the subduction zone and its distribution are not well constrained by existing data. They are subject of vigorous current research in the special research initiative (SFB 574) at University of Kiel and IFM-GEOMAR “Volatiles and Fluids in Subduction Zones: Climate Feedback and Trigger Mechanisms for Natural Disasters”.

Electromagnetic methods like magnetotellurics have been widely used to recognize fluid release and melt production through enhanced electrical conductivities. In the framework of SFB 574, an offshore magnetotelluric experiment was performed in 2007-2008 along a profile crossing the trench, where the Cocos plate is thrust beneath the Caribbean plate. The marine profile was extended onshore by the Free University of Berlin, yielding a large-scale amphibious data set across the subduction zone with a profile length of 370 km. The main goal of the experiment is to image the fluid content and its distribution along the subducting plate and deeper Earth structure.

The recorded electromagnetic time series have been processed to electromagnetic sounding curves (apparent resistivity & phase, and Tipper) at each station. As most of the stations lay on a cliffy continental shelf, they were highly susceptible to water enforced movement (tidal currents hitting the shelf). The data quality of the recorded electromagnetic time series therefore ranges from very good to noisy, depending on the instrument’s position and stability. Only quiet sections are used for the processing. In the subsequently derived marine transfer functions a distortion due to the so-called “coast effect” is visible at specific period and distance to the coast (apexes in apparent resistivity curves occur in the transvers-electric (TE) mode, accompanied by phases wandering through all four quadrants and abnormally high Tipper values).

A detailed modeling study is performed in order to explain and quantify the coastal distortion. The modeling study reveals that the presence of a coast affects the marine transfer functions with a specific signature, which depends on several physical parameters, such as distance from the coast, period, ocean depth and bulk resistivity. Approximations are derived that define a “characteristic period” and “characteristic distance” from the coast at which the distortion is expected to be most pronounced in the transfer functions. The distortion due to the coast is shown to be helpful

as it allows the estimation of the bulk resistivity of the subsurface and furthermore increases the sensitivity of the electromagnetic response to conductivity anomalies at depth.

The recorded marine transfer functions were inverted together with the land transfer functions to an electrical resistivity model of the subduction zone down to a depth of approximately 120 km. Based on the model the hydration and dehydration cycle of a subduction zone may be derived. An electrically conductive zone in the incoming plate outer rise is associated with sea water penetrating down extensional faults and cracks into the upper mantle. Along the downward subducting plate, distinct conductive anomalies identify fluids from dehydration processes in the sediments, crust and mantle.

A conductivity anomaly at a depth of approximately 12 km and at a distance of 65 km from the trench is associated with a first major dehydration reaction of mineral-bound water. This is of importance in the context of mid-slope fluid seeps which are thought to significantly contribute to the recycling of mineral-bound water. Another fluid accumulation is revealed by a conductivity anomaly at 20-30 km depth and a distance of approximately 30 km seaward from the volcanic arc. This lower crustal fluid accumulation could likely be caused by trapping of fluids released due to de-serpentinization processes or due to other mineral dehydration processes. A comparison with other electromagnetic studies from subduction zones around the world reveal that such a conductivity anomaly is a global feature suggesting the presence of a global fluid sink. This sink may help to explain the general observed deficit between water input and output in a subduction cycle. By relating seismic evidence as well as petrological results collected in the multi-disciplinary study of Costa Rica, budget estimations for the water cycle in the subduction zone are introduced.

Zusammenfassung

Wassergehalt und -verteilung an Kontinentalrändern spielen eine fundamentale Rolle in Subduktionszonen. Die abtauchende Platte verliert in einer Reihe von metamorphen Prozessen Wasser an die Oberplatte, was die Entstehung von Schmelzen begünstigen mag, aber auch Veränderungen der Dynamik und thermalen Struktur einer Subduktionszone zur Folge haben kann. Die Wassermenge- und -verteilung innerhalb eines Subduktionssystems waren bislang eher unzureichend abgebildet worden, wurde daher zu einem der Hauptfoki des Sonderforschungsbereiches “Volatile und Fluide in Subduktionszonen: Klimarückkopplungen und Auslösemechanismen von Naturkatastrophen” (SFB 574 an der Universität zu Kiel und IFM-GEOMAR).

Elektromagnetische Methoden, wie die der Magnetotellurik, werden oft genutzt, um Fluidverteilung und Schmelzentstehung anhand von erhöhten elektrischen Leitfähigkeiten zu identifizieren. In den Jahren 2007-2008 wurde im Rahmen des SFB 574 ein marines magnetotellurisches Experiment in Costa Rica durchgeführt, wo die Cocos Platte unter die Karibische Platte abtaucht. Das marine Profil wurde durch ein Landprofil der Freien Universität (FU) Berlin erweitert, so dass ein großskaliger amphibischer Datensatz über einer Subduktionszone gewonnen werden konnte. Das Hauptziel des Experimentes lag in der Darstellung von Fluidverteilung und -inhalt entlang der subduzierenden Platte und der tieferen Erdstruktur.

Die Analyse der marinen Daten beginnt mit der Umwandlung der erfassten elektromagnetischen Zeitreihen an jeder Station zu Sondierungskurven (ausgedrückt mittels scheinbaren Widerstandes & Phase, sowie durch den Tipper). Da viele der Stationen auf dem steilen Kontinentallhang lagen, waren diese höchst anfällig für wasserbedingte Bewegungen (Gezeitenströmungen, welche auf das Kontinentalschelf treffen). So schwankt die Datenqualität der aufgezeichneten elektromagnetischen Zeitreihen von sehr gut bis sehr gestört, abhängig von der Position der Stationen bezüglich der Meeresströmungen. Letztlich sind nur ungestörte Zeitabschnitte in die Analyse eingeflossen, um Übertragungsfunktionen für die Modellierung zu erhalten.

Die berechneten marinen Übertragungsfunktionen weisen sich aufgrund des sogenannten “Küsteneffektes” als stark verzerrt aus: An bestimmter Periode und bestimmtem Abstand zur Küste tauchen ungewöhnliche Spitzen in den scheinbaren Widerstandskurven der transvers-elektrischen (TE) Mode auf; das ist begleitet durch Phasenkurven, welche durch alle vier Quadranten laufen, während auch der Tipper normale Werte bei weitem übersteigt.

Eine detaillierte Modellierungsstudie wird hierzu durchgeführt, um diese Art der Küsten-bedingten Verzerrung zu verstehen und quantifizieren. Die Modellierungsstudie

zeigt, dass die Präsenz einer Küste auf die marine Übertragungsfunktionen in einer besonderen Art und Weise einwirkt, welche die Wiedererkennung und Definition einer spezifischen Signatur erlaubt. Diese Signatur mit Wiedererkennungswert hängt von mehreren physikalischen Parametern ab, wie z.B. der Distanz zur Küste, der Periode, der Ozeantiefe und des elektrischen Untergrundwiderstandes. Es werden Näherungen hergeleitet, welche die Definition einer “charakteristischen Periode” sowie die einer “charakteristischen Distanz” zur Küste zulassen, bei welchen der Küsteneffekt die größte Verzerrung in TE mode und Tipper Übertragungsfunktionen zur Folge hat. Es wird weiterhin gezeigt, dass die größte Verzerrung durch den Küsteneffekt sich als hilfreich erweisen kann, da sich mit Hilfe dessen einerseits der Untergrundwiderstand ableiten lässt und andererseits eine Erhöhung der Sensitivität der elektromagnetischen Übertragung zur Detektion von Leitfähigkeitsanomalien auftritt.

Die aufgezeichneten marinen Übertragungsfunktionen wurden zusammen mit dem Landdatensatz invertiert, um so ein Abbild des Hydrierungs- und Dehydrierungszyklus der Subduktionszone zu erhalten. Eine elektrische Leitfähigkeitszone der abtauchenden Lithosphärenplatte noch vor dem Tiefseegraben wird als Hydrierung der Platte durch Seewasser erklärt, welches entlang von Extensions-Bruchstellen bis in den Erdmantel hinein gelangt. Entlang der subduzierten Platte werden verschiedene Leitfähigkeitsanomalien identifiziert, welche als Dehydrierungswasser von Sedimenten, Kruste und Mantel interpretiert werden.

Eine Leitfähigkeitsanomalie in ca. 12 km Tiefe und in einer Distanz von ca. 65 km landeinwärts vom Tiefseegraben wird mit ersten größeren Dehydrierungsreaktionen von Sedimentmineralen assoziiert. Dies ist im Kontext von sogenannten “Fluid seeps” auf dem Kontinentalhang von Bedeutung, da diese seeps maßgeblich am Recycling vom mineralisch gebundenem Wasser beteiligt sein sollen.

Eine weitere Fluidanhäufung wird durch eine Leitfähigkeitsanomalie in 20-30 km Tiefe und in ca. 30 km Entfernung seewärts vom Vulkanbogen identifiziert, welche allerdings nicht klar einzuordnen ist. Jedoch zeigt ein Vergleich mit anderen elektromagnetischen Studien an Subduktionszonen, dass diese Leitfähigkeitsanomalie in der ganzen Welt beobachtet wird und somit ein globales Phänomen darstellt, welches einen globalen Speicher vermuten lässt. Dieser Speicher könnte dazu beitragen, um ein generell observiertes Defizit zwischen Wasserinput und -output in der Subduktionszone zu erklären. Durch die Hinzuziehung von seismischen und petrologischen Ergebnissen der multidisziplinären Studie in Costa Rica werden letztlich Abschätzungen zum Wasserhaushalt in der Subduktionsszone vorgenommen.

Contents

Preface	1
1 Introduction	3
2 Fundamental concepts	7
2.1 Subduction zone dynamics	7
2.1.1 Subduction erosion	8
2.1.2 Tectonic framework of Costa Rica	10
2.1.3 Fluids in Subduction Zones (SFB 574)	11
2.2 Electrical Resistivity of Earth materials	13
2.2.1 Resistivity of Rocks	14
2.2.2 Archie's Law and Hashin Shtrikman bounds	14
2.3 Introduction to Natural Source EM methods: Magnetotellurics and Geomagnetic Depth Sounding	17
2.3.1 Natural signal sources in Natural source EM (MT and GDS) .	18
2.3.2 Solar activity: The ap index	19
2.3.3 From signal to transfer functions	20
2.3.4 MT transfer function: IMPEDANCE TENSOR	21
2.3.5 GDS transfer function: TIPPER	23
2.3.6 Depth penetration: SKIN DEPTH	23
2.3.7 Finding a model: Inversion of MT Response Functions	24
2.4 Previous MT studies on subduction zones	25
2.5 Marine MT Instrumentation - the first generation	27
2.5.1 Fluxgate Sensor	28
2.5.2 Digital Fluxgate Magnetometer Principle	28
2.5.3 OBMT electronics	29
2.5.4 Electric field sensors	30
2.6 Summary of Chapter 2	31
3 Data Analysis	32
3.1 From the experiment to the observed time series	34
3.2 Elimination of noise in time series	35

3.2.1	Attempts to eliminate noise	35
3.2.2	Strategy: using only quiet sections	40
3.3	Rotation of time series	41
3.3.1	Rotation to the inertial frame	41
3.3.2	Rotation to North (finding the “yaw” angle)	46
3.4	Processing of time series \Rightarrow transfer functions	47
3.4.1	Calculating impedance tensor and Tipper elements from spectra	48
3.4.2	Remote Reference	50
3.4.3	The marine transfer functions	51
3.5	Summary of Chapter 3	55
4	The coast effect on marine transfer functions	56
4.1	Abstract	56
4.2	Introduction	57
4.3	Description of the effect: The specific distortion signature in the responses	58
4.4	Why is there a minimum in the horizontal magnetic field?	60
4.5	Definition of a characteristic length and period	62
4.6	Discussion of the characteristic parameters and introduction to rules of thumb	67
4.7	Application to inversion of distorted marine data	69
4.8	Conclusions	71
5	Imaging the fluid cycle in the Costa Rican Subduction Zone	73
6	Summary - Conclusion - Outlook of thesis	102
	Acknowledgement	107
	Bibliography	113
7	Appendix	125
7.1	Technical data of the first-generation OBMT instrument	126
7.2	Table 1	128
7.3	Comments on resolution test	129
7.4	A test for Anomaly G: Blob or Line?	137
7.5	Anomaly G in other MT surveys	143
7.6	Dimensionality analysis	153
7.7	Shaking apparatus for testing motion induced noise in Viehdamm	155
	Lebenslauf	161

Preface

This thesis is a partly cumulative work which comprises introductory chapters and two independent publications, one that is in review at *Geophysical Journal International* and a published paper in *Nature Geoscience*. The thesis consists of four main parts, which are bracketed by an introduction and conclusion chapter:

The introduction chapter states the motivation and the goal of the study.

The second chapter covers the fundamental concepts on which this work is based. It covers general information on subduction zones, leading to the target area of Costa Rica. The importance of fluids in subduction zones are discussed, and the approach used to image them. The electromagnetic methods of magnetotellurics and geomagnetic depth sounding are introduced and newly developed instruments are described.

The third chapter describes the experiment and evaluates the data analysis from the time series through to the calculation of the “transfer functions”, which finally leads to the starting point of the studies given in the publications.

The fourth chapter contains the modeling study on the coast effect on the data (Worzewski and Jegen, *in review*) and introduces a new methodological approach for interpretation of marine transfer functions at continental margins.

The fifth chapter contains the published qualitative interpretation of the modeling results of the data (Worzewski et al. [2011]). Using techniques described in the previous chapters, a model is derived which displays the deep electrical conductivity distribution of the Costa Rican margin. The results are discussed and interpreted in a broader geoscientific framework and are compared to models derived at other subduction zones around the world. Also included are the online Supplementary Information, in which some technical details are discussed in detail. Additional information beyond the Supplementary Information can be found in Appendix (7.3,

7.4, 7.5, and 7.6).

The last (sixth) chapter concludes with a summary of the study and the most important discoveries from methodological and geological perspectives, providing an outlook for future investigations.

Chapter 1

Introduction

After the devastating 2010 Haiti earthquake, United Nations Secretary-General Ban Ki-moon stated: “No country is immune from disaster, be it earthquakes or floods, storms or heatwaves. (...) Many of the world’s poorest people live in high-risk densely populated cities in flood or earthquake zones, or both. The culture of disaster risk reduction must spread. (...) To prevent natural hazards turning into disasters, we must all act sooner and act smarter”¹.

Secretary-General Ban Ki-moon was appealing for disaster prevention in form of infrastructural planning, training, better public education, and advancing pre-warning systems. But prevention starts with an understanding of the processes that cause natural hazards and it is a central task of the geo-scientist to strive for deeper insight into this matter.

Most of the world’s population live in coastal regions. The largest volcanic eruptions and earthquakes occur at convergent plate boundaries, called subduction zones, where a colliding plate slides under an overriding plate transferring material to greater depths. The subducted material transported into the Earth’s interior contains free fluids in pore spaces of rocks, as well as chemically bound fluids in rock minerals (Fig. 1.1). These fluids play a key role in the emergence of natural hazards, because they may trigger earthquakes and the onset of melting, as they are squeezed out and chemically released from the subducting plate in a series of metamorphic processes. Ascending volatile-rich melts yields the power to provoke highly-explosive plinian eruptions (Wilson [1976], Sparks [1978]). As the eruption columns of such eruptions can extend high into the stratosphere, volcanic gases may be released into stratospheric layers where particle residence times are long, thus they will change the radiation budget and affect the Earth’s climate (Robock and Mao [1992], Robock

¹Source: United Nations Department of Public Information (UN/DPI). Press report of March 18th, 2010, on internet page <http://www.preventionweb.net/english/professional/news>

[2000]). Thus, the causes of natural disasters, and the changes of the Earth's climate are both connected to the flow of volatiles and fluids into and out of subduction zones.

The collaborative research center (“SonderForschungsBereich”) SFB 574 at University of Kiel and IFM-GEOMAR undertakes a multi-disciplinary analysis of these fluids and volatiles flow in subduction zones, aiming to understand trigger mechanisms for natural disasters and the complex effects on climate (one of the highest priority objectives of modern geoscience, details in paragraph 2.1.3).

In the framework of SFB 574, much has been revealed about the structure and dy-

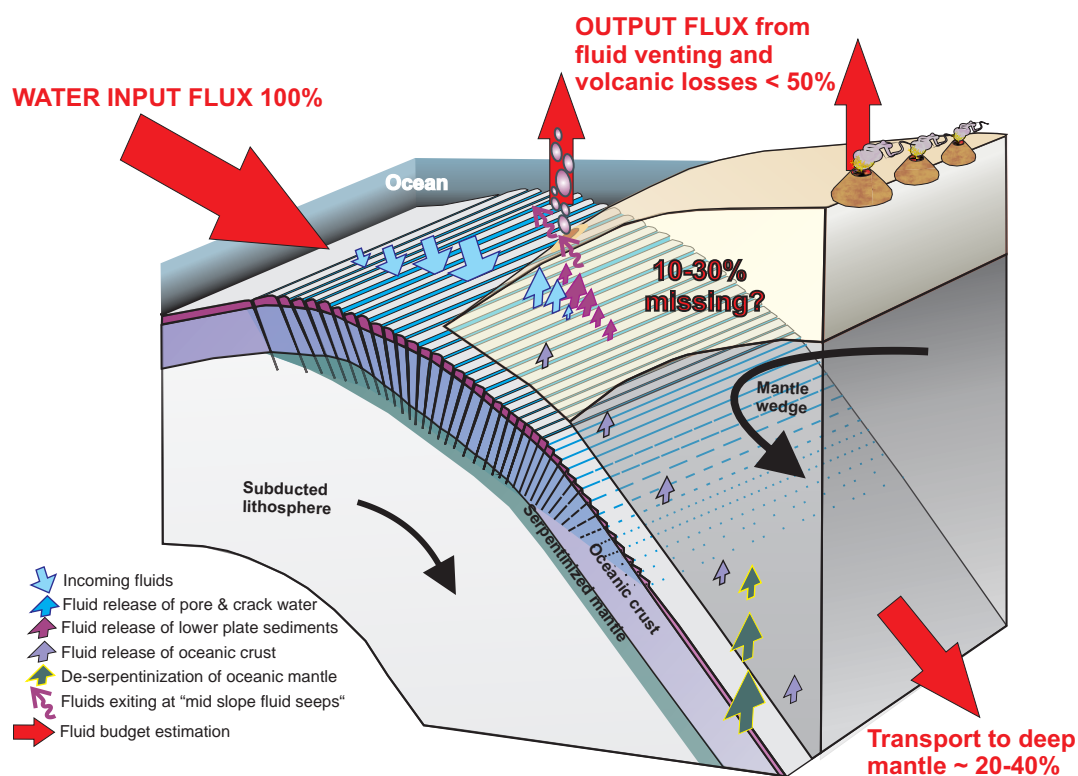


Figure 1.1: Sketch of (de-)hydration processes in subduction zones and budget estimations. A detailed discussion of this figure is given in paragraph 2.1.3.

namics of the Central American subduction zone, its fluid fluxes, and the estimations on fluid budgets. For example, Ranero et al. [2003] discovered that the incoming plate encounters an additional hydration prior to subduction by sea water that penetrates through bending related faults to mantle depths, serpentinizing crust and mantle. Water is carried into the subduction process chemically bound in minerals.

The amount of mineral bound water of the sediment and crust can be chemically derived using borehole information, whereas the amount of mineral bound water in the mantle can be quantified using seismic methods (Ivandic [2008], Ivandic et al. [2008]). This yields a measure for the total input flux into the subduction system, which is of particular interest, because it allows for budget estimations of the total water flux of a subduction zone. Such budgets (mostly globally averaged) have been published previously (e.g. Jarrard [2003]). However, recent research within the SFB 574 indicates that there is a discrepancy between the input flux and the flux leaving the subduction system through volcanic emissions, fluid venting and transportation to the deep mantle.

More precisely, output fluxes determined for forearc fluid venting and the volcanic arc emissions typically account for less than half of the input flux (S. Kutterolf and A. Freundt, pers. communication). On the other hand, Rüpke et al. [2004] determined through modeling studies that only 20% – 40% of all the chemically bound water in minerals which is entered into the subduction system can potentially be transported to great depths. These numbers indicate that 10-30 % of the incoming water is not accounted for in our current understanding of subduction zones (Fig. 1.1), which raises the questions:

Where has all the water gone? And how can we find out?

The main objective of this study which is carried out under the framework of SFB 574 is to image the fluid distribution on the Costa Rican subduction zone from the outer arc high to the volcanic front, and to interpret the results in the context of other findings, as other studies within the SFB 574 reveal where fluids are to be expected. For instance, Hensen et al. [2004] argue, from geochemical analysis, that fluids expelled at mid-slope seeps must have been produced at a minimum depth of 12 km from clay mineral dehydration processes. Modeling studies by Rüpke et al. [2004] and Rüpke et al. [2002] confirm that dehydration of sediment minerals occur at these depths, and also show that dehydration processes from crust and mantle minerals occur at greater depths, depending on the age of the subducting plate. Seismologic studies provide the tectonic and structural framework, but they do not easily image fluids. In order to image fluids, an electromagnetic technique called magnetotellurics (MT) is applied. MT is a geophysical method that complements seismic and gravity studies, by providing images of the electrical resistivity, a parameter which is particularly sensitive to the temperature and to the presence of highly conductive phases such as fluids.

In 2007-2008, an amphibious MT experiment was conducted across the Costa Rican subduction zone yielding an image of the subsurface resistivity distribution from

which conclusions regarding the fluid distribution may be drawn.

This study lends itself to tracing the journey of water to the Earth's interior and revealing where the water has gone.

However, prior to that, another more technical objective needs to be met. MT is a commonly used method on land, but there are only few publications on marine sounding curves at continental margins. The marine MT data collected offshore Costa Rica revealed extraordinarily distorted curves that would be regarded highly pathological if one were only used to land measurements. Within this study, the distortion due to the so-called "coast effect" on marine data will be investigated, gaining new methodological insight into the application and interpretation of marine MT soundings.

This study reveals how the coast affects marine responses and, surprisingly, how distortion can provide important information on geophysical parameters.

Chapter 2

Fundamental concepts

This chapter introduces the basic principles and fundamental equations which provide the framework of this study.

The first section gives an overview of subduction zones with special emphasis on Costa Rica. The important role of fluids in subduction zones is discussed on the basis of previous investigations relevant to this study. Eventually, this raises the question of how fluids may be imaged using geophysical tools.

The second section introduces the electrical properties of Earth materials, highlighting the high conductivity of fluids in comparison to almost all rock types. This implies that the electrical conductivity may be used as measuring parameter to image fluids, as is the aim of this study.

Accordingly, the third section describes the electromagnetic methods Magnetotellurics (MT) and Geomagnetic depth sounding (GDS), which are used for imaging the electric conductivities in the Earth. This section introduces and discusses the data analysis and interpretation used in the following chapters.

The fourth section provides examples of other MT studies around the world, showing that it is a common technique for probing the Earth's deep conductivity structure and imaging fluids.

The fifth section introduces the marine instrumentation that has been developed at IFM-GEOMAR and the University of Kiel, which was deployed for the electromagnetic experiment conducted in Costa Rica.

The sixth section provides an abbreviated summary of this chapter.

2.1 Subduction zone dynamics

Our Earth's surface is formed by tectonic plates that together form the lithosphere. They move at varying speeds and in different directions atop a layer of much hotter, ductile rocks, called asthenosphere. Tectonic plates move at rates of centimeters per year and they are composed of continental and/or oceanic lithosphere. The crust

forms the upper part of the lithosphere, whereas the lower portion encompasses the upper mantle. As plates move away from each other, new oceanic crust is created at mid-ocean ridges, a scenario which is referred to as seafloor spreading. The new-born oceanic crust moving away from the spreading center (or divergent margin) is formed of Layer I (the top layer consists of sediments and thickens as the plate moves away from the ridge), Layer II (basaltic layers of pillow lavas and diabase dikes) and Layer III (gabbros and cumulate ultramafic rocks formed by slow cooling of magma).

The counterpart to a divergent margin is a convergent margin where two tectonic plates move towards one another. If one of the plates is oceanic, it will slide under the other (if both are oceanic, the denser one is thrust beneath the other). This area of plate destruction is referred to as a subduction zone. Plate tectonic theory shows that the surface amount of new formed crust from divergent margins is more or less in equilibrium with the surface amount of crust disappearing at convergent margins. These processes are illustrated in Fig. 2.1.

2.1.1 Subduction erosion

For a long time it has been thought that all subduction zones have an accretionary prism, but meanwhile they are classified by two types that are distinguished by the existence or absence of a growing accretionary prism. Subduction zones where material is actively added to the overriding plate are referred to as “accretionary”, whereas subduction zones, which are characterized by removal of rock mass from the base of the overriding plate, are referred to as “erosive”. Subduction erosion mostly occurs in regions of high convergence rates and small sediment cover. In such regions sediment and/or crustal material is being recycled to the mantle affecting the rock and fluid dynamics. In contrast, accretion preferentially occurs in regions of slow convergence and comparatively thicker sedimentary layering (Clift and Vannucchi [2004]).

Generally, subduction zones create geologic formations such as mountain ranges, ocean trenches, and volcanic arcs, and they are associated with high rates of volcanism and seismicity. Fig. 2.2 exemplifies the close geographic link of subduction zones and geohazards associated with earthquakes and volcanoes. It also shows all those subduction zones that could be clearly assigned by Bilek [2010] to be of either erosive or accretionary type (other subduction zones that can not be clearly distinguished to be either of the two types are not specially marked). It is quite obvious that geohazards like earthquakes and volcanoes are inevitably linked to subduction zones.

The study area of this work is the erosive subduction zone off Costa Rica that is home to several active volcanoes and is frequently struck by strong earthquakes ($M_w \leq 7$).

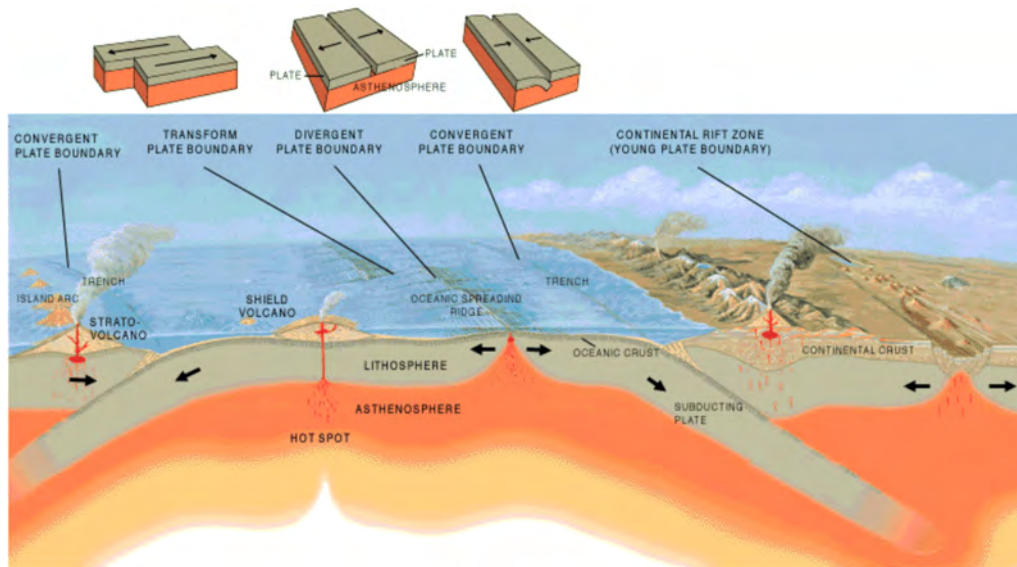


Figure 2.1: Overview of different plate tectonic boundaries, after Jose F. Vigil, USGS.

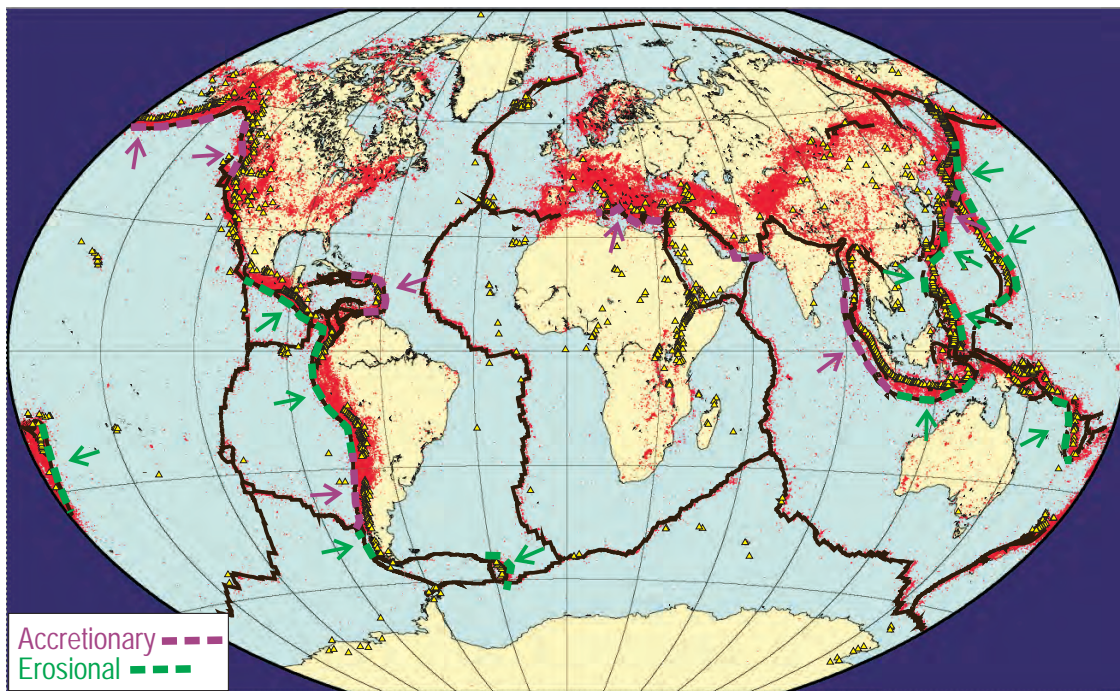


Figure 2.2: World map showing seismicity and volcanoes. Red points = earthquakes, yellow triangles = volcanoes, brown lines = plate boundaries. Dashed lines (after Bilek [2010] and Clift and Vannucchi [2004]) classify subduction zones into accretionary (purple), and erosive (green). Arrows show direction of subduction.

2.1.2 Tectonic framework of Costa Rica

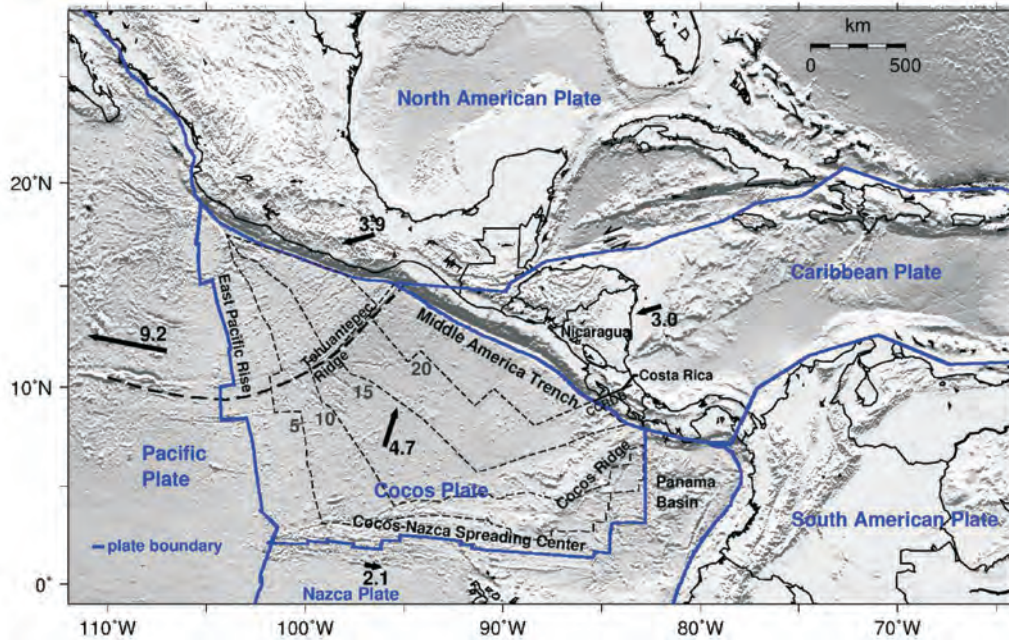


Figure 2.3: Topography map of Central America (Smith and Sandwell [1997]) and the major plate boundaries Bird [2003], modified by Berhorst [2006] and Lefeldt [2008]. Arrows indicate direction and velocity of absolute plate movement. Research presented in this thesis focuses on the Cocos Plate which is subducting at the Middle America Trench (MAT) underneath the Caribbean plate.

The Cocos plate in the North, and the Nazca plate in the South both originated 22.7 *Ma* ago from the breakup of the Farallon plate (Barckhausen et al. [2001]). Fig. 2.3 shows the tectonic framework of this study: The Cocos Plate is outlined by the East Pacific Rise (EPR) in the West, the Cocos Nazca Spreading Center (CNSC) in the South, the Panama Transform (PT) in the East, and the Middle America Trench (MAT) in the North. The EPR has a fast spreading rate of 10-12 *cm/a* (Carbotte and Macdonald [1992], Madsen et al. [1992]), which was even higher during a period from 11 – 18 *Ma* ago (at a rate of 20 *cm/a*, Wilson [1996]). These high rates led to the production of a thin, smooth and uniform crust. In contrast, the CNSC is a slow spreading ridge with a rate of 2.6 *cm/a* in the West increasing to 7.5 *cm/a* in the East (Lonsdale [1998], Allerton et al. [1996]); these differences in spreading rates cause an anti-clockwise rotation of the Cocos Plate. The comparably slow spreading rate led to the production of a rougher crust which is additionally overprinted by several seamounts, which were produced by the Galapagos hotspot.

Besides forming seamounts, the interaction between the Galapagos hotspot and the CNSC formed the so-called Cocos Ridge of approximately 100 km length and up to 200 km width, which is subducting at a wide uplifted shelf in southern Costa Rica. The subduction of aseismic ridges has been associated with the development of flat-slab segments and the cessation of arc volcanism (Vogt [1973], Pilger [1981], Nur and Ben-Avraham [1983]). While Costa Rica's volcanic arc is one of the most active in the world, there is in fact a gap in active volcanism opposite the colliding Cocos Ridge.

Owing to its rotation, the Cocos plate converges at different rates along the MAT: in the South at a rate of approximately 9 cm/a and in the North at a rate of 7 cm/a . In Costa Rica, the Cocos plate is thrust beneath the Caribbean plate at an orthogonal convergence rate of approximately 8 cm/a (DeMets [2001]). The subduction angle inferred from the Wadati-Benioff zone increases from 60° in Guatemala in the North to 80° in Nicaragua at great depths (Burbach et al. [1984]). The Wadati-Benioff zone seismicity beneath central Costa Rica shows a remarkable decrease in maximum depth toward southeastern Costa Rica (Husen et al. [2003]), where the deep subduction angle is still unknown. However, a new study using receiver function analysis indicates that the Cocos Ridge is subducting at much steeper angles than expected (Dzierma [2008]), controverting the near-horizontal underplating models (e.g. Protti et al. [1994], Protti et al. [1995]). This opens new questions on the mechanism that is responsible for shutting off volcanism. One of the possible explanations proposed by Dzierma [2008] is that the Cocos Ridge may be carrying less fluids than the faulted oceanic seafloor in the North, and thus melt processes do not occur, owing to insufficient fluid input. Another possible scenario is that this would be a temporary state in the establishment of slab subduction.

However, in northern Costa Rica, around Nicoya peninsula, in the region of this study, volcanism is still active. There, the age of the crust is 22 Ma, and the crustal thickness measures about 6 km (Walther and Flueh [2002]). More information on physical properties of the Costa Rican subduction zone are summarized in the Appendix (7.5), providing a comparison to physical parameters of other subduction zones around the world.

2.1.3 Fluids in Subduction Zones (SFB 574)

This paragraph highlights the role of fluids in subduction zones and provides a short overview on related research of the collaborative research center SFB 574 and on other investigations in this matter.

The incoming oceanic crust and lithosphere is already hydrated during its creation at mid-ocean ridges (Mével [2003]). In addition to that, another hydration process occurs. As the incoming plate approaches the trench, it bends and causes extension and normal faulting. Bathymetric and seismic investigations show that these bending related faults extend to mantle depths, and fluids are proposed to penetrate to these depths and serpentinize the crust and upper mantle (Ranero et al. [2003], Grevemeyer et al. [2005], Grevemeyer et al. [2007], Ivandic et al. [2008]). A mechanism to explain how fluids may penetrate to great depths despite their natural buoyancy has been introduced by Faccenda et al. [2009] using numerical experiments for showing how the bending of the incoming plate may produce vertical pressure gradients along normal faults which favor a “downward pumping of fluids”.

Thus, a hydrated oceanic plate enters the subduction process as sketched in Fig. 1.1: Water is carried into the subduction process as free pore water or chemically bound in minerals of sediments, crust and mantle. Fluids are partly transferred from the subducting plate into the mantle wedge and then rising upwards by magma. There, some of the fluids ascend to contribute to explosive volcanoes (Wilson [1976], Sparks [1978]). Most large earthquakes nucleate in the so-called seismogenic zone (the shearing area between the downgoing and the overriding slab), the position of which is governed by the amount of fluids present. Fluids outgassing from vents and volcanic eruptions also affect the Earth’s climate (Robock and Mao [1992], Robock [2000]). Taken together, the flow of material and fluids at subduction zones play an essential role in the generation of natural hazards.

In the last decade, a large amount of information has been gathered on Costa Rica’s subduction zone, many of the investigations have been carried out in the framework of the SFB 574. Geophysical investigations provided an overall structural framework as seismological, seismic and bathymetrical investigations have localized earthquakes, resolved the structure of the plates, mapped the sea floor, imaged the geometry of fault systems and provided insights into serpentinization (Sallarés et al. [2001], DeShon et al. [2006], DeShon and Schwartz [2004], Ranero et al. [2003], Ivandic et al. [2008], Lefeldt [2008]). Modeling studies have provided information on expected depths at which water is thought to be released, and also on the thermal structure of the subduction zone (Rüpke et al. [2002], Rüpke et al. [2004], Peacock et al. [2005]).

Borehole data provide important information on the amount of mineral bound water that enters the subduction zone (Morris and Villinger [2006], Silver et al. [2000]).

Geochemical analysis from fluids that exit at ocean seeps, and from fluid inclusions in magmatic extrusions, reveal where the fluids are coming from in terms of source depth and associated metamorphic reactions (Hensen et al. [2004], Sadofsky

et al. [2008]).

Fig. 1.1 sketches also the dehydration processes that occur at subduction zones, including findings from the research in Costa Rica. Upon subduction, the oceanic plate releases water in a series of metamorphic reactions owing to the increase of temperature and pressure with increasing depth (Rüpke et al. [2004]). Some of the water released by early metamorphic reactions finds its way up through deep-seated faults and exits at mid-slope fluid seeps which have been mapped in Costa Rica by Sahling et al. [2008]. From geochemical evidence, Hensen et al. [2004] discovered that the fluids being expelled at these seeps in Costa Rica originate at depths ≥ 12 km.

Fluid released later (and at greater depths) in the subduction process may find its way to the surface through volcanic gas emissions and magma extrusions, but an undefined fraction of water may be transported to great depths over some hundreds of kilometers (e.g. Ohtani et al. [2004], Schmidt and Poli [1998], Panero et al. [2003]). There it may join the large cycle of plate tectonics and reappear much later, recycled at newly formed crust at spreading centers (e.g. Sobolev and Chaussidon [1996]). Kelbert et al. [2009] image the likely existence of water at several hundreds of kilometers depth, though without quantification. Numerical models show that only 20% – 40% of the water input into the subduction zone can be possibly transported to such depths (Rüpke et al. [2004]). Although this work does not deal with any of the water that is being transported into the large tectonic cycle, these numbers are noted as they are used for water budget estimations discussed in Chapter 5.

The fluids being released plays a fundamental role in the origin of natural hazards. On the one hand, water triggers the onset of melting which eventually feeds the volcanoes (Wilson [1976], Sparks [1978]). On the other hand, water changes the dynamics and strength of rocks and thus can trigger earthquakes (Hacker et al. [2003], Peacock [1990], Byerlee [1993]). Much is known about these processes, yet, there are open questions, e.g. about the amount and their distribution in the Earth, raising the question: how can fluids be imaged? This will be evaluated in the next sections of this chapter.

2.2 Electrical Resistivity of Earth materials

Electrical resistivity is the reciprocal to electrical conductivity and in the community of electromagnetic depth soundings these terms are often used alternatively, depending on the focus of the target.

The electrical resistivity depends on material, conduction mechanism, fluid saturation and temperature. These properties are discussed in the following paragraphs.

2.2.1 Resistivity of Rocks

The electrical resistivity of rocks can vary by many orders of magnitude ($>100,000$ to <0.001 Ohm m); an overview is given in Fig. 2.4.

Compacted, dry, unfractured, crystalline rocks within the continental crust commonly have a high resistivity (about 1,000 to 100,000 Ωm). Regions of higher conductivity (lower resistivity) may be attributed to the presence of interconnected conductive material that is, typically, a minor component of the whole rock, but conducts electrical currents efficiently.

There are two dominant mechanisms of conduction in the Earth, the electronic conduction and the ionic conduction, which are classified by the electrical charge transport (Jones [1999]).

The electronic conduction refers to the movement of electrons. In most solids, electronic conduction is governed by the activation energy for the material, the absolute temperature and the Boltzmann constant. Electronic conduction generally occurs when interconnected graphite or sulphide or iron ores occur within a rock.

The ionic conduction refers to the movement of charged particles, i.e. ions. Ionic conduction is responsible for conduction in olivines at high temperatures, but also occurs in the presence of fluids such as partial melts along grain boundaries, water filling pore space, or intruding along fracture zones.

Measuring electrical resistivity may allow different materials and structures to be distinguished from one another and can improve knowledge of tectonic settings and geologic structures.

In particular, measurements of the Earth's resistivity distribution permits the detection of fluids, which are associated with high conductivities - one main focus of this work. So the next logical step to evaluate is how a rock's resistivity changes when it contains fluids, and how the electrical resistivity of a hydrous rock should be linked to its effective fluid content.

2.2.2 Archie's Law and Hashin Shtrikman bounds

In dry rocks, the electrical conduction is governed by electronic rather than ionic processes. The conductivity of the dry mantle increases with rising temperature, which

has been demonstrated by Constable et al. [1992] in laboratory measurements of the mantle mineral olivine. Fig. 2.5 shows that the conductivity of olivine increases by several orders of magnitude (from 10^{-6} to 10^{-3} S/m) as the temperature doubles from around 700°C to 1400°C .

In general, when a resistive rock contains free (conductive) fluids which are interconnected, ionic conduction will dominate, making the host rock more conductive. Even small amounts of fluids may increase the conductivity of the host rock by many orders of magnitude, which implies that the electrical conductivity is an important and effective physical parameter for detecting fluids. The increase in conductivity will depend on the amount of fluid in the host rock. The fluid content of a hydrous sedimentary rock may be estimated from the resistivity using Archie's empirically derived law (Archie [1942]):

$$\rho_{bulk} = a \cdot \phi^{-m} \cdot S^{-n} \cdot \rho_{fluid} \quad (2.1)$$

Archie's law relates the bulk resistivity ρ_{bulk} of a structure to its porosity fraction ϕ , fluid saturation S ($S=1$ for fully fluid saturated pores) and the resistivity of the pore fluid ρ_{fluid} . Parameters a , m and n vary depending on the cementation of the sediments. While Archie's Law is suitable for the estimation of pore fraction in sediments, the fluid-filled pore fraction in the crust may be estimated by Hashin-Shtrikman Bounds (Hashin and Shtrikman [1962]) given by

$$\sigma_{+} = \frac{\sigma_{fluid} + (\sigma_s - \sigma_{fluid})(1 - 2\phi/3)}{1 + (\phi/3)[(\sigma_s/\sigma_{fluid}) - 1]}, \quad (2.2)$$

$$\sigma_{-} = \frac{3\sigma_{fluid} + (\sigma_{fluid} - \sigma_s)(1 + 2\phi)}{(2 + \phi) + (\sigma_{fluid}/\sigma_s)(1 - \phi)} \quad (2.3)$$

where ϕ is the fluid (melt) fraction, σ_{fluid} is the conductivity of the melt and σ_s is the conductivity of the solid. Hashin Shtrikman's lower (-) and upper (+) bounds describe the limits of the effective conductivity for a two-phase (fluid and solid) isotropic material. Hashin Shtrikman bounds are based on conducting spheres in a resistive material (lower bound), and resistive spheres in a conductive material (upper bounds).

An image of the electrical conductivity distribution in the Earth can hence give information about fluid distribution and content. Electromagnetic experiments measuring the electrical conductivity distribution are therefore the method of choice for imaging water and partial melt distributions in the subsurface.

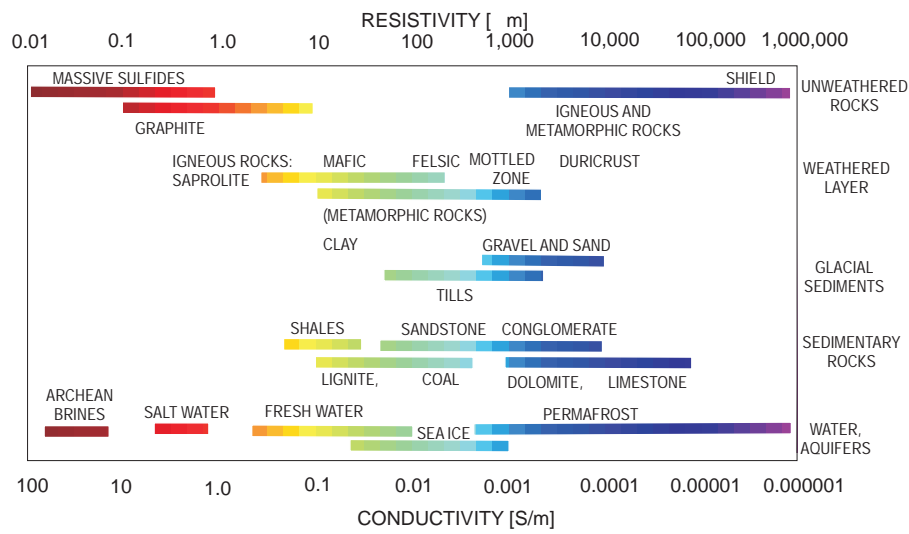


Figure 2.4: Overview of rock conductivities, modified from Palacky [1987].

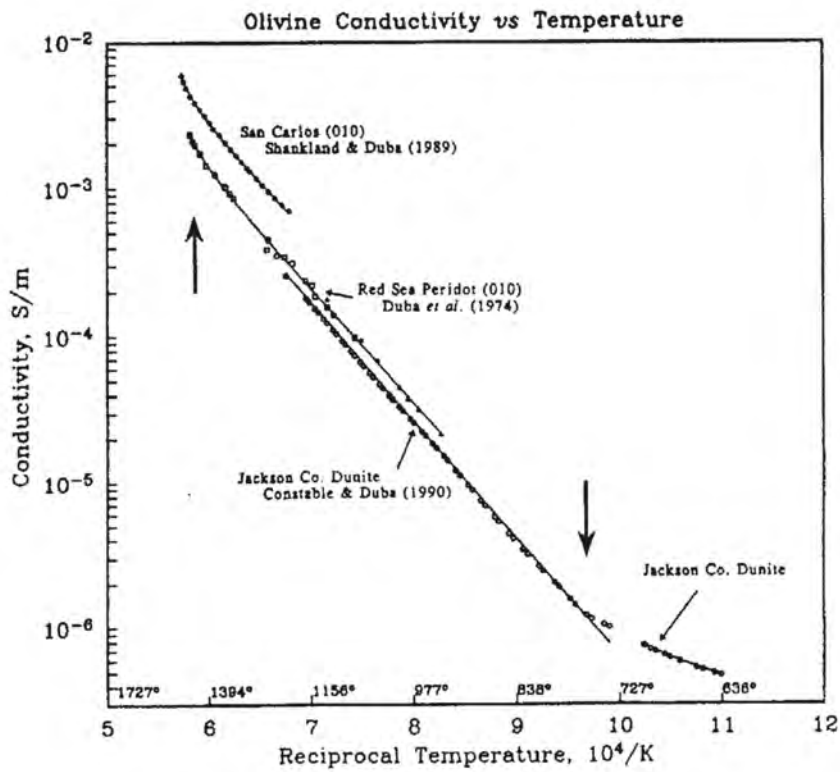


Figure 2.5: Laboratory measurement of electrical conductivity of olivine vs. temperature from Constable and Duba [1990].

2.3 Introduction to Natural Source EM methods: Magnetotellurics and Geomagnetic Depth Sounding

Out of the numerous electromagnetic (EM) methods, there are only a few techniques that allow for the probing of the electrical conductivity structure of the Earth down to depths of some hundreds of kilometers: Magnetotellurics (MT) and Geomagnetic Depth Sounding (GDS). The MT technique was introduced by the French geophysicist Louis Cagniard and the Russian geophysicist A. N. Tikhonov in the early 1950s (Cagniard [1953], Tikhonov [1950]). Since then, advances in instrumentation, processing and modeling, have made MT a very important tool in deep Earth research. These techniques use naturally-occurring electromagnetic field fluctuations as source signals. The following paragraphs introduce the basic theory of the MT and the GDS techniques; a short overview on practical applications is presented in Section 2.4.

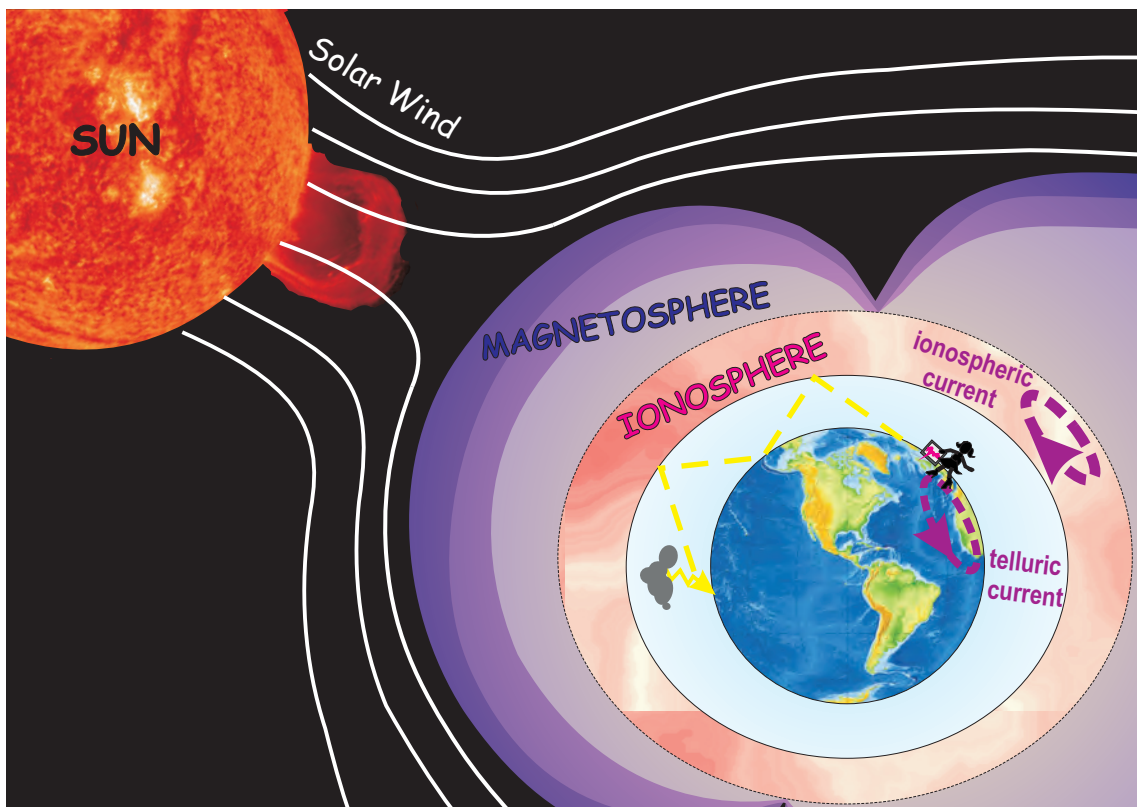


Figure 2.6: Schematic of MT source signals.

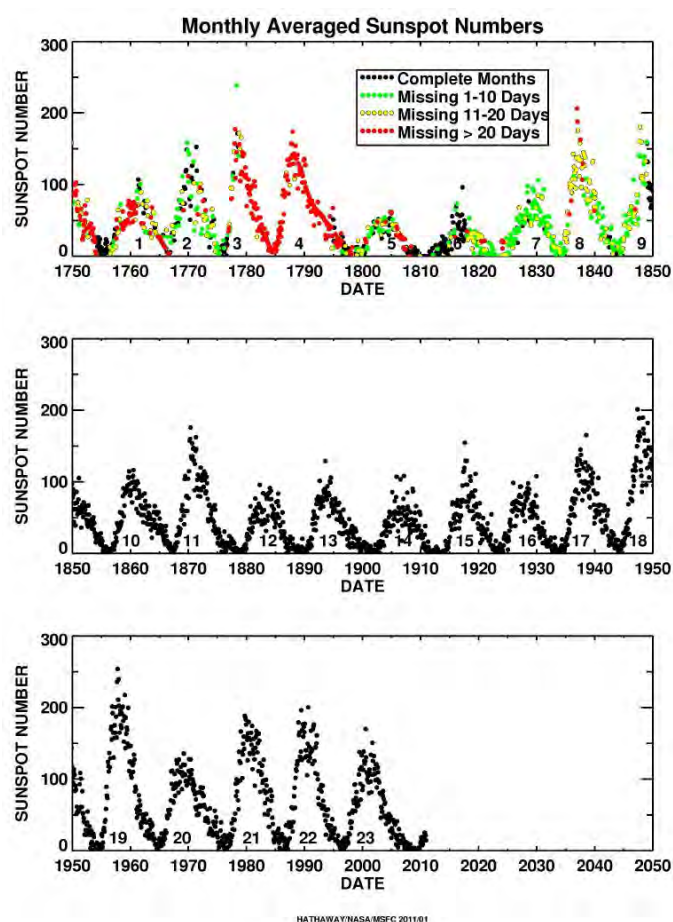


Figure 2.7: 11-year solar cycle of sunspot numbers. Last minimum was observed around 2007-2008 (see bottom panel). Source: NASA (<http://solarscience.msfc.nasa.gov>).

2.3.1 Natural signal sources in Natural source EM (MT and GDS)

The Earth's magnetic field is encompassed by a region defined as the magnetosphere. The magnetosphere has an oval tear-drop shape which results from the solar wind plasma interacting with the Earth's intrinsic magnetic field. The magnetosphere includes our atmosphere, which one can sub-classify under different aspects concerning different physical properties. Concerning electrical properties, the atmosphere is classified into neutrosphere and ionosphere. The neutrosphere is defined by a shell from the Earth's surface upward, in which the atmospheric constituent parts are mostly un-ionized, i.e. electrically neutral. The neutrosphere is electrically resistive. The part of the atmosphere above the neutrosphere is ionized by solar ra-

diation, contains plasma and is therefore electrically conductive. In a plasma, the negative free electrons and the positive ions are attracted to each other by the electromagnetic force, but they are too energetic to stay fixed together in an electrically neutral molecule. This ionized portion of the upper atmosphere is referred to as the ionosphere. The region of transition between the neutrosphere and the ionosphere is somewhere around 50-100 km above the Earth's surface, depending on daytime, season and latitude.

MT and GDS use electromagnetic field fluctuations which are generated by two sources, schematically illustrated in Fig. 2.6. One is the interaction of the Earth's magnetic field with the solar wind (charged particles emitted from the sun), which results in fluctuations in the magnetosphere that are transferred to the ionosphere in terms of large scale currents. The magnetic field variations resulting from this interaction typically contain frequencies below 1 Hz (i.e. periods >1 s).

The other source arises from global lightning activity in a lower part of the atmosphere (the troposphere). Lightning strikes emit electromagnetic energy that becomes trapped within the waveguide defined by the neutrosphere (the non-conducting space between the conducting Earth's surface and the conducting ionosphere). The electromagnetic radiation resonates around the planet resulting in the enhancement of certain frequencies which are referred to as "atmospherics" or just "spherics" and cause variations in the magnetic field typically exceeding 1 Hz (i.e. periods < 1 s).

At the Earth's surface, the total magnetic field vector is measured as a superposition of the large static primary field with an intensity in the order of $\approx 10^4$ nT, and the much smaller solar and atmospheric signals, which typically fluctuate around values in the order of $\approx 10^{-1} - 10^2$ nT. However, since the primary field can be regarded static during the MT/GDS experiment, the signals can be clearly distinguished from the primary field.

For the experiment in this thesis, mainly solar signals are used (periods greater than 1 s).

2.3.2 Solar activity: The ap index

The lower frequencies of magnetic field variations (below 1 Hz) that are generated by the interaction of Earth's magnetosphere and solar wind are related to the sunspot activity, which varies over several periodic time-scales. The principle periodic component of solar activity variation is the 11-year solar cycle which had its last minimum during the years around 2007-2008, as displayed in Fig. 2.7 (bottom panel). The sunspot activity is associated with solar flares (and resultant coronal mass ejections) that expel plasma traveling outwards from the sun and interacting with the

Earth’s magnetic field, which eventually governs the source signal strength and quality for MT and GDS measurements. Geomagnetic disturbances can be monitored by ground-based magnetic observatories recording the three magnetic field components. The global “Kp” index is obtained as the mean value of the disturbance levels in the two horizontal field components, observed at 13 selected, subauroral stations (the name Kp originates from the German expression “*planetarische Kennziffer*” = planetary index). Kp and related indices such as ap, Ap, and Cp are widely used in ionospheric and magnetospheric studies and are generally recognized as indices measuring worldwide geomagnetic activity. The three-hour index “ap” is directly related to the Kp index in a linear scale and ranges from zero (no magnetic activity at all) to 400 (magnetic storms). The ap index will be used in Section 3.2.2 to review the measured signals in terms of source quality.

2.3.3 From signal to transfer functions

The electromagnetic (EM) signals from such extremely large-scale sources behave, in the first approximation, like plane waves at the Earth’s surface as they propagate vertically into the Earth. These EM signals induce secondary electric currents in the Earth, which are referred to as “telluric” currents (from latin: *tellus*=Earth, the eponym for Magneto-tellurics). Their strength depend on the conductivity of the subsurface. Through measurements of the two horizontal components of the electric and the three orthogonal components of the magnetic field variations, frequency dependent transfer functions may be derived, which are dependent on the conductivity of the Earth only (independent of the source signal). The theoretical derivation is thoroughly described for an example in Vozoff [1991], and Simpson and Bahr [2005].

The reduction, including the removal of biasing effects, of the measured time series to a transfer function is referred to as “processing”. The recorded time series for the horizontal components of the electric and magnetic fields and the vertical magnetic field components are Fourier transformed and robustly band-averaged into transfer function estimates vs. frequency (period, respectively). Details on the processing of the time series will be presented in the context of data analysis in Section 3.4.

In this work two types of transfer functions are used:

One is the transfer function accounting for MT relates the horizontal electric field fluctuations to the horizontal magnetic ones, called the “impedance tensor $\underline{\mathbf{Z}}$ ”.

And the other is the transfer function accounting for GDS that relates the horizontal magnetic field fluctuations to the vertical one, called “Tipper \mathbf{T} ”. These transfer functions are used to derive a subsurface resistivity model.

2.3.4 MT transfer function: IMPEDANCE TENSOR

The impedance tensor $\underline{\underline{Z}}$ is complex valued, frequency dependent, and independent of the source field. It relates the measured horizontal electric field \vec{E} to the measured horizontal magnetic field components \vec{H} .

$$\begin{pmatrix} E_x(\omega) \\ E_y(\omega) \end{pmatrix} = \begin{pmatrix} Z_{xx}(\omega) & Z_{xy}(\omega) \\ Z_{yx}(\omega) & Z_{yy}(\omega) \end{pmatrix} \cdot \begin{pmatrix} H_x(\omega) \\ H_y(\omega) \end{pmatrix}, \quad (2.4)$$

where $\omega = 2\pi/T$ is the angular frequency and T is the period.

The abbreviated form is given by:

$$\vec{E}(\omega) = \underline{\underline{Z}}(\omega) \cdot \vec{H}(\omega). \quad (2.5)$$

The magnetic field \vec{H} has the unit $[\frac{A}{m}]$, \vec{E} has the unit $[\frac{V}{m}]$, and the impedance tensor has the unit ‘‘Ohm’’ $= \frac{V}{A} = [\Omega]$. It should be noted that magnetic variations are normally measured in nT which is the unit of the magnetic induction \vec{B} . As a result, it occurs quite often in literature that the transfer function between \vec{B} and \vec{E} is calculated as

$$\vec{E}(\omega) = \underline{\underline{\hat{Z}}}(\omega) \cdot \vec{B}(\omega), \quad (2.6)$$

where $\underline{\underline{\hat{Z}}}$ has the unit of a velocity and nevertheless is often referred to as impedance tensor, although the actual impedance (as given in Eq. 2.5) ought to have the unit Ohm, which sometimes leads to confusion. The relationship between these values is given by:

$$\vec{B} = \mu_0 \vec{H} \quad (2.7)$$

and therefore

$$\underline{\underline{Z}} = \mu_0 \underline{\underline{\hat{Z}}}, \quad (2.8)$$

where $\mu_0 = 4\pi \cdot 10^{-7} \frac{Vs}{Am}$ is the magnetic permeability of the vacuum.

The impedance tensor exhibits certain characteristics depending on the dimensionality of the resistivity distribution of the ground:

- For a simple layered resistivity model (1D case), diagonal elements are equal to zero and off-diagonal elements differ only in their sign ($Z_{xx} = Z_{yy} = 0$ and $Z_{xy} = -Z_{yx}$).
- For a 2D resistivity model, Maxwell’s Equations decouple into two sets of equations. One set describes currents flowing along the structure, which is referred to as E-polarization or TE mode, and the other set describes currents flowing across the structure, which is referred to as B-polarization or TM mode. When the tensor is rotated into strike direction, as illustrated in Fig. 2.8, the diagonal elements become zero and off-diagonal elements yield two independent

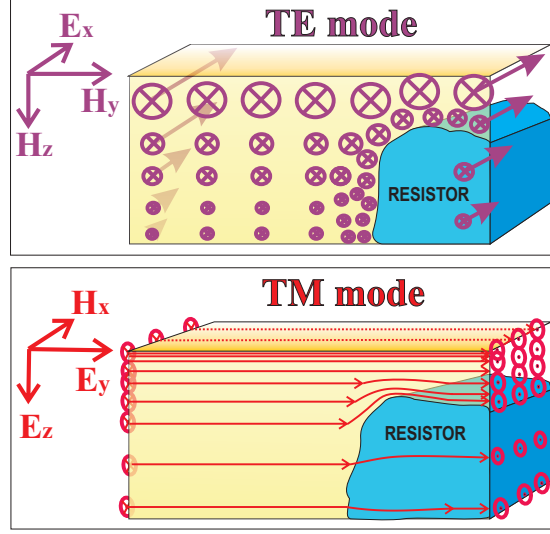


Figure 2.8: TE and TM mode, decoupled EM field components in a 2D Earth. Arrows indicate naturally induced telluric (electric) currents flowing along or perpendicular to the geologic strike direction. The electric current flow depends on the conductivity distribution; a resistivity contrast causes measurable changes of the electromagnetic fields at the surface.

measurements for the underlying resistivity structure. Thus $Z_{xx} = Z_{yy} = 0$ and $Z_{xy} \neq Z_{yx}$. Under ideal conditions the impedance tensor may be used to determine the strike direction by rotating the impedance tensor to that angle at which diagonal elements are minimized, i.e.

$$\underline{\underline{Z}}_{2D}(\omega) = \underline{\underline{R}}(\alpha_s) \cdot \underline{\underline{Z}}_{\text{obs}}(\omega) \cdot \underline{\underline{R}}^T(\alpha_s), \quad (2.9)$$

where $\underline{\underline{R}}(\alpha)$ is the rotation matrix, $\underline{\underline{R}}^T(\alpha)$ is the transpose, α_s is the strike angle at which $\|Z_{xx} + Z_{yy}\| \neq \min$.

- For a 3D Earth, all impedance tensor elements are non-zero and defer from each other.

The impedance tensor is normally visualized by its amplitude and phase which are expressed by the apparent resistivity and phase. For the element Z_{xy} the apparent resistivity $\rho_{a,xy}$ is calculated by:

$$\rho_{a,xy}(\omega) = \frac{1}{\omega} |Z_{xy}(\omega)|^2 \quad (2.10)$$

with the unit $[\Omega m]$.

The phase difference between \vec{E} - and \vec{H} -field is calculated through the argument of

Z:

$$\varphi_{xy}(\omega) = \arctan \frac{\Im(Z_{xy}(\omega))}{\Re(Z_{xy}(\omega))} \quad (2.11)$$

and is calculated in an analogous way for $\rho_{a,yx}(\omega)$ und $\varphi_{yx}(\omega)$.

2.3.5 GDS transfer function: TIPPER

The GDS transfer function is derived from the magnetic field components. The so-called Tipper \vec{T} relates the horizontal magnetic fields to the vertical magnetic field:

$$H_z(\omega) = T_x(\omega) \cdot H_x(\omega) + T_y(\omega) \cdot H_y(\omega) \quad (2.12)$$

Like the impedance tensor, the Tipper is complex valued and independent of the source signal. The Tipper is indicative for 2D-conductivity structures: For a 2D Earth, and in the correct coordinate system as illustrated in Fig. 2.8, $T_x = 0$, and T_y depends on the the conductivity contrast. For a 1D Earth, the Tipper vanishes ($T_x = T_y = 0$).

The Tipper is less commonly used, however, it provides important additional information to the impedance tensor.

2.3.6 Depth penetration: SKIN DEPTH

An electromagnetic signal travelling through a conductive medium undergoes energy absorption which depends on its frequency. Horizontal resolution of MT mainly depends on the distance between sounding locations - closer spacing of sounding locations increases the horizontal resolution.

The depth of penetration of the MT signal is linked to its frequency and the conductivity of the materials into which it is penetrating. Vertical resolution decreases as depth of investigation increases. The skin depth δ is defined as the depth in the Earth at which the incident amplitudes of electric and magnetic waves have been reduced to $1/e$ ($\approx 37\%$) of their surface strength. In a homogeneous half-space, the skin depth is given by

$$\delta = \sqrt{\frac{2}{\omega \mu_0 \sigma}} \approx 0.5 \sqrt{\rho T}. \quad (2.13)$$

δ is measured in $[km]$, the period T measured in $[s]$, σ is the conductivity which is the reciprocal of resistivity ρ measured in $[S/m]$ ($\sigma = 1/\rho$).

The skin depth δ at a station defines the induction space; in case of a homogeneous background the induction space is given by a half sphere of radius δ , which then determines the area in which induced fields can be measured.

On land, the broad spectrum of natural electromagnetic signals can be measured as introduced in Paragraph 2.3.1. But at the seafloor, the recorded spectrum of signals is limited due to the absorbing effect of the ocean. The ocean is highly conductive with an average conductivity of 3 S/m (= a resistivity of 0.33 Ωm) and dampens effectively high frequency (low period) signals. As a consequence, electromagnetic signals at high frequencies are very small at ocean bottom inhibiting resolution of shallower sea-bottom features. Only signals with periods large enough to reach the seafloor are valuable. Inserting the average ocean resistivity into Eq. 2.13, and solving for the period T, yields an estimate for the minimum period T_{min} at a given ocean depth d_o that can be used for evaluation of subseafloor structures:

$$T_{min} \approx 12 \cdot d_o^2, \quad (2.14)$$

where T is yielded in [s], when $[d_o]$ is inserted into this approximation with the unit of [km].

2.3.7 Finding a model: Inversion of MT Response Functions

After the calculation of transfer functions, a resistivity model of the Earth is sought via an inversion process. An inversion is a procedure in which an assumed model is progressively changed in order to fit the measured data and a-priori knowledge under given special constraints. The inversion requires a forward operator, which is capable of computing the data one would observe, given as assumed model parameterization thought to describe the real resistivity distribution of the Earth.

Let \vec{d} be a data vector consisting of n data points $\vec{d} = (d_1, \dots, d_n)^T$, where superscript “T” denotes the transpose. Then, let the Earth be represented by a model parameter vector \vec{m} containing information on electrical resistivity structure. As an example, in the 1D case, the structure information is given by k horizontal layers of thicknesses l_k , so the model vector is expressed by $\vec{m} = (\rho_1, \dots, \rho_k, l_1, \dots, l_k)^T$. Further, let the forward operator be a function f . In the ideal case, the forward calculation $f(\vec{m})$ equals the measured data \vec{d} . However, in reality, no model will exactly reproduce real measured data. The misfit between model measured data is normally defined by the rms (root mean square) that is generally defined by:

$$rms = \sqrt{\frac{(\vec{d} - f(\vec{m}))^T R_{dd}^{-1} (\vec{d} - f(\vec{m}))}{n}}, \quad (2.15)$$

where R_{dd} = data error covariance matrix.

The observed data, with their errors, and an a priori model, together comprise the input parameters for the inversion process. Within the inversion process, the

rms misfit is sought to be minimized to a tolerance level due to the non-linearity of the forward function f . The inversion is an iterative procedure to stabilize the inversion smoothing constraints in the model space. In general, minimizing the model complexity (increasing the smoothness) has the opposite effect to fitting the measured data as well as possible: minimizing data misfit will maximize the model roughness. Therefore, a compromise between these values must be found that regulates the trade off between model smoothness and data misfit.

There are many different inversion schemes. Here, only a standard inversion scheme will be described which is used in the work presented here. An established inversion scheme for MT data is Tikhonov's method (Tikhonov [1965], Tikhonov and Arsenin [1979]), which defines a regularized solution as the model that minimizes the objective function:

$$S(\vec{m}) = (\vec{d} - f(\vec{m}))^T R_{dd}^{-1} (\vec{d} - f(\vec{m})) + \tau \|L(\vec{m} - m_0)\|^2, \quad (2.16)$$

where L is a stabilizer called roughness operator or regularization functional, m_0 = a priori model, τ = regularization parameter that determines the trade off between model smoothness and data misfit.

In this work, the 2D MT modeling/inversion package WinGLink from Geosystems is used for the derivation of the resistivity model described in Chapter 5. The package is based on an algorithm published by Rodi and Mackie [2001]. The inversion is based on the Tikhonov scheme using the Laplacian operator $L = \Delta$ with $\|L(m - m_0)\|^2 = \int (\Delta(m(r) - m_0(r)))^2 dr$ as the regularization functional.

2.4 Previous MT studies on subduction zones

Magnetotellurics (MT) has been widely used to investigate the conductivity distribution of the crust and mantle aiming at a better understanding of plate-tectonic processes and fluid imaging. Commercial uses include

- hydrocarbon exploration (e.g. Hoversten et al. [1998], Constable et al. [1998b], Constable et al. [1998a]),
- geothermal exploration (e.g. Hoffmann-Rothe et al. [2001], Ingham and Reeves [1993], Monteiro Santos et al. [1995]),
- mining exploration (e.g. Tuncer et al. [2006], Jones and Craven [2004], Oldenburg [2002]), and
- groundwater monitoring (e.g. Pedersen et al. [2005]).

The MT method has been used to image geologic structures on land since the 1950s (Vozoff [1972]) and in the ocean since the 1980s (reviews on marine MT studies are given in Law [1983], Constable [1990], Heinson and Constable [1992], Palshin [1996] and Baba [2005]). Since fluids are very conductive in comparison to other Earth materials (Section 2.2), MT is popularly used for detecting fluid zones in active tectonic settings. Examples of such studies are “fluids in the Tibetan crust” (Wei et al. [2001]), “fluids at intraplate earthquake zones in Japan” (Ogawa et al. [2001]), or fluid zones at several other plate boundaries (Jiracek et al. [2007]).

Several subduction zones in the world have been studied with MT revealing conductivity anomalies associated with fluids. Land experiments have been carried out in the subduction zones of Argentina (Booker et al. [2004]), Cascadia (Jiracek et al. [1989], Soyer and Unsworth [2006]), Chile (Brasse et al. [2002], Schwalenberg et al. [2002]), Greece (Galanopoulos et al. [2005]), Indonesia (Hoffmann-Rothe et al. [2001]), Japan (Ichiki et al. [2000]), New Zealand (Heise et al. [2007], Wannamaker et al. [2002], Wannamaker et al. [2009]), and Mexico (Joedicke et al. [2007]). Also, a marine survey over a subduction zone was conducted in Japan (Shimakawa and Honkura [1991]). However, numerical studies showed that both land and marine data are essential to infer electrical conductivities in the offshore and onshore regime of the subduction zone (Evans et al. [2002]), so these MT surveys so far did not provide a complete image of the (de-) hydration processes.

In the 1980s, a pioneering amphibious project, called EMSLAB, was conducted across the Cascadia subduction zone, which at the time was the largest electromagnetic study incorporating land and marine measurements. While one of the first MT 2D-inversions was performed for the land data (Jiracek et al. [1989]), the marine data was evaluated by trial-and-error forward modeling (Wannamaker et al. [1989]). The EMSLAB project revealed important information on the electrical properties of subduction zones, however, due to large station spacing on the marine side, no information of the offshore region around the trench and continental slope could be provided in detail.

One novelty of the amphibious experiment presented in this work is the combined inversion of land and marine MT data over a subduction zone that has a station spacing dense enough to resolve for structures which are small in comparison to the profile length. The results of the amphibious experiment in Costa Rica are presented in Chapter 5. As few marine EM instruments exist worldwide, only few amphibious experiments on subduction zones have been carried out since the EMSLAB project besides the experiment presented here: The FU Berlin conducted a study of the Chilean margin (Brasse et al. [2009a]) and Scripps and Woodshole Oceanographic

Institute investigated the Nicaraguan margin¹.

Some of the published MT studies on subduction zones mentioned above focus on the very deep structure of subduction zones reaching several hundreds of kilometers deep. The experiments are designed on a very large scale with station spacings too wide to resolve smaller scale structures (e.g. Booker et al. [2004]). Other experiments only focus on the very near surface resistivity distribution (e.g. Hoffmann-Rothe et al. [2001]). Subduction zone experiments which are comparable to the one presented here will be discussed in Chapter 5 and also in the Appendix (7.5).

Since the EMSLAB project in the late 1980s, instrumentation was further improved to permit a better resolution of resistivity structures through increased measurement precision. For the experiment presented here, new instruments were developed, which are presented in the next section 2.5.

2.5 Marine MT Instrumentation - the first generation

During the last years, new instruments have been developed at IFM-GEOMAR and University of Kiel, which have been extensively tested and improved during several measurement campaigns. However, for the electromagnetic experiment conducted in Costa Rica, only the first generation of instruments was used, which is described in this section. The instrument measures the natural temporal geomagnetic and geoelectric field variations in a period range from $T = 0.2$ s to DC (possible sampling rates are 10Hz, 5Hz, 1Hz and 1/60Hz.). The OBMT-System (Ocean Bottom MagnetoTelluric System) is constructed similar to ocean bottom seismometers from IFM-GEOMAR (Bialas and Flüh [1999]). The recording instrument inside the titanium cylinder is designed and constructed by MAGSON GmbH and contains:

- a three component fluxgate magnetometer,
- two E-field channels for recording the electric field in two components,
- a dual axes tilt meter for measuring pitch and roll, and
- a temperature sensor.

The instrument is equipped with an internal data logger with a temperature controlled clock for instrument control and data storage on compact flash cards.

¹The marine data are currently being evaluated in the framework of other PhD theses, the analysis in Chile is performed by Gerhard Kapinos (FU Berlin, Germany) and the one in Nicaragua by Samer Vaif (Scripps).

The OBMT-System is a free falling system with a non-magnetic anchor made of aluminum and concrete to avoid distortion of data due to induction effects. It is released from the seafloor through an acoustic release system. The instrument in total weighs around 400 kg including the anchor (≈ 300 kg without anchor) in air, and approximately 30 kg in water. A photo of the instrument during deployment is shown in Fig. 2.9.

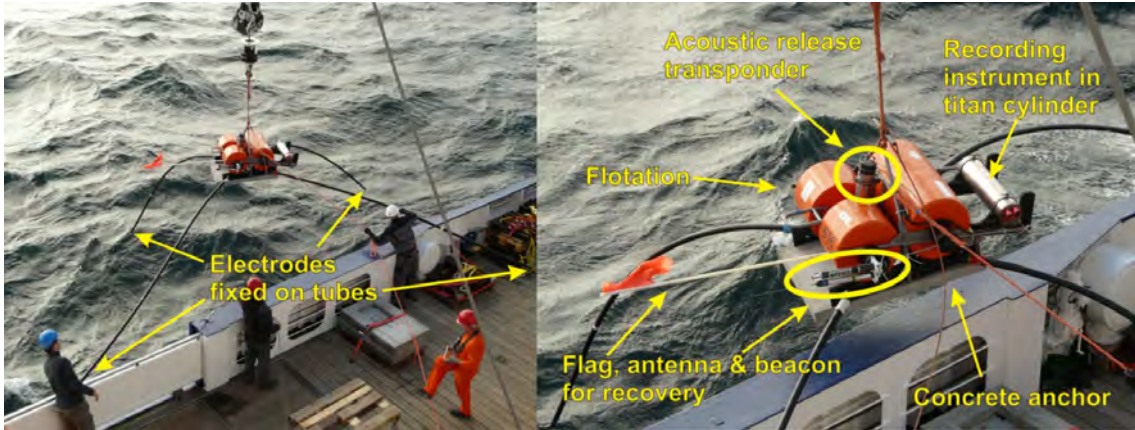


Figure 2.9: Picture of OBMT instrument from IFM-GEOAMR during deployment.

2.5.1 Fluxgate Sensor

The magnetic field is measured with a vector compensated ringcore fluxgate sensor which has been developed and is used for planetary magnetic field measurements on satellite missions. It consists of two crossed ringcores, three pick-up coils and a tri-axial Helmholtz coil system for field feedback, which are used to null out the static magnetic field to increase the dynamic range of the magnetic field variation measurement. Scale values and non-orthogonality depend only on stability of the feedback coil system. Because of stable temperature conditions on sea floor, the use of the three component mini sensor without additional support materials is feasible. The thermal expansion coefficient of the feedback coil system is about $24\text{ppm}/^\circ\text{C}$. The noise level of the ringcores is in the order of $10\text{pT}/\sqrt{\text{Hz}}$ at 1Hz.

2.5.2 Digital Fluxgate Magnetometer Principle

The main property of the digital fluxgate magnetometers is the direct digitization of the second harmonic of the excitation frequency, which contains the magnetic field information. Filters and phase-sensitive demodulators are not used. Analog-to-digital conversion close to the sensor reduces the amount of analogue parts, which

often cause drift problems or show deviations in the component values, and it highly increases the robustness against environmental influences (e.g. temperature change and electromagnetic disturbances).

These considerations lead to the design of mainly digital sensor electronics. First, the sensor output signal is amplified by an instrumentation amplifier. Next, it is digitized by a 16-bit analogue-to-digital converter exactly in the minimum and maximum of the second harmonic of the excitation frequency. The FPGA (Field Programmable Gate Array) calculates the difference between both measurements and stores the result in an accumulator. This measurement will be repeated for a programmable number of excitation periods. A FPGA internal RISC (Reduced Instruction Computer) processor calculates from the accumulated ADC (Analog/Digital Converter) values and the last set DAC (Digital/Analog Converter) feedback value the magnetic field value, transmits the results to the data logger and calculates a new set of DAC feedback values.

The feedback system is driven by two 16bit DA-Converters for each component, the first one to compensate the Earth's field and the second one to operate the sensor in a reduced range. Therefore two measurement modes are available. The full range mode covers the whole Earth's magnetic field range and the variometer mode works in a limited range of +/-2000nT.

The reason to separate the field compensation into coarse and fine range is the differential nonlinearity (DLN) of the DA-Converter. Reduced operation range in variometer mode guarantees that nonlinearity is smaller than the resolution. Using a higher internal sampling rate and cascaded DA-Conversion, the resulting dynamic range corresponds to 24bit. The resolution on the background of the Earth's field is still 10pT.

2.5.3 OBMT electronics

The electronics consists of magnetometer electronics, electric (\vec{E} -) field measurement, tilt and temperature measurement, data logger, and a high precision temperature controlled clock board. \vec{B} - and \vec{E} - field will be measured in time synchrony, triggered by the 1Hz signal of the clock board. The internal data acquisition rate is 100Hz. Dependent on the selected storage frequency, data output as well as system time, inclination, temperature and instrument status are stored on the flash disk. Furthermore, data logging and instrument control with an external unit is possible via RS232.

Optionally, a time table may be programmed to determine settings of mode, sam-

pling rate and format for any time chosen. This option allows, for example, a broadband recording at shallower depth from high frequent sampling in the beginning switching automatically to long period measurements saving disk space and battery.

2.5.4 Electric field sensors

Electric field fluctuations are determined by measuring the potential difference (U) between pairs of electrodes, which are connected via shielded cables to form a dipole and fixed in the water column nearby the ground at known distances (d) of about 10 m apart: $E = U/d$. In this system we use four unpolarizable Ag-AgCl electrodes for probing the electric field (2x two dipoles). Two dipoles are required in order to ascertain the two horizontal components of the electric field. They are configured orthogonal to each other being fixed to four tubes of each 5 m length, which yields a distance of 10 m per electrode pair (see Fig. 2.9).

Further information on technical details is provided in the appendix (7.1).

2.6 Summary of Chapter 2

- In Costa Rica, the Cocos Plate is thrust beneath the Caribbean Plate forming an erosive subduction zone, which is characterized by high input flux rate of material that is carried into the Earth's interior.
- Natural hazards at convergent margins are linked to the presence of fluids. The aim of this work is to image the fluid distribution in a subduction setting.
- The resistivity of rocks varies over many orders of magnitude - fluids are very conductive in comparison to the solid matrix of a rock and determine the bulk resistivity of a rock.
- The resistivity of a rock can be related to its fluid content using Archie's law or Hashin Shtrikman bounds.
- MT and GDS are natural source electromagnetic techniques that measure the resistivity distribution in the Earth, and therefore can be used for imaging and quantifying fluids.
- For seafloor measurements, EM signals with periods exceeding 1 s may be recorded.
- The source signal induces a secondary frequency dependent field in the Earth. At the surface both fields, primary and secondary, are measured over time yielding electromagnetic time series.
- "Transfer functions" in the frequency domain are derived from the time series, which are independent of the source field and contain the information about the resistivity distribution in the Earth.
- The transfer function of MT, called "impedance tensor", may be expressed through apparent resistivity and phase curves. The GDS transfer function, called "Tipper", can be expressed by its real and imaginary components.
- Many MT surveys have been carried out at subduction zones, but since they were mostly bound either to an exclusively onshore or an exclusively marine environment, they lack information on the entity of the subduction processes. The large-scale amphibious study presented here is aimed to provide insights on subduction processes.
- New instruments were developed at IFM-GEOMAR and University of Kiel for the seafloor MT and GDS experiment.

Chapter 3

Data Analysis

Marine MT instruments constructed at IFM-GEOMAR and University of Kiel (Section 2.5) were used in Central America to conduct an offshore marine MT experiment which was complemented onshore by the FU Berlin in 2007-2008. Eleven marine stations recorded electromagnetic fields at the ocean bottom. Simultaneously, one onshore station near the coast line recorded the magnetic field at the surface. The recordings are used to derive marine transfer functions, which are eventually needed for modeling the subsurface resistivity distribution.

While MT measurements on land must be carried out in remote places in order to minimize human/urban noise, such electrical distortions practically do not exist at the ocean bottom. Yet, unexpectedly strong water currents in the vicinity of the shelf can destabilize the seafloor instruments. A magnetometer moving by only 0.1 degree from the horizontal produces a pronounced artificial signal in the magnetic time series, which is explained with the following example: Let the static total magnetic field vector have a magnitude of 35,000 nT while its direction may be expressed by only two components (one in the horizontal direction pointing to North, and one directed vertically to depth, whereas there is no partition in the East component). Let the natural inclination of the static total field vector be 20° from the horizontal, then a magnetometer with sensors aligned to the geomagnetic coordinate system would record a projected value of $35,000 \cdot \cos(20^\circ)$ nT on its horizontal sensor (and $35,000 \cdot \sin(20^\circ)$ nT on its vertical sensor, respectively). If the magnetometer position is now displaced by 0.1° from the horizontal, the resulting registration in the (changed) inclined coordinate system records $35,000 \cdot \cos(20 \pm 0.1^\circ)$ nT at the former horizontal sensor (and $35,000 \cdot \sin(20 \pm 0.1^\circ)$ nT at the former depth sensor, respectively). The difference between the sensor's registration in the two slightly different coordinate systems measures $\approx \pm 20$ nT ($\approx \pm 57$ nT, respectively). These values range in the order of natural signals at the time of the recording.

However, in this context one must distinguish between a static displacement (mean averaged tilt over time) and any periodic movement (shaking) of the instrument. A displacement static in time poses no problems to calculate correct impedances as a static tilt may be easily removed from the data, which is discussed in Section 3.3. But if the sensor was periodically shaking and constantly changing the coordinate system for the measurement of the static field, this would produce an artificial signal in the measured time series. Such motion induced noise is obviously not related to any natural electromagnetic induction effect, an integration of such “false” signals would lead to the calculation of incorrect impedances. Thus, motion induced noise poses a problem.

The fact that noisy data was acquired in Costa Rica eventually led to the devel-

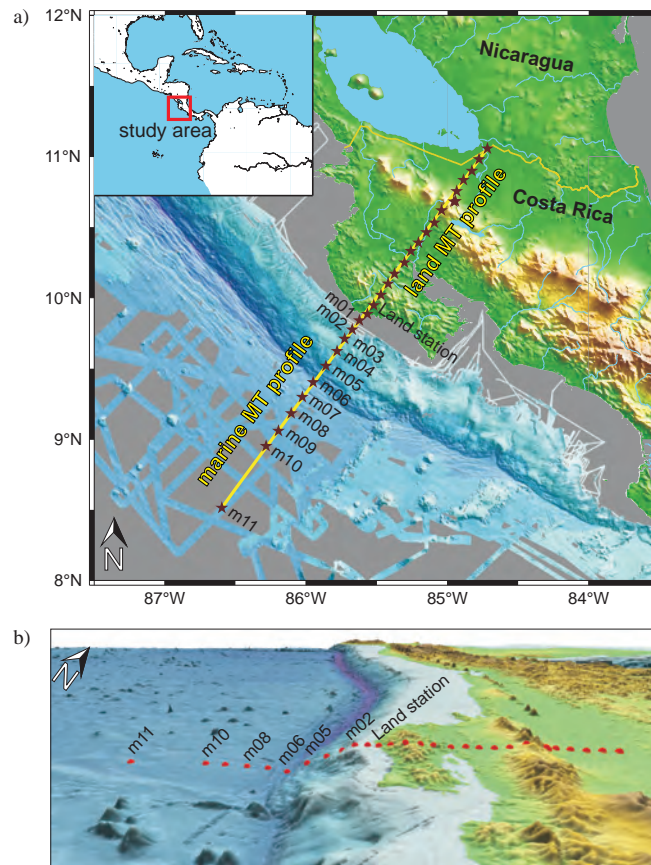


Figure 3.1: Upper panel: Station map of amphibious MT profile. Land profile was acquired by FU Berlin. Lower panel displays a side view (vertically exaggerated by factor 5). Bathymetric data were kindly provided by Wilhelm Weinrebe, pers. communication.

opment of a second generation of OBMT instruments. Among other improvements, the second generation instrument is much more stable to withstand strong water forces. However, one of the challenges of the present work was to extract reasonable transfer functions from the noisy data recorded.

Fig. 3.1 a shows the amphibious MT profile across the Costa Rican subduction zone. The onshore profile acquired by the FU Berlin was analyzed by Brasse et al. [2009b]. As most of the marine stations were positioned on a clifty continental shelf (Fig. 3.1b), they were highly susceptible to water current and wave induced movement. Data quality therefore ranges from good to extremely noisy depending on the instrument's position and tilt variations due to ocean currents. In particular, stations m05, m04, m03 and m01 were exposed to increased levels of water currents and wave induced movement, and station m02 was lost. The following sections will take the reader through the whole procedure from the observation of time series in varying quality to the calculation of transfer functions:

Section 3.1 shows the recorded timeseries and introduces the problematic noise in the data. Section 3.2.2 deals with the elimination of the problematic noise. After the elimination of noise, the data must be rotated into a geomagnetic coordinate frame which is described in Section 3.3. The subsequent data processing for deriving transfer functions is presented in Section 3.4. Last but not least, a very unusual shape of the derived transfer functions caused by the so-called ‘‘coast effect’’, and investigated in more detail in the following Chapter 4.

3.1 From the experiment to the observed time series

Most of the noise can be tracked back to water induced movement of the instrument as tiltmeter registration shows. The tiltmeter inside the OBMT instrument (Section 2.5) measures the displacement from the horizontal in two components based on the movement of air bubbles in two orthogonal levels attached to the magnetometer. The inclination of the instrument is registered simultaneously with the electromagnetic field (same sampling rate), so any instrument shaking and the resulting effect on the magnetic field is sensed.

Fig. 3.2 shows, as an example, a section of noisy time series of marine station m05, placed on clifty shelf. Panels a), b) and c) display magnified sections of different time lengths (ten days, two days and nine hours of recording, respectively). Each panel displays: the three orthogonal components of the magnetic field (B_1, B_2, B_3), two components of the electric field (E_1, E_2) and the dual axis tiltmeter registration (t_x, t_y). The influence of water motion on MT registration is visible in several frequency bands. Tidal movement is the dominant signature in registrations of tilt

and magnetic field (noise that appears every few hours and lasts for several hours). However, throughout the full four month long time series of station m05, several small sections with several hours length can be identified in which the instrument did not move - an important point for further evaluation, which will be discussed further later.

The complete magnetic field registration has periodical motion dominating over natural variations at all frequencies (see power spectra in Fig. 3.3 a). The tiltmeter data tracks that tidal waves occur near lunar frequencies ($l_2 \approx 6$ h), and other currents which are often aligned to temperature variations (currents are mostly driven by temperature changes). However, there are natural signals clearly visible in magnetic field components, which have no signature in the tiltmeter registration. For an example, the reader is referred to the daily variation ($Sq = 24$ h) in Fig. 3.3 b or its third harmonic ($sq3 = 8$ h) in Fig. 3.3 a (both outlined by red dashed circles).

In order to derive an electromagnetic transfer function, the extraction of signal without motion induced noise constituted the first step in the data processing sequence as discussed in the following Section 3.2.2.

3.2 Elimination of noise in time series

From the inspection of time series (Fig. 3.2) and power spectra (Fig. 3.3), it is obvious that any movement directly influences the magnetic field registration. A more quantitative assessment through coherencies is provided in Fig. 3.4, providing a measure of the correlation between these values. The second panel in Fig. 3.4 shows a coherency of almost 100% at all frequencies between one tiltmeter component and one horizontal magnetic field component, implying that in this case, the movement mainly arises from a certain direction. Although the processing described in Section 3.4 can deal with some noise and outliers, such high noise levels as those observed heavily distort the calculation of transfer functions and must therefore be removed.

3.2.1 Attempts to eliminate noise

Different techniques were utilized in an attempt to cancel out the noise of the instrument's shaking. Test measurements in an electromagnetically noise free, remote place of Schleswig Holstein were carried out with a self-constructed non-magnetic shaking-apparatus (for details see appendix 7.7). An MT sensor was fixed to the shaking apparatus while comparing measurements were recorded on a solid level

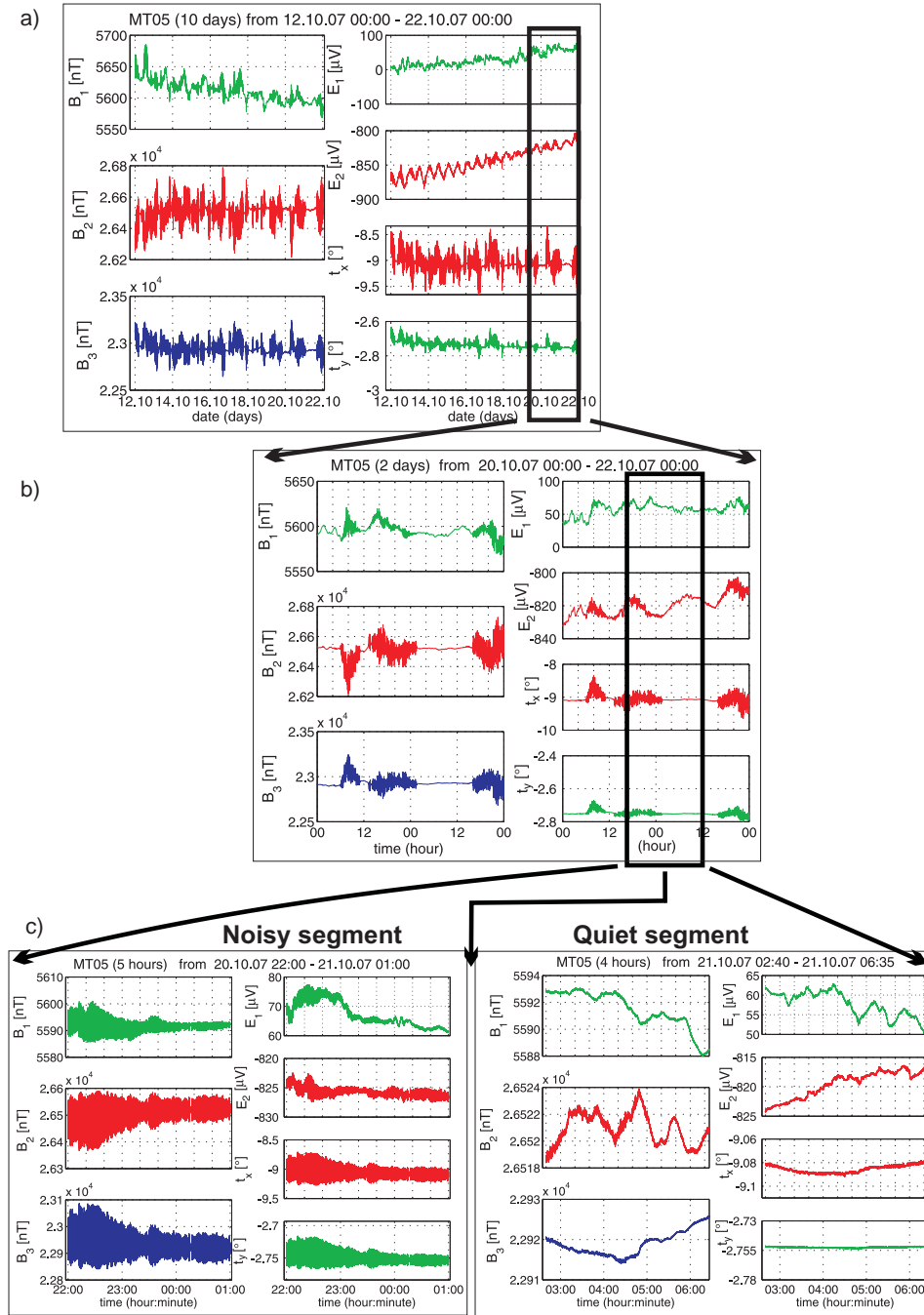


Figure 3.2: Example of noisy time series of station m05 in different time sections: a) 10 days, b) 2 days and c) 9 hours. B_1, B_2, B_3 = magnetic components; E_1, E_2 = electric fields; t_x, t_y = dual axis tiltmeter registration.

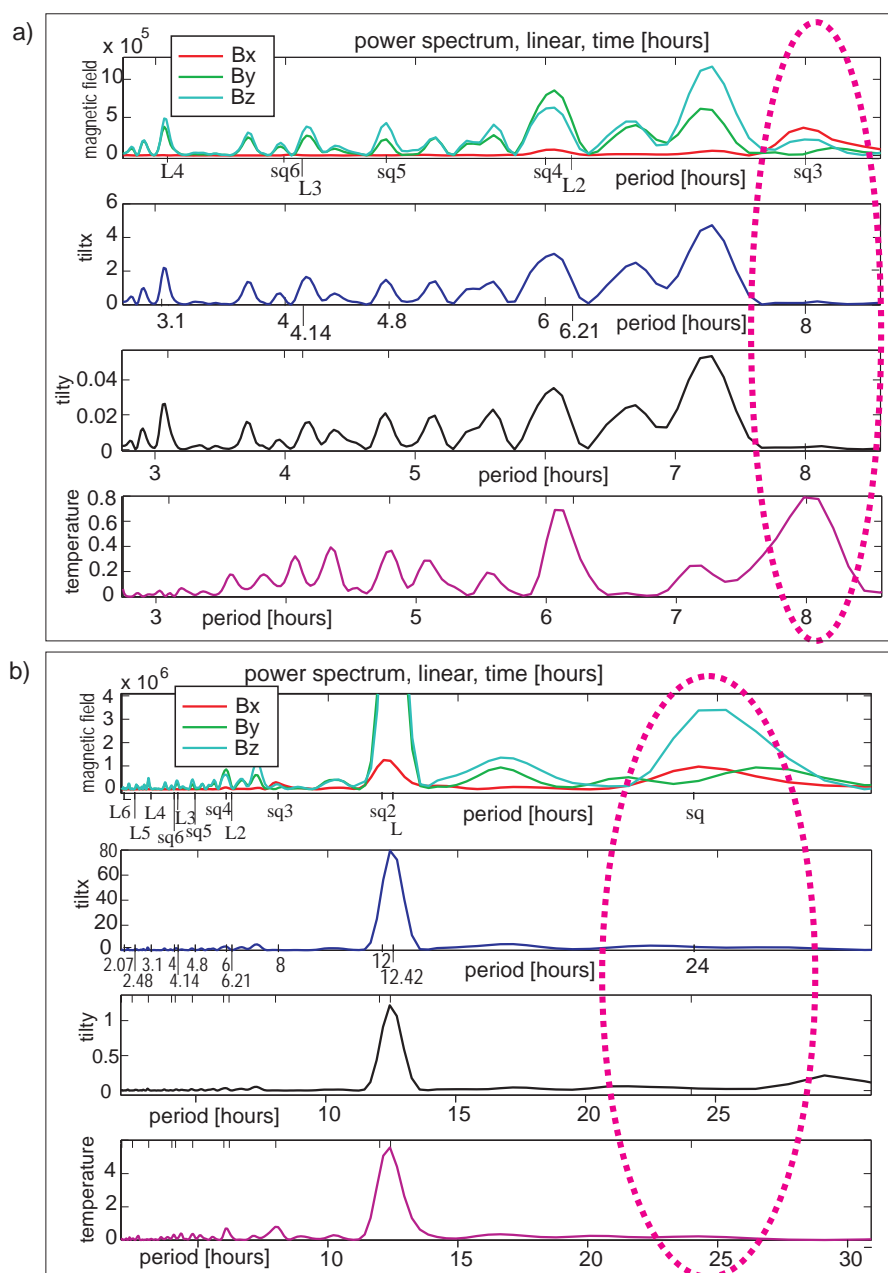


Figure 3.3: Power spectra of recorded time series at station m05 (section as in Fig.3.2). Uppermost panels of a) and b) display magnetic field components; second and third panels show tilt registrations in two components; lowest panels show temperature. Typical natural signals (solar sq and lunar L) are labeled on abscissas of uppermost panels. Noisy sections reveal high correlation between water enforced movement (tilt) and magnetic field, which dominates the whole spectra. Yet, natural signals are also visible (outlined by red dashed circles).

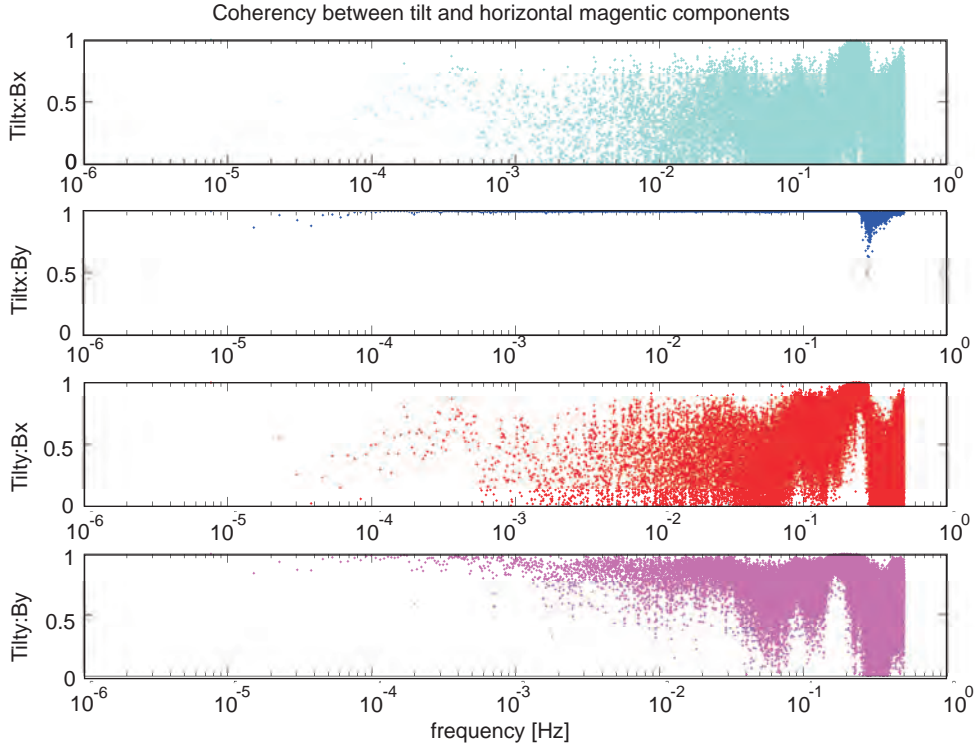


Figure 3.4: Coherency between tilt components and horizontal magnetic components at station m05 for the the 12-days long time section in Fig.3.2.

with a second magnetometer for reference. Controlled shaking and rotation of the apparatus yielded data sets that could be evaluated with respect to quiet reference measurements. Using this controlled experiment and the recorded data of the Costa Rican experiment, three different noise reduction approaches were tested:

- 1.) An attempt was made to rotate back the magnetic field time series at each sample using the displacement angles measured by the tiltmeter. For the transformation to the horizontal plane, rotational matrices were used as described in Fitterman and Yin [2004], using a modification discussed in Section 3.3.
- 2.) Several filter options were tested, including an adaptive filter described by Lezaeta et al. [2005], designed to clean the time series using a variable filter that permanently adapts its entries according to changes in the tiltmeter time series.
- 3.) A frequency dependent transfer function between noise vector (tiltmeter components) and horizontal magnetic field vectors was searched for in order to transform back the time series vector.

All of these attempts failed, especially within sections of high noise level - nei-

ther of the attempts reduced the noise sufficiently to a level lower than the natural electromagnetic signals. The unsuccessful attempts will not be evaluated here, but comments on the assumed reasons for the failures are given.

In some sections the noise generated through tilt variation is much higher than 0.1° , at some stations reaching several degrees. These string movements infer a response in the magnetic field sensor that ranges over tens to hundreds of nT, which is much higher than natural signals measured at the ocean bottom. Here, normal filtering fails, because periodical motions dominate over natural variations at all frequencies, as shown in Section 3.1. As a consequence, the natural signals are also filtered out. Adaptive filtering technique also fail at such high noise levels as has been observed by Lezaeta et al. [2005]. Furthermore, noise that arises from movement is not uncorrelated, thus, the standard processing technique (as will be examined in Section 3.4) cannot provide clean transfer functions.

One reason of the failure could be the inertia of the liquid in the tiltmeter sensor. The tiltmeter accuracy is tied to temperature, total inclination and settling time of the liquid (for manufacturer information see Appendix 7.1 and Section 2.5). The temperature at the ocean bottom varied by only $0.3^\circ C$ during the whole measuring period. This infers maximum changes in the tiltmeter registration of 0.001° , which is beyond the resolution. Therefore a temperature effect can be excluded. The total (static mean value) inclination of all stations, except for m01, were below 10° at each tiltmeter component, which assures an accuracy of at least 0.01° (see Appendix 7.1). But the settling time of the liquid takes around 0.5 s at a temperature of $20^\circ C$, and it becomes longer at lower temperatures as the viscosity increases (pers. communication with manufacturer). Thus, the response to a sudden motion is delayed in the tiltmeter response, whereas a sudden change of the magnetic sensor's position is immediately registered. This causes a delay between the actual motion and the response of the tiltmeter, and therefore a delay between tiltmeter and magnetic field response to the motion. When the sampling rate is comparable to this delay, this should affect any point-by-point transformation, rotation or filtering attempt as no accurate relationship between motion and reaction of the magnetic field recording to that motion exists. An inconclusive relationship between motion and magnetic response to motion can also be observed in the time series.

Another reason for the failure of the point-by-point rotation could be an inaccurate calibration of base values of total field components, since the fluxgate magnetometers are calibrated according to a proton magnetometer but do not explicitly measure the total field.

3.2.2 Strategy: using only quiet sections

After all attempts failed to use the complete information of the full time series for calculating reasonable transfer functions, a more forward strategy is adopted: All noisy sections, as defined by the tiltmeter registration, are discarded, and only “clean” time sections are used for processing. All sections are picked by hand according to two criteria:

- 1.) the tilt variation must be smaller than 0.01 (for extremely noisy stations a higher limit had to be accepted chosen after personal assessment), and
- 2.) the section chosen must be highly coherent to the simultaneously recording land station. The land station was installed manually and the sensor was placed according to the magnetic coordinate system (with B_x pointing to North). In contrast, one cannot control the alignment of the marine station as it is dropped from a ship. Thus, for comparison between marine stations and reference station onshore, the marine data must first be rotated to North in order to be aligned with the reference components on land. The rotation is described in Section 3.3.

An example of a quiet segment of five hours length is shown in Fig. 3.5. Red lines indicate the observed magnetic components of station m05 after it has been rotated to North and to the horizontal plane as described in Section 3.3 in order to be comparable to the magnetic field recorded by the land reference station (black lines). A high correlation of the seafloor fields to the land registration is observed. However, the land station data contains high frequency signals not visible in the recordings at marine station m05. This is explained by the attenuation of electromagnetic signal in the conducting ocean: the equation of the skin depth (Eq. 2.13) predicts, for a 3 km thick ocean of 0.3 Ω m resistivity, that periods smaller than 120 s barely reach the ocean bottom as the electromagnetic energy is dissipated as it travels through the ocean layer. Note that the section between 10,500 s and 11,500 s displays some high frequency content at B_z -component of m05 (lowest panel) attributed to noise. However, such small-scale disturbances hardly affect the derivation of transfer functions as the processing tools can compensate for this (Section 3.4).

Other differences between the registrations of the reference land station and quiet sections of the marine stations are due to expected induction effects and constitute the desired electromagnetic signal.

Stations far offshore display good quality and noisy sections are cut out liberally. However, stations close to the coast line are so disturbed that any section of comparably low noise level has to be picked out to ensure enough data for processing. As an extreme example, at station m03, about 60 single sections of only a few hours length each are cut out, while the rest of the time series (over 90%) had to be discarded. Data at station m01 could not be used at all, because after a few days of

extremely noisy registrations, strong water currents/waves eventually dislodged the station to an imbalanced position outside the tiltmeter range ($> 20^\circ$). Fig. 3.6 a gives an overview of all quiet segments that are eventually used for processing selected for the time series recorded at each station.

The procedure of picking out usable sections of the time series by hand is rather labor-intensive. A more practical and elegant solution to this is in preparation (J. Chen, pers. communication) and consists of a processing scheme in the time domain that automatically allows for the selection of usable time sections under certain criteria.

The long recording time of all stations assure a broad selection of usable time segments and sufficient low noise data could be identified to determine meaningful transfer functions. However, these quiet sections are remarkably void of large geomagnetic activity. This is due to the fact that the magnetic activity was very low during the entire measuring period as illustrated by the ap index in Fig. 3.6 b, lower panel. All values are lower than 40, although the ap index ranges up to 400 during magnetic storms (Section 2.3.2). Nevertheless, the time series do contain signals which are now used for derivation of transfer functions.

3.3 Rotation of time series

When the OBMT instrument is deployed and sinks down, it normally reaches the seafloor with an arbitrary orientation from the North direction and might also be tilted from the horizontal plane, if the seafloor is not even. For further evaluation all stations must be aligned to the same coordinate system, and therefore the time series are rotated accordingly to a right-handed orthogonal system in which B_x points to North, B_y points to East (with B_x, B_y on a horizontal plane) and B_z points to depth. This system will be hereafter referred to as the “inertial frame”, while the system in which the OBMT instrument records on the ocean bottom will be referred to as “observation frame”.

3.3.1 Rotation to the inertial frame

To achieve a transformation from the observation frame to the inertial frame, rotations are performed as described by Fitterman and Yin [2004], except for one modification discussed in the following. By their convention, the rotation from the inertial frame to the observation frame is decomposed into three rotations. The first, called “yaw”, is a rotation ψ_Y around the transverse axis. Following this rotation, the new orientations of the frame axes are labeled as x' and y' , respectively (see

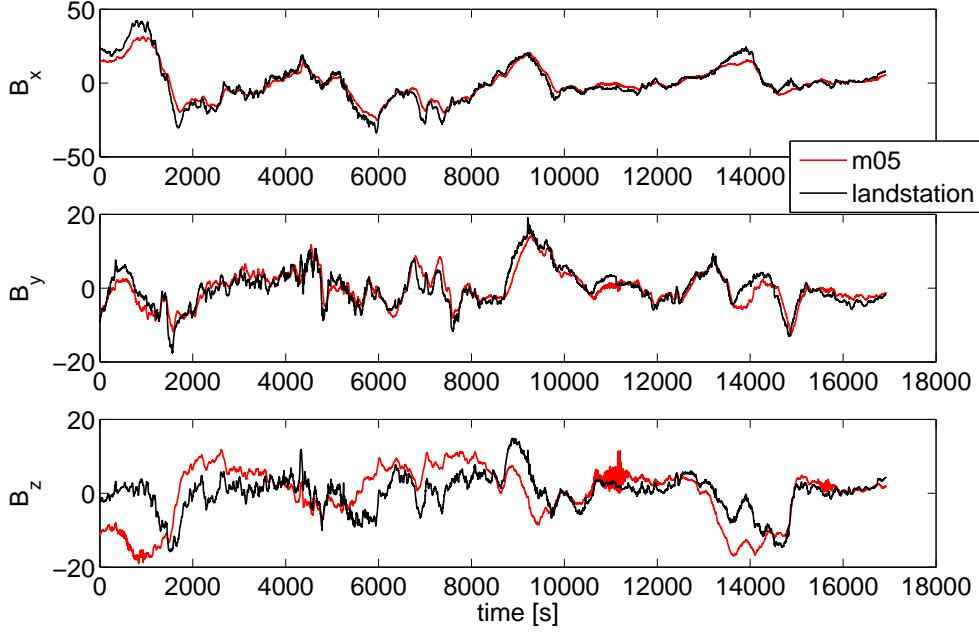


Figure 3.5: Comparison of simultaneous recordings at the reference land station (black line) and a quiet segment of m05 (red line). Note that marine magnetic fields of m05 are rotated to North and to the horizontal plane (as described in Section 3.3), in order to be comparable.

Fig. 3.7). The second rotation, called “pitch”, is a rotation ψ_P around the new axis y' resulting in the new axes x'' and z' . The third rotation, called “roll”, is a rotation ψ_R around the new axis x'' . After operating the yaw, pitch and roll rotations, the (new) observed frame is given by x'' , y'' and z'' .

The magnetic field vector in the inertial coordinate system is expressed as

$$\vec{B}_{inert} = x\hat{\mathbf{i}} + y\hat{\mathbf{j}} + z\hat{\mathbf{k}}. \quad (3.1)$$

Following a sequence of yaw, pitch and roll rotations, the vector will have the components x'' , y'' and z'' :

$$\vec{B}_{obs} = x''\hat{\mathbf{i}} + y''\hat{\mathbf{j}} + z''\hat{\mathbf{k}}. \quad (3.2)$$

Note that this vector is still dependent on the unit vectors in the inertial system, only the length of its components have changed. The relationship between the vectors \vec{B}_{inert} and \vec{B}_{obs} is given by

$$\vec{B}_{obs} = \mathbf{R}_{roll}\mathbf{R}_{pitch}\mathbf{R}_{yaw}\vec{B}_{inert}, \quad (3.3)$$

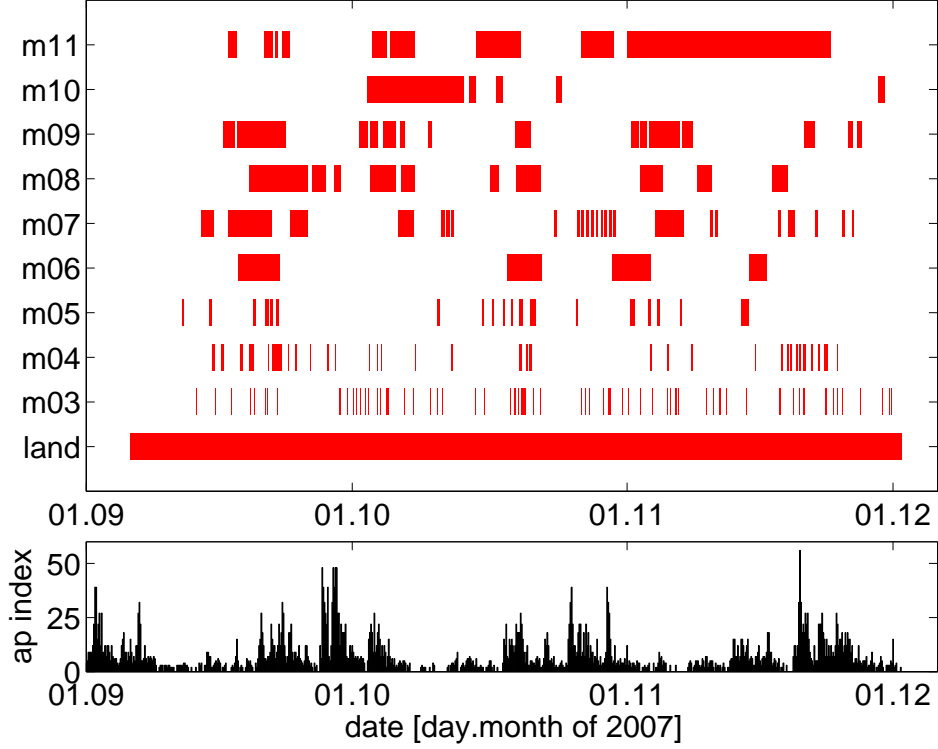


Figure 3.6: a) Overview of all identified quiet time segments which are used for processing. Land station data was recording throughout the entire time yielding good quality. b) Magnetic activity during the same time period (ap values were kindly provided by the Adolf-Schmidt-Observatorium in Niemegk, GFZ Potsdam).

where the matrices for the individual yaw, pitch and roll rotations are given respectively by

$$\mathbf{R}_{\text{yaw}} = \begin{pmatrix} \cos\psi_Y & \sin\psi_Y & 0 \\ -\sin\psi_Y & \cos\psi_Y & 0 \\ 0 & 0 & 1 \end{pmatrix},$$

$$\mathbf{R}_{\text{pitch}} = \begin{pmatrix} \cos\psi_P & 0 & -\sin\psi_P \\ 0 & 1 & 0 \\ \sin\psi_P & 0 & \cos\psi_P \end{pmatrix},$$

$$\mathbf{R}_{\text{roll}} = \begin{pmatrix} 1 & 0 & 0 \\ 0 & \cos\psi_R & \sin\psi_R \\ 0 & -\sin\psi_R & \cos\psi_R \end{pmatrix}.$$

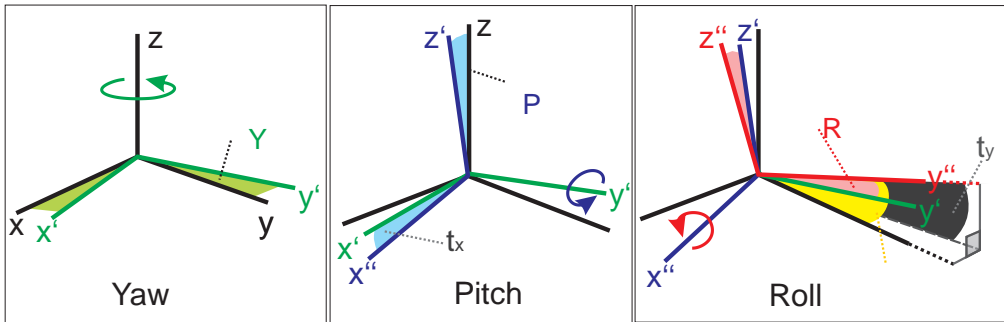


Figure 3.7: Rotation of coordinates from the inertial system to the observed system modified after Fitterman and Yin [2004]. The inertial system axes are given by $x; y; z$, and are depicted in the black frame. The observation system axes are $x''; y''; z''$. ψ_Y , ψ_P , and ψ_R denote the yaw, pitch, and roll angles, and t_x , t_y the displacements from the horizontal (x,y)-plane, as observed from tiltmeter sensors in OBMT instruments.

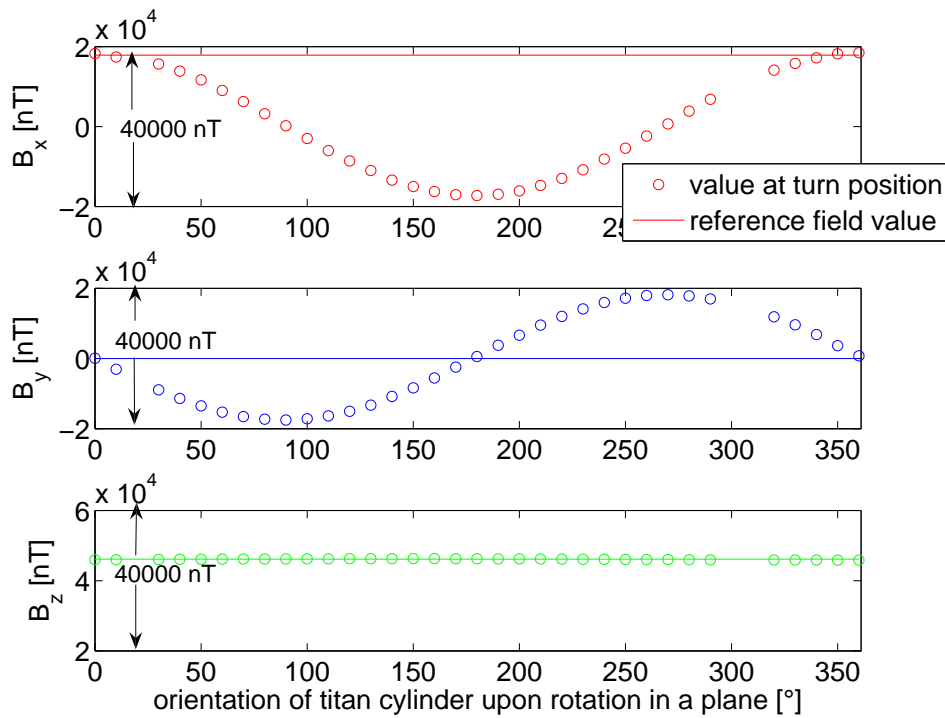


Figure 3.8: Data obtained during test measurements at Viehdamm (see Appendix 7.7). Rotation of fluxgate magnetometer on a horizontal plane in steps of one degree. Circles display recorded values at each rotated position, lines display reference magnetometer components.

Since matrix multiplication is not commutative, the order of multiplication may not be changed. The original vector (of the inertial system) $\begin{pmatrix} B_x \\ B_y \\ B_z \end{pmatrix}$ becomes the

observed vector $\vec{B}_{obs} = \begin{pmatrix} B_{1,obs} \\ B_{2,obs} \\ B_{3,obs} \end{pmatrix}$.

However, the OBMT instrument does not measure the roll angle as described above. After applying the rotations as illustrated in Fig. 3.7, the roll angle ψ_R does not equal the angle measured as displacement from the inertial system (the horizontal (x,y)-plane). But the tiltmeter sensor of the OBMT instrument measures the displacement from the horizontal Earth plane in two components (dual axis). The measured angle t_x corresponds to the pitch angle ψ_P , the horizontal displacement. However, the measured angle t_y does not directly correspond to the roll angle ψ_R (see Fig. 3.7). Instead, the roll rotation must be performed with the angle ϕ which is related to the measured tilt angles t_x and t_y by

$$\phi = 2 \cdot \arcsin \left\{ \frac{\sin(0.5 \cdot t_y)}{\cos(t_x)} \right\}, \quad (3.4)$$

(geometrical derivation by J. Chen, pers. communication).

Hence, the equation used for rotating back the observed magnetic field vector to the inertial frame is given by:

$$\vec{B}_{inert} = \mathbf{R}_{yaw}^{-1}(\alpha) \cdot \mathbf{R}_{pitch}^{-1}(t_x) \cdot \mathbf{R}_{roll}^{-1}(\phi) \cdot \vec{B}_{obs}. \quad (3.5)$$

For $t_y \ll 1$ and $t_x \ll 1$, ϕ becomes identical to t_y ($\phi \approx t_y$). However, this modification only becomes noticeable at angles larger than several degrees.

The procedure to transform the observed magnetic field vector to the inertial frame is divided into two steps. First the measured vector is rotated to the Earth horizontal plane (without yaw-rotation to North): $\vec{B}_{plane} = \mathbf{R}_{pitch}^{-1}(t_x) \cdot \mathbf{R}_{roll}^{-1}(\phi) \cdot \vec{B}_{obs}$. The vertical z-component of \vec{B}_{plane} equals the z-component observed in the inertial frame, but since the horizontal components are not yet aligned to North and East, they are denoted as $B_{1,plane}$ and $B_{2,plane}$. Thus, the vector components of the magnetic field on the horizontal (x,y)-plane, \vec{B}_{plane} , are given by:

$$\begin{aligned} B_{1,plane} &= Bx_{obs} \cdot \cos(t_x) + By_{obs} \cdot \sin(t_x)\sin(\phi) + Bz_{obs} \cdot \sin(t_x)\cos(\phi), \\ B_{2,plane} &= By_{obs} \cdot \cos(\phi) - Bz_{obs} \cdot \sin(\phi), \\ B_z &= -Bx_{obs} \cdot \sin(t_x) + By_{obs} \cdot \cos(t_x)\sin(\phi) + Bz_{obs} \cdot \cos(t_x)\cos(\phi). \end{aligned} \quad (3.6)$$

This yields a vector in the (x,y)-plane, $(B_{1,plane}, B_{2,plane})$, that now must be rotated around the z-axis to North for achieving (B_x, B_y) in the inertial frame. For the rotation to North, the yaw rotation matrix is used as described in the next paragraph.

3.3.2 Rotation to North (finding the “yaw” angle)

The total magnetic field vector is measured as a superposition of the large static primary field, that can be considered constant over the measuring period, and the much smaller fluctuating secondary field which provides the induction signals (see Section 2.3). When the total vector of the static primary field is measured in an orthogonal system with one component pointing to North and another to depth, then the third static component pointing to East is always zero (this certainly does not account for the magnetic fluctuations of the secondary field). Using this fact, a record of the total field vector components can be used as a compass. Hence, there are several ways to find the the North direction from a magnetic measurement that has recorded the total field components:

- One is to rotate the mean vector of $(B_{1,plane}, B_{2,plane})$ in small degree’s steps until $B_{2,plane}$ becomes minimal.
- Another is to use a land reference station that is consciously aligned to North. The time series of $(B_{1,plane}, B_{2,plane})$ is rotated in small degree’s steps until the highest coherency is reached between the rotated station and the reference station.
- Another is to find the functional minimum. Since $B_{2,plane}$ must be minimized, the angle α sought after must fulfill the condition:

$$\frac{\partial B_2(\alpha)}{\partial \alpha} = -B_1 \cdot \sin(\alpha) + B_2 \cdot \cos(\alpha) = 0$$

$$\Rightarrow \alpha = \arctan\left(\frac{B_2}{B_1}\right).$$

Fig. 3.8 shows how the three orthogonal components of the static total magnetic field change as the sensor is rotated in one degree steps from zero to 360° (circles display observed registration at each rotation angle, continuous line is the reference value to sensor aligned to North and East). There are two positions at which $B_{2,plane}$ ($= B_y$) minimizes (second panel): one at which $B_{1,plane}$ ($= B_x$) points to North and one as it points to South (B_x in first panel). This is a 180-ambiguity that can easily be solved by establishing a query in the rotation code for finding the angle α at which $B_{2,plane}$ minimizes and $B_{1,plane}$ is positive. This constraint assures a right handed coordinate system with B_x positively pointing to North and B_y positively to East.

Once that quiet segments as presented in Fig. 3.6 are selected from the time series, following steps are performed:

1. Mean values of the tilt registrations in each selected segment are calculated and then used to separately rotate segments to plane using the three equations 3.6. This yields timeseries rotated to the horizontal plane.
2. From the horizontal plane rotated time series, the mean values of the magnetic field components within each of the plane rotated segments is calculated (for seeking the North (yaw) angle).
3. Using the mean values of the magnetic timeseries in the plane, the yaw angle is determined after the three methods described above in the enumeration and the result from the methods are compared, approving that each of the method yields the same result.
4. The calculated (and approved) yaw angle is used to rotate every single of the plane-rotated segments to North.
5. Each fully rotated section is compared to the simultaneous recording of the reference station on land by visual inspection - an example is given in Fig. 3.5.

After performing these steps, the achieved quiet time series segments, which are rotated to the inertial coordinate system, are processed together with the reference land station as discussed in the next Section.

3.4 Processing of time series \Rightarrow transfer functions

All recorded time series inhibit biasing effects arising from remaining noise which ought to be removed within the processing (also the quiet time series segments still contain noise). In the following, a general approach of a simple and basic processing scheme is described. As evaluated in Buttkus [1991] and Simpson and Bahr [2005], the basic procedure is outlined in several steps:

1. The time series segments are windowed and Fourier transformed in these windows to the frequency domain (FFT), power and cross spectra for all electromagnetic components are calculated (the specific spectra are evaluated in Paragraph 3.4.1).
2. The achieved spectra are smoothed in order to assure an equidistant spectral arrangement in the logarithmic presentation. The smoothing of neighboring frequencies can be operated through different spectral windows, a popular one would be the "Parzen-typ". The spectra prewhitened to avoid Leakage effects and systematic errors.

3. The evaluation frequencies are chosen according to two conditions: One is that the evaluation frequencies are equally spaced on a logarithmic scale, and second is that ideally there should be only 6-10 evaluation frequencies per decade. More frequencies are unnecessary (Simpson and Bahr [2005]), because the dispersion relation (Kramer-Kronig relation) as defined by Weidelt [1972] predicts similar results for neighboring frequencies, but fewer result in an aliasing in the frequency domain. However, frequency bands are chosen, and within these bands the frequencies are averaged.
4. Noise reduction in the transfer function estimates are achieved through coherence sorting or “remote reference” technique described in Paragraph 3.4.2.
5. “Clean” spectra of all segments are averaged.
6. Impedance tensor and Tipper elements are calculated as explained in further detail in Paragraph 3.4.1.
7. From impedance tensor elements, apparent resistivities and phases are calculated as defined in Section 2.3.

Different popular processing codes are available, which have refined some of the points applying mathematically more sophisticated techniques, e.g. Egbert [1997] and Egbert [2002], Chave and Thomson [2004] and Chave and Thomson [1989], Ritter et al. [1998], Jones et al. [1989]. In this work, the BIRRP code developed by Chave and Thomson [2004] has been used.

The following paragraphs describe the basic calculation of impedance tensor elements and the remote reference technique.

3.4.1 Calculating impedance tensor and Tipper elements from spectra

As introduced in Section 2.3, the spectra of the electric and magnetic spectra are related through the complex valued impedance tensor $\underline{\underline{Z}}$ (Eq. 2.4). In expanded form it may be rewritten as:

$$E_x(\omega) = Z_{xx}(\omega)H_x(\omega) + Z_{xy}(\omega)H_y(\omega), \quad (3.7)$$

$$E_y(\omega) = Z_{yx}(\omega)H_x(\omega) + Z_{yy}(\omega)H_y(\omega). \quad (3.8)$$

The electric (E_i) and the magnetic (H_i) field components are observed values (with $i, j \in x, y$), from which the impedance tensor elements Z_{ij} will be determined. The following summarizes the most important steps for derivation of the impedance tensor elements from the measured components (after Buttkus [1991]).

Eq. 3.7 and 3.8 become inexact through noise. Therefore, the impedance tensor $\underline{\mathbf{Z}}$ requires a statistical solution that minimizes for the uncorrelated noise. The uncorrelated noise is assumed to have normal (Gaussian) distribution. The uncorrelated noise arising from the electric field may be accounted for by the remainder function $\delta\mathbf{Z}(\omega)$ added to Eq. 3.7 and to Eq. 3.8:

$$E_x(\omega) = Z_{xx}(\omega)H_x(\omega) + Z_{xy}(\omega)H_y(\omega) + \delta\mathbf{Z}_x(\omega) \quad (3.9)$$

$$E_y(\omega) = Z_{yx}(\omega)H_x(\omega) + Z_{yy}(\omega)H_y(\omega) + \delta\mathbf{Z}_y(\omega). \quad (3.10)$$

Statistical processing methods like least-square and robust processing techniques are commonly used to solve the functions inferred from Eq 3.9 and 3.10 in terms of minimizing $\delta\mathbf{Z}(\omega)$. Since the components of the impedance tensor are determined through several independent calculations expressed by $E_x^j(\omega)$, $E_y^j(\omega)$, $B_x^j(\omega)$, $B_y^j(\omega)$, $j = 1, 2, \dots, N$, the aim is to minimize the sum of least square mean errors of Eq 3.9 and 3.10:

$$\sum_{j=1}^N \delta\mathbf{Z}_x \delta\mathbf{Z}_x^* = \sum_{j=1}^N (E_x^j - Z_{xx}H_x^j - Z_{xy}H_y^j)(E_x^{*j} - Z_{xx}^*H_x^{*j} - Z_{xy}^*H_y^{*j}), \quad (3.11)$$

$$\sum_{j=1}^N \delta\mathbf{Z}_y \delta\mathbf{Z}_y^* = \sum_{j=1}^N (E_y^j - Z_{yx}H_x^j - Z_{yy}H_y^j)(E_y^{*j} - Z_{yx}^*H_x^{*j} - Z_{yy}^*H_y^{*j}), \quad (3.12)$$

where suffix (*) denotes the complex conjugate.

The minimum may be found by setting the derivative of Eq. 3.11 with respect to Z_{xx}, Z_{xy} , to zero which yields

$$\begin{aligned} \sum_{j=1}^N E_x^j H_x^{*j} &= Z_{xx} \sum_{j=1}^N H_x^j H_x^{*j} + Z_{xy} \sum_{j=1}^N H_y^j H_x^{*j} \\ \sum_{j=1}^N E_x^j H_y^{*j} &= Z_{xx} \sum_{j=1}^N H_x^j H_y^{*j} + Z_{xy} \sum_{j=1}^N H_y^j H_y^{*j}. \end{aligned} \quad (3.13)$$

In an analogue fashion,

$$\begin{aligned} \sum_{j=1}^N E_y^j H_x^{*j} &= Z_{yx} \sum_{j=1}^N H_x^j H_x^{*j} + Z_{yy} \sum_{j=1}^N H_y^j H_x^{*j} \\ \sum_{j=1}^N E_y^j H_y^{*j} &= Z_{yx} \sum_{j=1}^N H_x^j H_y^{*j} + Z_{yy} \sum_{j=1}^N H_y^j H_y^{*j}, \end{aligned} \quad (3.14)$$

may be derived for Eq. 3.12.

For abbreviation, the following notation is introduced:

$$\langle XY^* \rangle = \frac{1}{N} \sum_{j=1}^N X_j Y_j^*, \quad (3.15)$$

such that Eq. 3.13 and Eq. 3.14 now become:

$$\begin{aligned}\langle E_x H_x^* \rangle &= Z_{xx} \langle H_x H_x^* \rangle + Z_{xy} \langle H_y H_x^* \rangle, \\ \langle E_x H_y^* \rangle &= Z_{xx} \langle H_x H_y^* \rangle + Z_{xy} \langle H_y H_y^* \rangle,\end{aligned}\quad (3.16)$$

$$\begin{aligned}\langle E_y H_x^* \rangle &= Z_{yx} \langle H_x H_x^* \rangle + Z_{yy} \langle H_y H_x^* \rangle, \\ \langle E_y H_y^* \rangle &= Z_{yx} \langle H_x H_y^* \rangle + Z_{yy} \langle H_y H_y^* \rangle.\end{aligned}\quad (3.17)$$

From Eq. 3.16 and Eq. 3.17 the impedance tensor components may be derived, i.e.:

$$\begin{aligned}Z_{xx} &= \frac{\langle E_x H_x^* \rangle \langle H_y H_y^* \rangle - \langle H_y H_x^* \rangle \langle E_x H_y^* \rangle}{\det}, \\ Z_{xy} &= \frac{\langle H_x H_x^* \rangle \langle E_x H_y^* \rangle - \langle H_x H_y^* \rangle \langle E_x H_x^* \rangle}{\det}, \\ Z_{yx} &= \frac{\langle E_y H_x^* \rangle \langle H_y H_y^* \rangle - \langle H_y H_x^* \rangle \langle E_y H_y^* \rangle}{\det}, \\ Z_{yy} &= \frac{\langle H_x H_x^* \rangle \langle E_y H_y^* \rangle - \langle H_x H_y^* \rangle \langle E_y H_x^* \rangle}{\det},\end{aligned}\quad (3.18)$$

where

$$\det = \langle B_x B_x^* \rangle \langle B_y B_y^* \rangle - \langle B_x B_y^* \rangle \langle B_y B_x^* \rangle.$$

The solutions of Eq. 3.18 provide estimates of impedance tensor elements with minimal error on E_x and E_y , respectively. If the error is assumed to be rather in the magnetic components, analogous evaluation can be performed for minimizing the error in H_x and H_y .

The elements of the Tipper, $T_x(\omega)$ and $T_y(\omega)$ (Eq. 2.12) are estimated similarly to $Z_{ij}(\omega)$, with the notation defined in Eq. 3.15 the formulation is

$$\begin{aligned}T_x &= \frac{\langle H_z H_x^* \rangle \langle H_y H_y^* \rangle - \langle H_z H_y^* \rangle \langle H_y H_x^* \rangle}{\det} \\ T_y &= \frac{\langle H_z H_y^* \rangle \langle H_x H_x^* \rangle - \langle H_z H_x^* \rangle \langle H_x H_y^* \rangle}{\det}.\end{aligned}\quad (3.19)$$

3.4.2 Remote Reference

The remote reference method was introduced by Gamble et al. [1979a], Gamble et al. [1979b], and Gamble et al. [1982] in order to remove systematic biasing effects from

unaccounted noise in the data. Correlated noise in the magnetic field for an example would downward bias the impedance estimated (see Eq. 3.18). The idea is to deploy an additional station at a remote site in some distance from other stations. The naturally induced signal is expected to be coherent over spatial scales over many kilometers, but noise is normally random and incoherent. Therefore, the magnetic (or electric) recording of a high quality reference station can be used to remove noise on another station, if the noise is uncorrelated to the reference station (the remote reference technique cannot remove noise that is correlated between the stations). Using the notation from Eq. 3.15, and adopting subscripts r to the electromagnetic components of the remote reference station (i.e. $H_{x,r}$, $H_{y,r}$), the equations in 3.18 become:

$$\begin{aligned}
Z_{xx} &= \frac{\langle E_x H_{x,r}^* \rangle \langle H_y H_{y,r}^* \rangle - \langle H_y H_{x,r}^* \rangle \langle E_x H_{y,r}^* \rangle}{det^*}, \\
Z_{xy} &= \frac{\langle H_x H_{x,r}^* \rangle \langle E_x H_{y,r}^* \rangle - \langle H_x H_{y,r}^* \rangle \langle E_x H_{x,r}^* \rangle}{det^*}, \\
Z_{yx} &= \frac{\langle E_y H_{x,r}^* \rangle \langle H_y H_{y,r}^* \rangle - \langle H_y H_{x,r}^* \rangle \langle E_y H_{y,r}^* \rangle}{det^*}, \\
Z_{yy} &= \frac{\langle H_x H_{x,r}^* \rangle \langle E_y H_{y,r}^* \rangle - \langle H_x H_{y,r}^* \rangle \langle E_y H_{x,r}^* \rangle}{det^*}, \tag{3.20}
\end{aligned}$$

where $det^* = \langle B_x B_{x,r}^* \rangle \langle B_y B_{y,r}^* \rangle - \langle B_x B_{y,r}^* \rangle \langle B_y B_{x,r}^* \rangle$.

As stations can be precisely synchronized via GPS, simultaneous data of different sites can be easily processed together. However, a high degree of correlation between the naturally induced electromagnetic fields is required.

3.4.3 The marine transfer functions

The selected quiet data segments, which are rotated to the horizontal plane and to North, are processed using the processing code BIRRP¹, which allows a robust estimation of transfer functions. BIRRP is a standard processing tool in the MT community and has been described in detail by Chave and Thomson [2004] and Chave and Thomson [1989]². For remote referencing, the low noise recordings of the magnetic field variations at the land station are used.

¹BIRRP:= Bounded Influence Remote Reference Processing

²The manual of BIRRP can be downloaded at
http://www.whoi.edu/science/AOPE/people/achave/Site/Next1_files/birrp.5.pdf

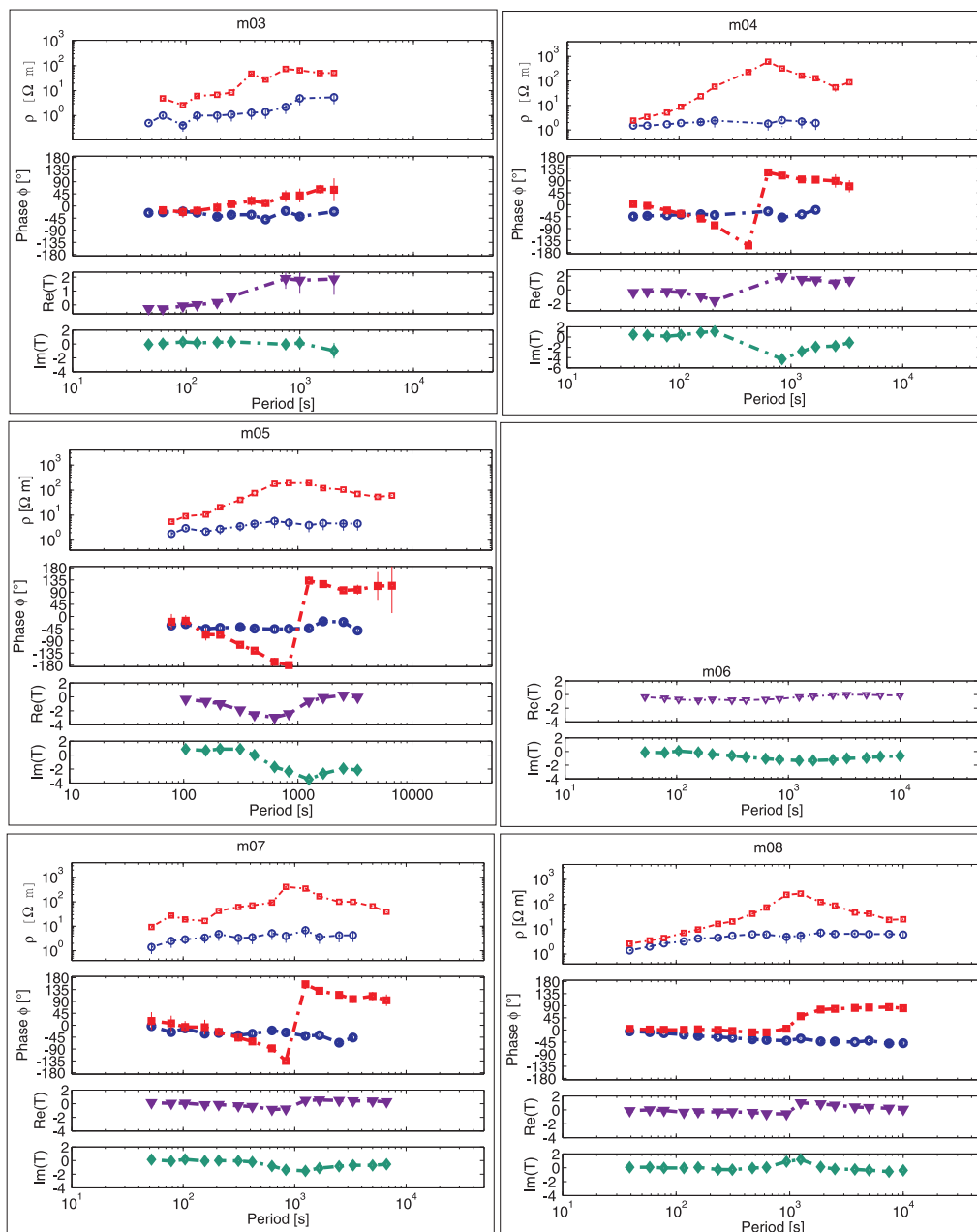


Figure 3.9: Marine strike-rotated transfer functions of stations m03 to m08. Uppermost panels at each station display apparent resistivity (red for TE mode, blue for TM mode), second panels display phase, third and bottom panels display real and imaginary Tipper components. Stations m09 to m11 are displayed in Fig. 3.10.

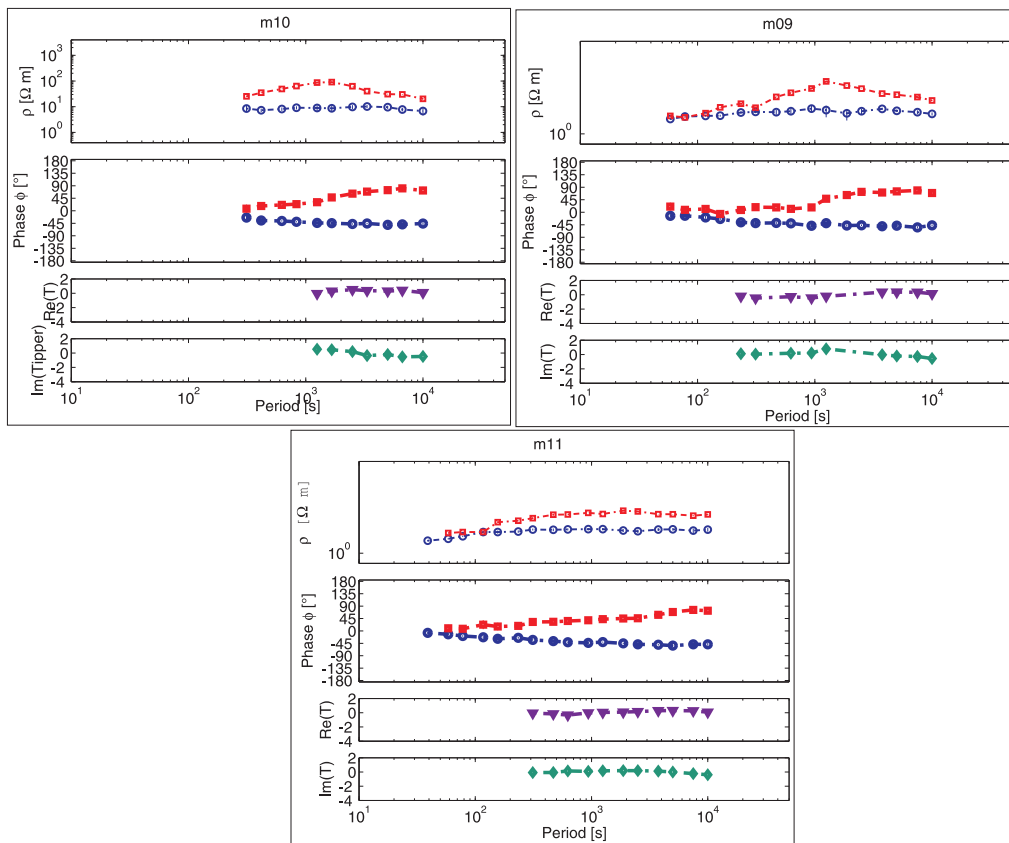


Figure 3.10: Continuation of Fig. 3.9: marine strike rotated transfer functions of stations m09, m10 and m10.

Several constraints are set to guarantee a maximum coherency between the electric and magnetic field data of one marine station and also between the magnetic fields of a marine and a land station. Only quiet time segments as defined in Section 3.2.2 are used. Attempts to derive transfer functions using the tilt disturbed sections failed.

Finally, the obtained transfer functions are to the 2D geologic strike direction, as shown in Fig. 2.8, such that TE mode and TM mode apparent resistivities and phases may be determined. Brasse et al. [2009b] proved the validity of a 2D assumption on the the land data determining a strike angle of 55° (further dimensionality analysis is discussed in the Appendix 7.6). The marine impedance tensors of all stations are rotated to minimize their diagonal elements according to Eq. 2.9 affirming the strike angle found by Brasse et al. [2009b]. The strike rotated transfer functions are displayed in Figs. 3.9 and 3.10. Data of stations close to the coast (m03 and m04) do not provide long periods since the time segments as displayed in Fig. 3.6 are short, because high noise level prevented to choose longer segments. On the other hand, data of stations far away from the coast, and at greater ocean depth, such as m11 and m10, lack smaller periods because of the dissipating effect of the conducting ocean as described in Eq. 2.13 and Eq. 2.14. Station m06 only contains the Tipper data because of an electrode failure.

While TM mode resistivity and phases display rather normal curve types for land or marine data, the observed transfer functions of TE mode and Tipper exhibit extraordinary shapes. The TE mode exhibits a coherent peak in the apparent resistivity at different stations with phases in all four quadrants. The Tipper data grows to unusual high values at different stations. A more detailed investigation of the extraordinary shapes will be presented in the next chapter.

3.5 Summary of Chapter 3

- An amphibious experiment is conducted in the Costa Rican subduction zone yielding electromagnetic time series.
- Examination of marine recordings reveals that data of stations far offshore are of high quality, whereas data of marine stations close to the shoreline on the continental shelf are highly affected by water current and wave enforced motion.
- Any movement expressed by an inclination greater than a few hundreds of a degree causes highly correlated noise and thus an artificial signal on the magnetic field that in fact exceeds the natural signals at the sea floor. This noise is present at all frequencies and prevents the calculation of reasonable transfer functions.
- The noise problem is (only) solved by simply discarding all noisy sections in the timeseries and restricting the evaluation on only to quiet segments.
- The quiet time segments are all rotated to the horizontal plane and to the North direction in order to be evaluated with a remote reference station on-shore that has been recording simultaneously.
- All recovered marine stations in Costa Rica are processed using a code by Chave and Thomson [2004], called BIRRP, yielding transfer functions for MT and GDS.
- Finally, the transfer functions are rotated to the 2D-strike direction and examined. In the correct coordinate system (aligned to geologic strike), the transfer functions display very odd shapes, which will be analyzed in the next chapter.

Chapter 4

The coast effect on marine transfer functions

This chapter contains the publication:

Approximations for the 2D-Coast Effect on Marine Magnetotelluric Data

in review at Geophysical Journal International, 2010.

Authors: T. Worzewski and M. Jegen

The original form has been slightly modified in order to prevent repetition concerning information on the experiment and data analysis, which have been discussed in the previous chapters. The main structure remains, however.

4.1 Abstract

We observe seemingly anomalous transfer functions in a marine magnetotelluric dataset acquired offshore the Costa Rican subduction zone. At specific periods in specific distances to the coast, apexes in apparent resistivity curves appear in the TE mode, which are accompanied by phases that wander through all quadrants. At the same distances and frequencies, the Tipper also exceeds normal values. These observations have been reported and partly explained before as the marine coast effect. In this contribution, these effects will be discussed and defined in more detail, based on numerical modeling of several ocean-coast scenarios. The study reveals that this effect depends on several physical parameters, such as distance from the coast, period, ocean depth and bulk resistivity. We derive approximations that define a characteristic period and characteristic distance from the coast at which the effects in TE mode and Tipper are to be expected to be the most pronounced for simple ocean-coast settings.

4.2 Introduction

The coast effect could be regarded as an extreme bathymetric feature distorting the data. Distortion of marine MT data due to bathymetric and/or coastal effects has been long recognised and dealt with in various contexts. Several authors have attempted to remove the distortion of the marine response. One approach is to incorporate the topography directly in the inversion process; another is to estimate the bathymetric effects for correction of the data prior to inversion. Nolasco et al. [1998] apply a hybrid approach to distortion removal, and model the bathymetric influence as precisely as possible in order to remove it from the data using a thin-sheet approximation. Baba and Seama [2002] present a technique to incorporate seafloor topography into forward modelling by transforming variations in oceanic thickness into variations in electrical properties. Baba and Chave [2005] derive an analysis method for seafloor MT data which combines the removal of three-dimensional topographic effects with inversion of the data for two-dimensional structure. Schwalenberg and Edwards [2004] find an analytical formulation to calculate magnetotelluric effects in the presence of a sinusoidal interface and report distortions in apparent resistivities and phases.

These studies cover several aspects of bathymetric effects on marine MT data. Normally, the distortion is considered unwelcome, and attempts are made to remove it from the measured data. However, in contrast to bathymetric variations, corrections on the data for the coast effect cannot be made. Hence, we aim to characterize the coastal effect in detail by describing a significant effect on TE mode and Tipper responses and by providing a quantitative analysis of the effects. In marine magnetotelluric (MT) data offshore continental margins, notable effects can be observed, which would be considered unusual for land MT responses: Peaks occur in TE mode apparent resistivity curves, which are accompanied by phases that wander through all quadrants. At the same time, the Tipper increases to extremely high values. TM mode apparent resistivities are less affected and show a slight decrease.

Such data have been recorded and also modelled before. In the framework of the Tasman Project, Ferguson [1988], Ferguson et al. [1990], Kellet et al. [1991] and Heinson and Lilley [1993] evaluate marine MT recordings between the Australian and the New Zealand shores. Ferguson (1988) records anomalously high Tipper values expressed by induction arrows and observes a frequency-dependence of the maximum coast effect when displaying the Tipper magnitudes of all sites over the distances from coast. Furthermore, observed TE mode phases of some stations in the Tasman Sea wander through all four quadrants and TE mode apparent resistivities show extreme values at specific periods. Although the investigation of Ferguson et al. [1990] indicates that the geomagnetic induction is influenced by the large-scale

3-D conductivity structure of the region, Ferguson [1988] already recognized that the most pronounced features may be attributed simply to a 2D coastal effect, which is also confirmed by modeling studies by Kellet et al. [1991].

“Negative Phases” and peaks in TE mode apparent resistivities are also reported offshore California by Constable et al. [2009], who could also reproduce these special features with a 2D bathymetric model.

We also recorded such eccentric data offshore the Costa Rican subduction zone (for map see Fig. 3.1) and will investigate the special signature of responses in TE mode and Tipper by a comprehensive modelling study. The aim is to evaluate the parameters that control the coast effect and to investigate whether useful geological information may be derived from them. This study will show that the coast effect can help with data interpretation as it inherits information regarding the average bulk resistivity and increases the sensitivity to conductivity anomalies.

4.3 Description of the effect: The specific distortion signature in the responses

The offshore measurements in Costa Rica are depicted in Figs. 3.9 and 3.10. Station m05 was recording on the continental slope 50 km offshore. Station m07 and m08 were further offshore (80 and 95 km from the coast); and station m11 is farthestmost from the coast (190 km offshore). Some stations, including m07 and m08, have pronounced peaks in TE mode apparent resistivities at around 1000 s. TE mode phases of m07, m05 and m04 wander through all quadrants. Tipper values of stations m04 to m08 exceed typical values (>1) and taper at around 1000 s. Additionally, the peak in the imaginary part of Tipper flips polarity between m08 and m07.

For our comprehensive modeling study we use the finite element code “FEMMT” developed by Franke et al. [2007], which models plane-wave diffusive time-harmonic electromagnetic fields. FEMMT uses an adaptive unstructured triangular grid, which proved to be very suitable for simulating electromagnetic fields on the ocean bottom as it can closely conform to any seafloor bathymetry. MT responses are calculated in a simple coastal setting with a continental slope (approximated by a triangle) for stations on the ocean bottom as shown in Fig.4.1 a. Initially, the bulk resistivity is set to $50 \Omega m$ and ocean depth to 4 km, which is comparable to the geological setting in Costa Rica. The full model in this case extends from -800 km to +800 km horizontally and down to 600 km depth. The coast in this model is placed at position zero. An appropriate mesh adapted to station position, conductivity contrast and model geometry, is generated automatically within the FEMMT code by (Franke et al, 2007). The TE mode and Tipper responses for several sea floor

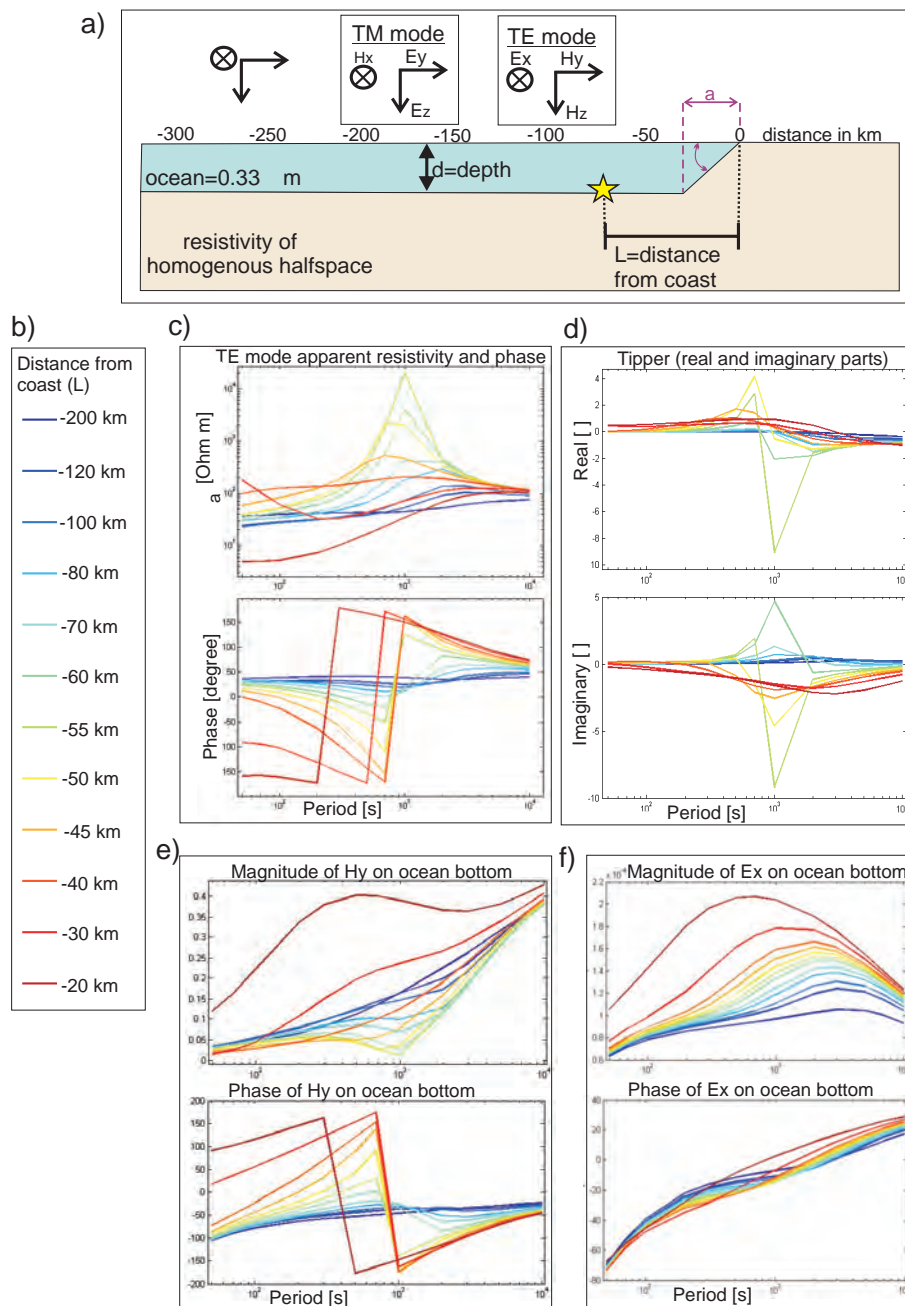


Figure 4.1: Modeled transfer functions and electromagnetic field components of selected stations on ocean bottom for a fixed ocean depth (4 km) and a fixed background resistivity ($50 \Omega m$). Subfigures (c) to (f) display responses of TE mode, Tipper, magnetic and electric fields at the ocean bottom. Abscissas are periods scaled between 40s and 10,000 s. Each colored curve is the response of a station at a certain distance to the coast (legend in (b)).

stations are displayed in different colours in Figures 4.1 c-f. Stations far away from the coast (blue curves) show normal responses for periods up to a few thousand seconds. Only at higher periods, where the induction volume becomes very large, is the presence of the coast sensed by increasing TE mode resistivities. Close to the coast, stations experience this elevation in apparent resistivity in the form of peaks at progressively smaller periods. In this particular setting, the most pronounced peak (i.e. smallest half-width plus greatest magnitude) is observed at the station at around 55 km distance from the coast (green curve) at a period of around 1000 s (Fig.4.1 b). At coincident periods and distances from the coast, phases leave the quadrant and Tipper responses increase dramatically (Fig. 4.1 c). Similar distortion has been modelled previously by Alekseev et al. [2009].

To facilitate further discussion, this signature at which the effect is most pronounced will be referred to as “**maximum effect**”; T_{me} shall denote the characteristic period, and L the characteristic distance to the coast at which the maximum effect occurs.

As can be seen in In Fig. 4.1 e, the maximum effect is related to a minimum in the horizontal magnetic field component perpendicular to the coast H_y . The complex value of H_y is expressed as its magnitude and phase. A global minimum in field strength occurs exactly at the station of maximum effect (green curve). In contrast, the horizontal electric field (Fig. 4.1 e) does not display any anomalous behaviour at the maximum effect. In both calculations of Impedance and Tipper, this implies a minimized denominator giving rise to a maximized response.

4.4 Why is there a minimum in the horizontal magnetic field?

Constable et al. [2009] explain the TE mode distortion by an “inductive effect associated with currents flowing along the edge of the deep ocean basins, steepening the magnetic field and even causing a phase reversal in the horizontal field used for MT impedance calculations (and thus generating negative phases)”.

We demonstrate this by calculating the electromagnetic field components in the entire model with respect to the maximum effect. Fig. 4.2 displays the components at 1000 s (in accordance with the maximum effect observation in Fig. 4.1) that are accountable for the described distortion signature: I.e. the current density j_x (parallel to coast line, pointing into paper plane) and horizontal magnetic field H_y (perpendicular to the coast line). Both values are displayed by the two possible ways of expressing a complex number: on the one hand by their real and imaginary components and on the other by magnitude and phase. In Fig. 4.2, the pink star

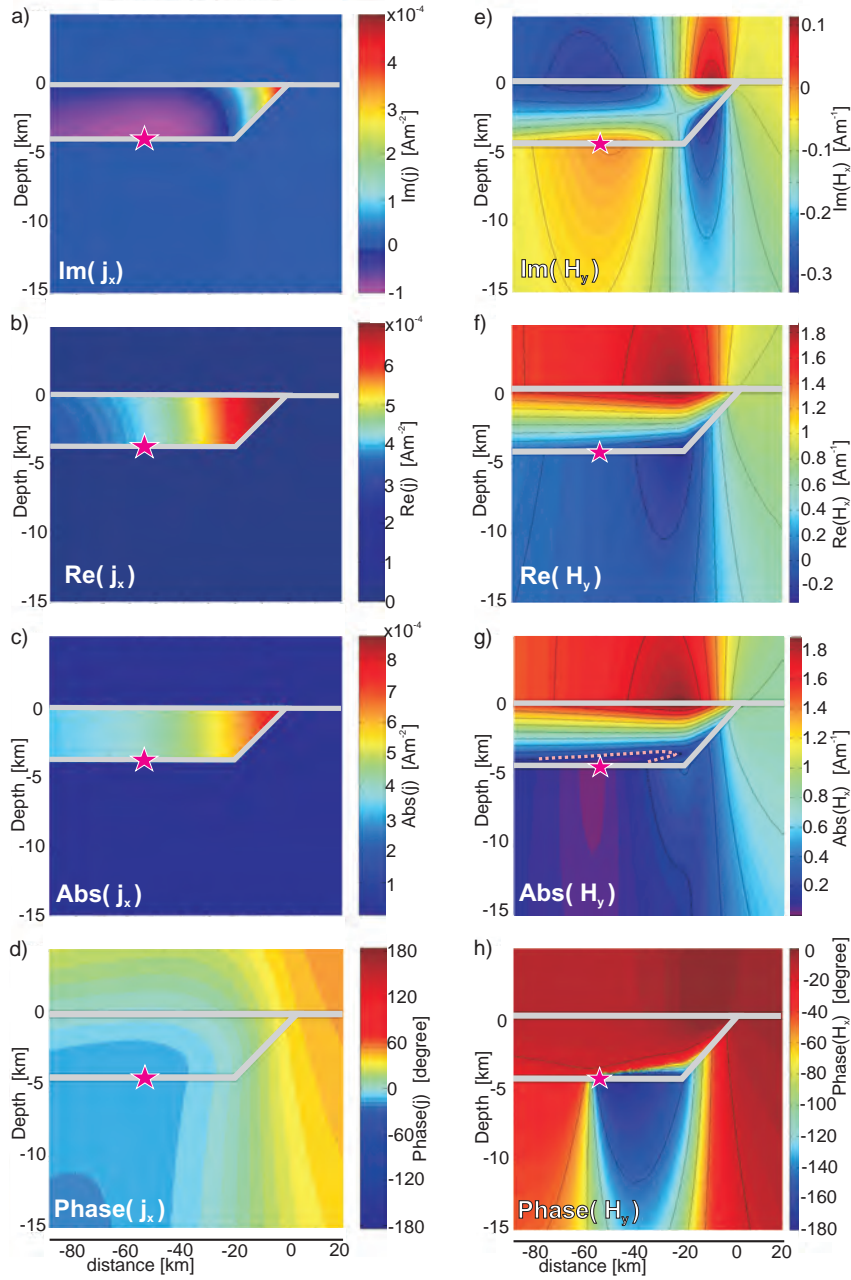


Figure 4.2: Field components throughout the entire model of complex current density j_y in TE mode (pointing into paper plane, left column) and complex valued horizontal magnetic field H_y (pointing towards the coast, right column) at 1000 s (period of maximum effect in this model). Complex values are on the one hand expressed through real (Re) and imaginary (Im) modulus and on the other hand by magnitude (Abs) and phase. The star denotes the position at which the maximum effect is observed.

denotes the position on the ocean bottom at which the maximum effect is observed.

Fig. 4.2 g shows the magnitude of the magnetic field $|H_y|$, which is smallest at the maximum effect position (note the marked isoline that “flips”: from the star position, values of $|H_y|$ are greater for stations further offshore but also closer to the coast). This is accompanied by a rapid phase change (Fig. 4.2 h), which expresses a change in orientation and thus implies an anomalous current. Stations between the star and the coast experience the phase change of magnetic field by displaying TE mode phases that wander through all quadrants.

Current density is strongest at the edge of the coast (magnitude $|j_x|$ in Fig. 4.2 c). However, the phase of the complex valued current density changes within the water column above the star in Fig. 4.2 d, and again implies an abnormal current flowing above the position of the maximum effect. The abnormal current is indirectly visible through the imaginary components of the magnetic field ($\text{Im}(H_y)$ in Fig. 4.2 e) and the current density ($\text{Im}(j_x)$ in Fig. 4.2 a). The current density is highest at the edge for real and imaginary parts, but the imaginary parts become negative in the vicinity of the star. This implies a pronounced change in the induced current pattern.

We infer from the directional change of current density and magnetic field, that an anomalous current is flowing above the star, which is small in comparison to the other currents at the edge, but has a large impact on the response due to its proximity to the station.

Fisher and Schnegg [1978] analytically calculate the responses of an ocean-coast model which consists of a uniformly conducting half-space with an ocean expressed as a perfectly conducting thin-sheet. They note that the idealization and extreme features of their ocean model lead to pathological variations, which may not be observed in practice. And indeed, the responses on the marine side calculated under and above the thin-sheet do not display any features comparable to our observations in this study. Therefore we assume that the maximum effect may not be explained using an analytical solution with a thin-sheet approximation, as a thin sheet has no thickness to account for any anomalous currents flowing within an ocean.

4.5 Definition of a characteristic length and period

Constable et al. [2009] perform modeling studies with a geometrically fixed ocean-coast setting and calculate responses for varying bulk resistivities. At one seafloor station they observe that the cusp in TE mode apparent resistivity vanishes for higher/lower bulk resistivity. We extend this study showing that the localization

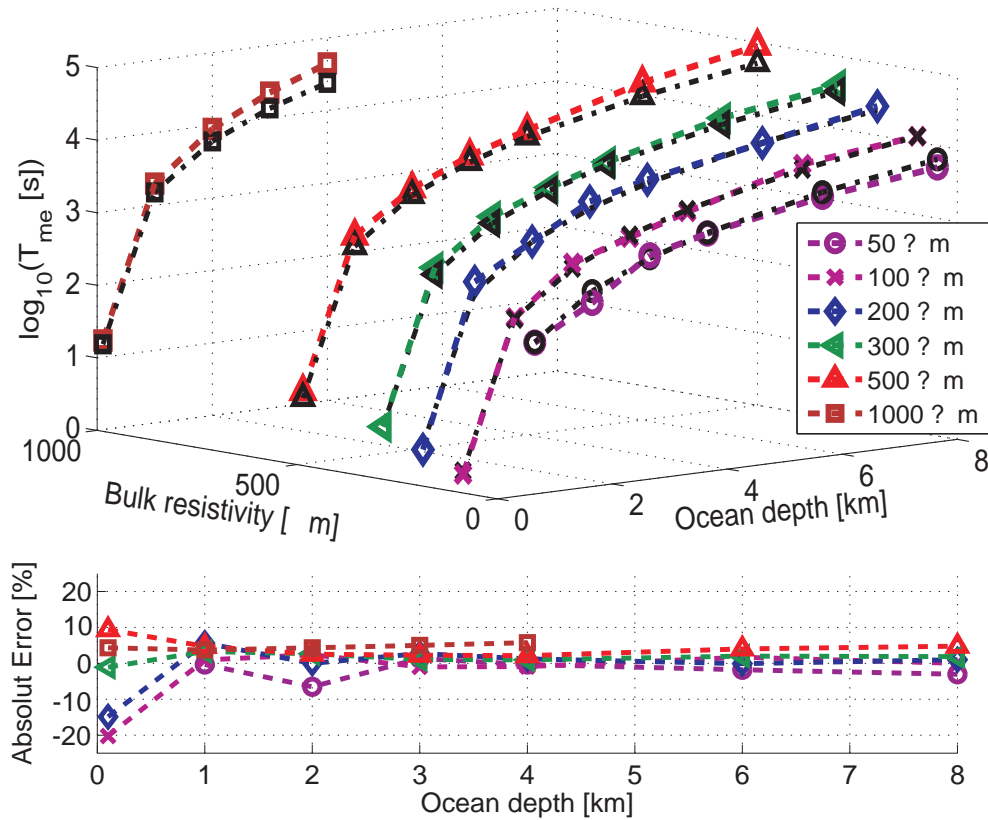


Figure 4.3: Check of validity for Eq. 4.5. Upper panel: Comparison between observed and calculated characteristic period of maximum effect (T_{me}) in dependency of varying background resistivity ρ and ocean depth d (observed periods in black from Table 1, Fig. 7.2). Lower panel: The relative error (percentage) between calculated and observed logarithm of period T_{me} . Almost all points lie within the uncertainty of period detection.

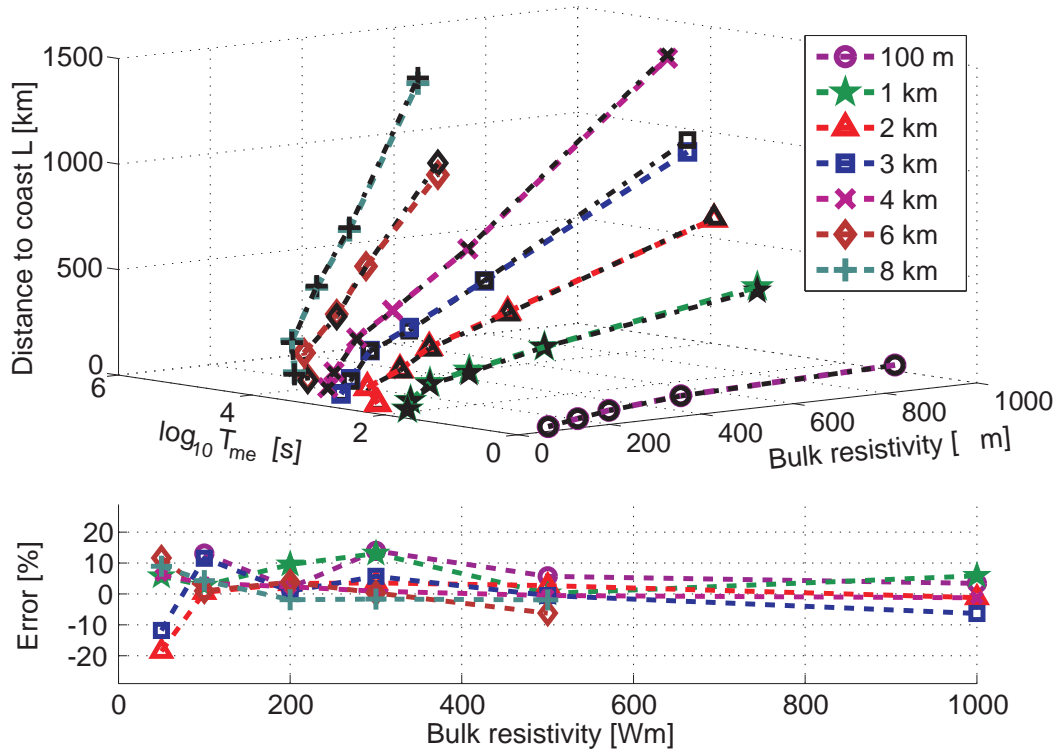


Figure 4.4: Check of validity for Eq. 4.4. Upper panel: Comparison between observed and calculated characteristic distances from coast (L) in dependency of observed period and varying background resistivity (observed distances are displayed in black from Table 1, Fig. 7.2). Lower panel: The relative error (percentage) between calculated and observed distances L . Almost all points lie within the uncertainty of period detection. Outliers are explained by an additional uncertainty due to the detection of the distance from coast, which depends on gridding and station spacing - factors that become negligible for large distances.

of the effect is dependent on bulk resistivity and ocean depth, and never vanishes, but rather “moves”. Hence, we introduce some approximations to describe these relations.

Varying bulk resistivity and depth changes the distance to coast and also the period at which the maximum effect is detected. This is also indirectly observed in the real data set of the Tasman Project; Ferguson [1988] demonstrated that the Tipper magnitudes became highest at certain distances from the coast, which vary with the considered period. In particular, the maximum in response appears to move oceanwards at longer periods, which Ferguson [1988] explains by the gradually deepening ocean.

We calculate several sets of models and vary physical parameters such as ocean depth d (from 100 m to 8 km), homogenous half space resistivity ρ (from 50 to 1000 Ωm), and angle of continental slope using the code of Rodi and Mackie [2001]. The model extent was adapted accordingly to the homogenous background resistivity. To exclude boundary effects, each model was tested by extending its size horizontally and vertically and is regarded sufficient wide if no differences in calculated responses occurred upon any extension. The advantages of the FEMMT by Franke et al. [2007] are not necessary for the further evaluation, as the test models are constructed without topography (with a vertical coast) and electromagnetic fields within the model are also no longer needed. We eventually switched from the finite element code Franke et al. [2007] to the finite difference code of Rodi and Mackie [2001] only because of an increased calculation speed.

The observation for one set of models with a vertical slope is given in Table 1 (Fig. 7.2 in Appendix 7.2). Further information on the models can be found in the table’s caption. The aim was to approximate a characteristic period T_{me} and characteristic distance to the coast L , at which the maximum effect may be expected. Responses for all models were calculated with 20 periods per decade. The uncertainty in detection of the characteristic period is determined by the length of the interval to the next calculated frequency. As the difference between two neighbouring periods equals 10%, the error on the observed period is likewise estimated at 10%.

For a vertical coast (in the following subscripted as “v.c.”), i.e. for an angle of slope $\alpha = 90^\circ$ (nomenclature of Fig. 4.1 a), we found from Table 1 (Fig. 7.2) the following dependencies:

$$L_{v.c.} \approx 0.2 \cdot \sqrt{\rho \cdot T_{me}} \quad (4.1)$$

$$T_{me} \approx 3 \cdot \rho^{0.9} \cdot d^2, \quad (4.2)$$

where $L_{v.c.}$ is measured in [km], T_{me} in [s], d in [km], and ρ in [Ωm].

Substituting Eq. 4.2 into Eq. 4.1 yields

$$L_{v.c.} \approx 0.35 \cdot \rho^{0.95} \cdot d. \quad (4.3)$$

It should be noted that the ocean resistivity was fixed to $0.33 \Omega m$ (the average resistivity of seawater).

We test the validity of Eq. 4.1 by comparing the observed distances in Table 1 (Fig. 7.2) with the calculated distances of Eq. 4.1. The comparison is displayed in Fig. 4.4 in the uppermost panel. The deviation between the observed and calculated distance is displayed in the second panel. The comparison between calculated periods from Eq. 4.2 and observed periods in Table 1 are displayed in Fig. 4.3. Most errors between observed and calculated values lie within error (the uncertainty of determining the period or distance), so we conclude that both equations approximate the observations well.

Models with varying angles of continental slope were also considered (not shown here). We varied the slope angle at a fixed coast position and found that the effect moves laterally with respect to the amount of water displaced. As an example: Assume that a maximum effect is observed at distance $L_{v.c.}$ from a vertical coast. In this case, the amount of water between the maximum effect and the coast is given by $L_{v.c.} \cdot d$.

In the next step we vary the angle α of continental slope without changing the position of the coast, i.e. we are varying α by changing the seafloor projected length of the continental slope “a”. When α (a, respectively) is varied, two changes are observable:

1. The amount of seawater between $L_{v.c.}$ and the (vertical) coast changes (with α increasing, more water is displaced with respect to a fixed reference point on the ocean bottom).
2. The maximum effect moves, respectively, and is now observed at L_α .

When varying α from vertical (90°) to smaller values ($\alpha = 0^\circ$ equals a thin sheet), the amount of water between $L_{v.c.}$ and the coast reduces by $0.5 \cdot a \cdot d$ (half of the right triangle area with sides d and a). This seems to correspond to a shift of the new maximum effect by a distance of $a/2$ away from to the coast: $L_\alpha = L_{v.c.} - a/2$.

4.6 Discussion of the characteristic parameters and introduction to rules of thumb

Since the observability of the maximum effect depends on the ocean depth, analytical solutions of the coast effect using thin-sheet modeling may not account for the observed and modeled effects on the marine side (a thin-sheet has no thickness).

The characteristic length L for a vertical coast is a fraction (less than half) of the skin depth (compare Eq. 4.1 with Eq. 2.13). One implication of this is that if a maximum effect is observed at a station on the ocean bottom, the coast must be accounted for in any inversion, even if it seems to be very far away. Equations 4.2 and 4.3 define a characteristic period and a characteristic distance from the vertical coast, at which the maximum effect should be visible depending on the bulk resistivity and ocean depth. A very crude simplification of Equations 4.2 and 4.3 (using approximation for exponents: $0.95 \approx 1$ and $0.9 \approx 1$) leads to rough but quite catchy rules of thumb:

$$1^{st} \text{ rule of thumb: } T_{max \text{ effect}} = 3 \cdot \rho \cdot d^2, \quad (4.4)$$

$$2^{nd} \text{ rule of thumb: } L_{vertical \text{ coast}} = \frac{1}{3} \cdot \rho \cdot d, \quad (4.5)$$

with T_{me} in [s], ρ in [Ωm], d in [km], $L_{v.c.}$ in [km], and for an average ocean resistivity of $0.33 \Omega m$.

In reality, continental margins are not vertical, but as a first approximation may be treated as triangles. Therefore, when a maximum effect is detected on a continental slope, $L/2$ would be better used for the 2^{nd} rule of thumb. On the other hand, when the characteristic length is used for estimating the bulk resistivity from Eq. 4.5, one should first subtract the projected length of the continental slope (“a”, see nomenclature in Fig.4.1 a) from the observed characteristic length, i.e. $L_{used \text{ for estimation of } Rho} = L_{observed} - a/2$.

Obviously, if the underlying crust and mantle are resistive, these effects can propagate laterally over very large distances. As an example, a resistive basement of $1000 \Omega m$ and an ocean of 4 km depth would move the maximum effect more than a thousand kilometers from the coast. Heinson and Constable [1992] stated that “no part of the global ocean basin is immune to galvanic distortions” caused by the coast effect.

A noteworthy observation arises when comparing the maximum effect in the TE mode with a coastal distortion effect in the TM mode. The currents in the ocean that flow towards the coast (i.e. the TM mode) are deflected downwards through the seafloor because the resistive coast acts as a barrier. The zone of deflected currents

in the TM mode is referred to as “boundary zone” (Cox [1980], Lilley et al. [1989]). Although the TM mode is not dealt with in this study, we assert that Lilley et al. [1989] also approximate crustal resistivity by using a simplified theoretical analysis for describing the TM-mode boundary effect as introduced by Ranganayaki and Madden [1984] and Cox [1980], which is given by:

$$L_{TM \text{ boundary}}^2 = (\sigma_{ocean} \cdot \rho_{bulk}) \cdot d \cdot H. \quad (4.6)$$

$L_{TM \text{ boundary}}$ is the rate at which the anisotropy of the MT impedance in a coastal setting decreases with respect to its TM mode component, as the observation point moves away from the coast. In particular, $L_{TM \text{ boundary}}$ describes a characteristic distance from the coast at which electric currents in the TM mode are deflected (Cox [1980], Lilley et al. [1989]). It is noted that $L_{TM \text{ boundary}}$ also equals the inverse of the parameter tau defined by Berdichevsky and Dimitriev [1976] for measuring the strength of an anomaly at the edge of a 2D inhomogeneity. The term $d \cdot \sigma_{ocean}$ denotes the integrated conductance of an ocean of thickness d and conductivity σ_{ocean} . The term $H \cdot \rho_{bulk}$ denotes the integrated bulk resistivity of thickness H . Eq. 4.6 is certainly different from the characteristic equations or rules of thumb introduced here, as it describes a different characteristic distance (the total extent of the boundary zone). However, we observe an interesting relationship between the maximum effect observed in TE mode and the characteristic distance of the TM mode boundary zone:

Let us approximate σ_{ocean} by $3 \text{ S/m} = 0.33 \text{ } \Omega\text{m}$ and further, estimate the bulk thickness H by the extent of the induction volume, which in the homogeneous case is given by a half sphere with radius of the skin depth (according to Eq.2.13):

$$H_{bulk, \text{ skin depth}} [km] \approx 0.5 \sqrt{T \cdot \rho_{bulk}}. \quad (4.7)$$

Inserting the characteristic period $T_{max-effect}$, as defined in the first rule of thumb, into Eq. 4.7 and transferring the result to Eq. 4.6 yields:

$$\begin{aligned} L_{TM \text{ boundary}} &\approx 1.6 \cdot \rho_{bulk} \cdot d \\ &(\approx 5 \cdot \frac{1}{3} \cdot \rho_{bulk} \cdot d). \end{aligned} \quad (4.8)$$

This is the same order of magnitude as the characteristic length of the maximum effect in the second rule of thumb. Eq. 4.8 implies that the characteristic length of maximum effect in the TE mode lies within the boundary zone of deflected currents in the TM mode. The TM boundary zone ends around five times farther away from the coast than where the maximum effect would be observable in the TE mode.

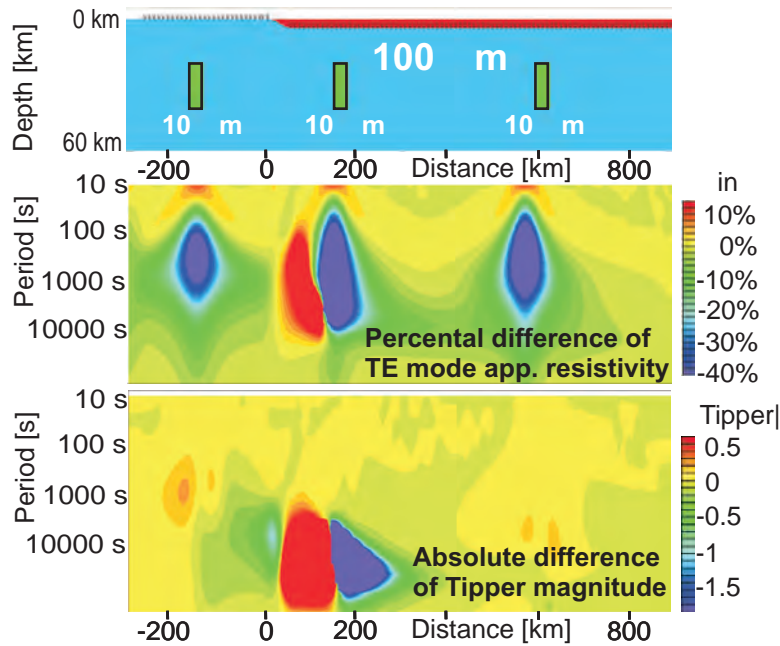


Figure 4.5: Comparison of the sensitivity to conductivity anomalies in different settings. Panel a: Anomalous model containing three conductors, each with a specific resistivity of 10 Ohm m, placed differently in the model: one beneath land stations; the second next to localization of the maximum effect; the third far offshore. In the following panels, responses of this model are compared with responses of the homogeneous case (without anomalies). Second panel: Difference [%] of TE mode apparent resistivity. Bottom panel: Absolute difference of Tipper magnitude. The conductivity anomaly in the vicinity of the maximum effect produces the greatest differences of responses.

4.7 Application to inversion of distorted marine data

A simple test to investigate whether the maximum effect hampers detection of conductivity anomalies is shown in Fig. 4.5. A simple model including the coast is constructed, both with and without anomalies. Responses of anomalous models (Fig. 4.5 a) are then inverted with various homogeneous starting models using a 2-D forward modeling and automated inversion based on the code of Rodi and Mackie [2001]. A smooth inversion was applied, specified by a uniform grid Laplacian operator solving for the smoothest model and minimizing the Laplacian of the model. Trade-off analysis between model roughness and misfit led to a choice of tau between 1 and 10.

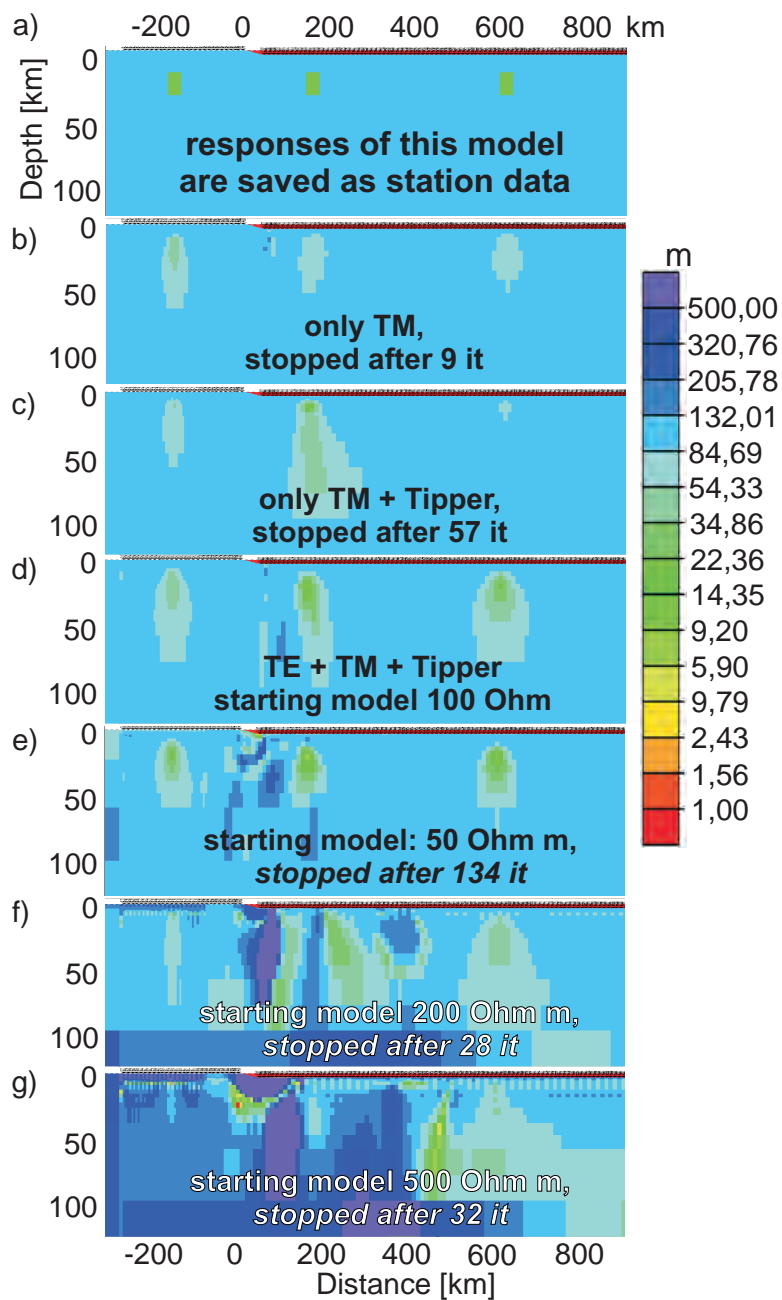


Figure 4.6: Resolvability of conductivity anomalies under different conditions. The anomalous model in the uppermost panel (a) is calculated with 10 % random gaussian noise and responses are saved as station data. Thereafter, several inversions are initiated with an homogeneous half-space and a fixed ocean included in the starting model. Different inversion parameters and starting model resistivities are chosen in panels b)-g).

The inversion only converges satisfactorily under certain conditions. Incorporating TE mode apparent resistivity into the inversion process was vital in order to maintain the model in Fig. 4.5, as it contributes important information regarding the bulk resistivity. However, the TE mode phases can be generally difficult to invert, as some codes cannot handle four quadrants. Therefore, the TE mode phases are de-emphasized in comparison to the TE mode apparent resistivities in order to achieve a sufficient convergence in the inversion process. We discovered that another important condition for a successful inversion was the appropriate choice of a starting model (a starting model as resistive as $500 \Omega m$, for example, would hamper a successful inversion). With such preconditions, and a combined inversion of TE mode, TM mode and Tipper data, the conductivity anomalies can be well resolved, despite the distortion of responses (illustrated in Fig. 4.5 d). An example of an unsuccessful inversion that stopped after only a few iterations, trapped in a local minimum of the process, is shown in Fig. 4.5 e. The subsurface conductivity anomaly affects the TE mode apparent resistivities most severely for stations influenced by the coastal effect: In Fig. 4.5 b, the difference in responses between the anomalous model and the homogeneous half-space are most pronounced in the vicinity of stations that encounter the maximum effect. This implies that the sensitivity is increased to detect conductivity anomalies.

4.8 Conclusions

The coast affects marine responses significantly. The effect in the TE mode and Tipper is most pronounced at a characteristic distance from a (vertical) coast at a characteristic period. Numerical modeling revealed specific dependencies between characteristic values, ocean depth and bulk resistivity. Since a deep ocean combined with a high bulk resistivity may carry the distortion over very large distances (>1000 km), this effect may even be witnessed at large offshore distances and, thus, special care must be taken when inverting marine data at continental margins. A dense coverage of marine stations is essential in order to detect the maximum effect. Upon detection of a maximum effect, the approximations presented here may be used to find an appropriate starting model for an inversion of marine MT data. As such, the coastal effect on marine data does not hamper the detection of subsurface conductivity anomalies. In fact the sensitivity to conductive structures is enhanced for stations in the vicinity of the “maximum effect”.

If the ocean depth and an estimate of bulk resistivity are known, the rules of thumb may also serve to crudely approximate the detection of a maximum effect (the period and the distance from coast).

As an outlook, we hope that our approximations can be verified with an analytical solution.

Chapter 5

Imaging the fluid cycle in the Costa Rican Subduction Zone

This chapter contains a publication in *Nature Geoscience* in its original form. It deals with the modeling results of the data collected in Costa Rica and reveals the journey of the water to the Earth's interior. In the publication, there are several links to more detailed discussions in the online Supplementary information, which is attached to the publication. Please note that both, the publication and its Supplementary information, contain each their own reference lists and refer to their own page numbers.

Concerning the data interpretation, resolution tests and the comparison of other subduction zones in the world, some questions may arise which are not covered in the Supplementary information, but can be found in the appendix: In Appendix 7.5, a selection of other subduction zone findings is presented in respect to the anomalies detected in this study. Appendix 7.3 and Appendix 7.4 provide further resolution tests to the one presented in the Supplementary information. Appendix 7.6 discusses the dimensionality of the recorded electromagnetic fields.

Magnetotelluric image of the fluid cycle in the Costa Rican subduction zone

Tamara Worzewski^{1*}, Marion Jegen¹, Heidrun Kopp^{1,2}, Heinrich Brasse³ and Waldo Taylor Castillo⁴

Fluids entering the subduction zone play a key role in the subduction process. They cause changes in the dynamics and thermal structure of the subduction zone¹, and trigger earthquakes when released from the subducting plate during metamorphism^{2,3}. Fluids are delivered to the subduction zone by the oceanic crust and also enter the oceanic plate as it bends downwards at the plate boundary. However, the amount of fluids entering subduction zones is not matched by that leaving through volcanic emissions⁴ or transfer to the deep mantle², implying possible storage of fluids in the crust. Here we use magnetotelluric data to map the entire hydration and dehydration cycle of the Costa Rican subduction zone to 120 km depth. Along the incoming plate bend, we detect a conductivity anomaly that we interpret as sea water penetrating down extensional faults and cracks into the upper mantle. Along the subducting plate interface we document the dehydration of sediments, the crust and mantle. We identify an accumulation of fluids at ~20–30 km depth at a distance of 30 km seaward from the volcanic arc. Comparison with other subduction zones^{5–14} indicates that such fluid accumulation is a global phenomenon. Although we are unable to test whether these fluid reservoirs grow with time, we suggest that they can account for some of the missing outflow of fluid at subduction zones.

Oceanic crust and lithosphere is hydrated during its creation at mid-ocean ridges¹⁵. Hydration has also been proposed to occur at subduction zones related to the bending of the oceanic plate, which causes extension and normal faulting reaching several kilometres depth below the crust–mantle boundary as inferred from seismic and thermal investigations^{16,17}. Recent numerical experiments show how stress changes induced by the bending oceanic plate can produce vertical pressure gradients along normal faults, favouring downward pumping of fluids and enabling fluids to penetrate to great depths despite their natural buoyancy¹⁸. On subduction, fluids in the hydrated slab are released in a series of metamorphic reactions^{2,6}, but their distribution is not well constrained by existing data. Fluid accumulation is associated with electrically low-resistive (conductive) anomalies, because the bulk electrical resistivity of a rock is mainly governed by the amount of interconnected fluid present¹⁹. We use the term fluids for partial melt and for water originated from pores and fractures or from mineral-bound water. Electromagnetic methods, such as magnetotellurics, are sensitive to electric conductivity anomalies associated with fluids and have therefore been widely used to image fluid migration and melt pathways (for example refs 5,6,20).

Numerical studies have shown that onshore–offshore data are a prerequisite to image the hydration–dehydration cycle in

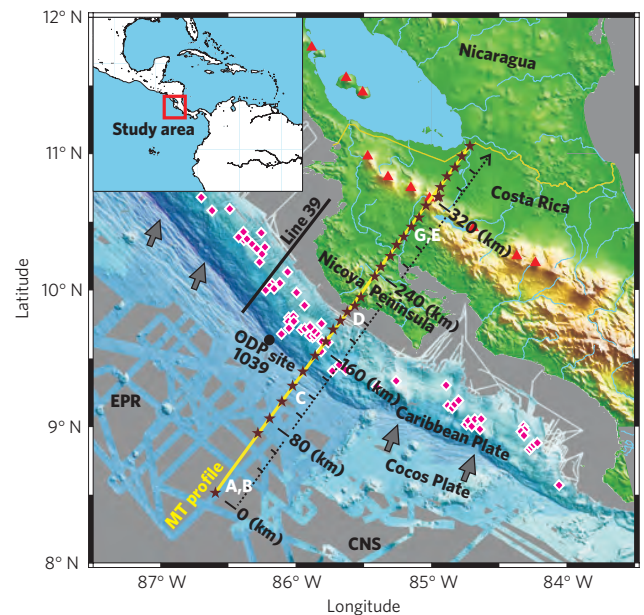


Figure 1 | Location of magnetotelluric (MT) profile on- and offshore Nicoya Peninsula in Costa Rica. Black stars on the yellow profile show station positions. Red triangles: volcanoes. Black dot: borehole position of Ocean Drilling Program (ODP) Leg 170 Site 1039. Black line: bathymetric profile (Line 39) of ref. 16. Grey letters on kilometre markers refer to observed anomalies in Fig. 2. Pink diamonds: fluid seeps. Arrows indicate the direction of plate convergence (for further information see Supplementary Information).

subduction zones²¹. Nearly all previous magnetotellurics surveys on subduction zones were limited to either exclusively land (for example refs 6,20) or marine acquisition (for example ref. 7).

An exception was constituted in the Cascadia subduction zone through the pioneering EMSLAB project in the 1980s (refs 8, 22), which at the time was the largest electromagnetic study incorporating land as well as marine measurements. Hydration processes were not confirmed, because only a few magnetotelluric responses around the trench could be incorporated, but other conductive structures were identified that were attributed to fluids in the subduction zone.

The Costa Rica subduction zone has been widely studied in many aspects involving fluids (see, for example, refs 16,23,24). Offshore Costa Rica, the Cocos plate that is generated at the East Pacific

¹SFB 574 at Kiel University/IFM-GEOMAR, Wischhofstr. 1-3, 24148 Kiel, Germany, ²IFM-GEOMAR, Wischhofstr. 1-3, 24148 Kiel, Germany, ³Free University of Berlin, Fachrichtung Geophysik, Malteserstr. 74-100, D-12249 Berlin, Germany, ⁴Instituto Costarricense de Electricidad, UEN Proyectos y Servicios Asociados Area de Amenaza y Auscultación Sísmica y Volcánica, Sabana Norte, Apdo 10032-1000, San José, Costa Rica.

*e-mail: tworzewski@ifm-geomar.de.

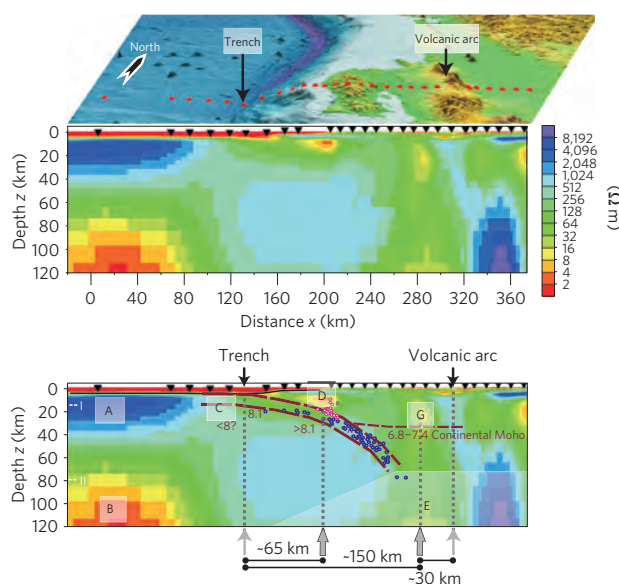


Figure 2 | Two-dimensional inversion model of electrical resistivity below the Costa Rican subduction zone. Upper panel: station map including bathymetry. For the location, refer to Fig. 1. Middle panel: inversion result. The electrical resistivity given in ohm metre ranges from conductive (least resistive) in red to highly resistive in blue, that is, red to yellow colours indicate high to moderate conductivity (low resistivity) associated with fluids. The colour scale is logarithmic. Lower panel: seismic information superimposed on inversion result—seismic boundaries (dashed brown) and velocities; blue circles, interplate earthquakes; pink circles, seismogenic-zone earthquakes from ref. 25. The transparent area is of limited significance owing to lower resolution. I and II indicate transition to the mantle and electrical asthenosphere, respectively.

Rise in the west and the Cocos-Nazca Spreading Centre in the south, is thrust beneath the Caribbean plate (Fig. 1) at a rate of approximately 88 km Myr^{-1} . Ref. 25 has imaged the seismogenic zone extending from 26–28 km underneath Nicoya Peninsula.

In 2007–2008 we conducted a long-period magnetotellurics experiment along a 380-km-long profile extending onshore–offshore Nicoya Peninsula with a station spacing dense enough to resolve conductive structures that are small compared with profile length.

The onshore–offshore magnetotellurics data were inverted to provide a comprehensive electrical resistivity image of the deep Costa Rican subduction zone, enabling us to image both hydration and fluid release from the incoming oceanic plate into the overriding plate.

The farthestmost marine stations southwest of the trench image normal oceanic lithosphere in terms of electrical resistivity (anomaly A in Fig. 2), as has also been observed in other marine magnetotellurics surveys (for example at the East Pacific Rise²⁶). Low-resistive ($<10 \text{ } \Omega \text{ m}$), water-saturated oceanic sediments overlay pillow lavas and sheeted dykes with increasing resistivities until a very high resistivity ($>1,000 \text{ } \Omega \text{ m}$) is reached in the upper mantle. At lithospheric depths beneath 40 km, resistivities decrease again owing to increasing temperatures²⁷. Low-resistive anomaly B in Fig. 2 beneath $\sim 80 \text{ km}$ depth is consistent with other oceanic magnetotellurics studies on oceanic plates²⁸, and could possibly be associated with an asthenosphere containing minor amounts of partial melts.

On underthrusting, the highly resistive oceanic lithosphere exhibits a moderate reduction in electrical resistivity down to deep-crustal and possibly upper-mantle regions ($>1,000 \text{ } \Omega \text{ m}$ to $\sim 50 \text{ } \Omega \text{ m}$ anomaly C in Fig. 2). Multibeam bathymetry and multichannel

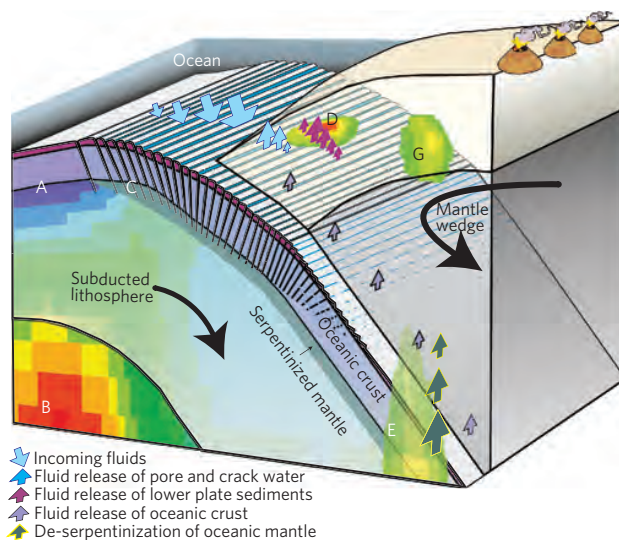


Figure 3 | Schematic interpretation of inversion results. Straight arrows indicate different pathways and origins of fluids. The cool incoming plate (A) is topped by water-saturated sediments (pink layer on top of subducting slab) and overlays a hot asthenosphere (B). On bending, the oceanic crust is hydrated possibly to upper-mantle depths (C). Anomaly D is associated with release of mineral-bound water and G with accumulation of crustal fluids caused by fluid release within the oceanic crust or heating and dewatering of the mantle wedge. The weakly resolved anomaly E can be associated with de-serpentinization of oceanic mantle.

seismic reflection images northwest of Nicoya Peninsula ('Line 39' in Fig. 1) reveal that bending-related faulting of the incoming plate creates a pervasive tectonic fabric, penetrating at least 20 km into the crust and upper mantle, promoting serpentinization of the upper mantle¹⁶. Reduced seismic velocities in the upper mantle along a seismic refraction array²⁵ also point to serpentinized mantle but could not be resolved well because of a lack of ocean-bottom seismometers. Serpentinization of the mantle produces an increase in porosity leading to a reduction in electrical resistivity²⁹, which may additionally be reduced through the production of networks of electrically conducting magnetite²⁹. The reduction in resistivity of the upper mantle from values exceeding $1,000 \text{ } \Omega \text{ m}$ to approximately $50 \text{ } \Omega \text{ m}$ on bending as observed in our study (anomaly C in Fig. 2) is in agreement with laboratory experiments on dry and serpentinized mantle rocks²⁹.

Farther landward in the subduction process, hydration is superseded by dehydration. Two mechanisms account for fluid release in the subduction channel, that is, the region between the subducting and overriding plates. (1) Expulsion of free fluids from gradually closing fractures and pore spaces along the upper few kilometres of the subduction channel. (2) Release of mineral-bound water along the deeper portion of the subduction channel²³. We cannot structurally resolve the subduction channel with magnetotellurics, but we can image fluid accumulations associated with dehydration processes in the subduction channel. The expulsion of free fluids is documented in a shallow, not well-resolved, very conductive (low-resistive) zone along the décollement zone (in Fig. 2 red-coloured region positioned at 130–160 km between anomalies C and D). Release of mineral-bound water is most probably associated with the distinct and well-resolved anomaly D at 12–15 km depth, where resistivity values drop from around 50 to $5\text{--}10 \text{ } \Omega \text{ m}$. This depth corresponds to the geochemically derived source depth of fluids produced through clay demineralization, which flow upward along deep-seated faults and exit at mid-slope fluid seeps²³. Although we do not directly detect

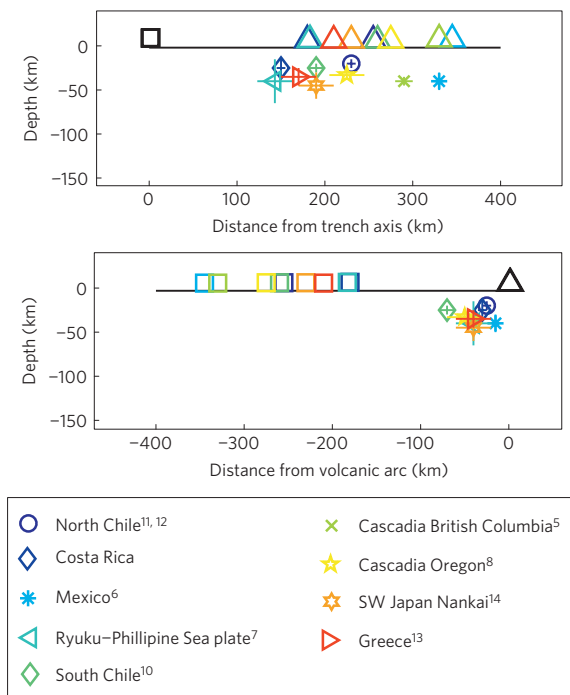


Figure 4 | Global overview of the forearc conductor (anomaly G) appearances in subduction zones. Triangles depict the volcanic arc; squares represent the trench axis; colours correspond to different subduction zones (see the legend on the right). Error bars are assigned according to the uncertainty of the centre of the conductive zone. See Supplementary Information for further details. Upper left panel: distances of anomalies G and volcanic arcs from trench axes are plotted (trench axes are aligned to zero). Lower left panel: distances of anomalies G and trench axes from volcanic arcs are plotted (volcanic arcs are aligned to zero).

such an upward fluid flow owing to limited resolution, mid-slope fluid seeps are indeed observed along our profile (see Fig. 1). Estimates derived from the resistivity values and anomaly size are compatible with a fluid volume of 1–6 km³ per km of along-strike trench, which would amount to about 5–34% of the fluids that are estimated to have entered the subduction zone over the past 10 Myr on the basis of information from Ocean Drilling Program leg 170 (see Supplementary Information).

Underneath anomaly D a cluster of earthquakes defining the seismogenic zone²⁵ is observed, showing that the transition from aseismic to seismogenic behaviour correlates with a declining amount of fluid³⁰.

Further prominent conductivity anomalies are revealed by the land data. The high-conductivity zone located ~150 km landward of the trench, at 30 km distance to the volcanic arc at ~20–30 km depth, is termed anomaly G in accordance with ref. 9. The temperature at this depth is not sufficiently high to produce or retain substantial melt fractions. This anomaly is most probably associated with fluid release from the oceanic crust² or heating and dewatering of the upper part of the serpentinitized mantle wedge. Our estimate on the basis of the size and resistivity of the anomaly amounts to 0.5–2.5 km³ of fluid per kilometre trench length (see Supplementary Information).

Their preliminary resistivity modelling⁹ required a high-resistivity zone underneath anomaly G. However, by adding offshore data and not applying horizontal smoothing during the inversion as previously done, we now find that a zone of reduced resistivity (anomaly E beneath 70 km under anomaly G) proves stable in the inversion process.

Resolution tests confirm a slightly better fit for a reduced-resistivity zone below 70 km depth in the current study (see Supplementary Information). The transparent faded region in Fig. 2 indicates where sensitivity is reduced in the model. However, numerical models showing an effective dehydration of serpentinitized mantle and crust (de-serpentinization) at more than 100 km depth² suggest that this anomaly is geochemically feasible and could therefore be associated with de-serpentinization.

The diagram in Fig. 3 summarizes the interpreted hydration–dehydration cycle: in the hydration part on bending, deep faults are created, enabling water to penetrate to mantle depths (C). Water is partially stored in cracks and pores (free fluids) as well as mineral (chemically) bound in oceanic sediment, crust and (serpentinized) mantle. In the dehydration part, on subduction farther downward, water is released and expelled from cracks and pores within the first few kilometres. Additionally, water released from shallow phase transition reactions in sediment is accumulated at shallow depths (D). Further in the subduction process, crustal and mantle dehydration are associated with deep-crustal fluid accumulation (G). An effective dewatering through de-serpentinization at depths greater than ~100 km might be associated with a weakly resolved anomaly at depth (E).

Anomaly G in the overriding plate deserves more attention, because comparable anomalies of varying resolution are observed in mature subduction zones that have developed typical surface expressions such as volcanic arcs around the world: land magnetotellurics surveys in South Chile¹⁰, in British Columbia⁵ and in Oregon⁸ (Cascadia), in Mexico⁶, in North Chile^{11,12}, in Greece¹³ and in Japan (Nankai)¹⁴, as well as a marine magnetotellurics survey in Japan (Ryukyu Trench)⁷, image conductive (low-resistive) zones in comparable distances to the volcanic arcs. The observed anomalies are summarized in Fig. 4; they are located in similar distances from volcanic arcs and are located at similar depths (20–40 km from volcanic arcs in 20–40 km depth, except for outlier South Chile). Details on the various subduction zone anomalies are given in the Supplementary Information.

The conductivity anomaly G thus represents a globally existent fluid accumulation and must be linked to fundamental dynamical processes in subduction zones. Output fluxes determined for the forearc fluid venting and the volcanic arc emissions typically account for less than half of the input flux of free or mineral- and chemically bound fluids in subducting sediment and hydrated crust and mantle, although volatile losses from intrusive magmatism are very poorly constrained⁴. Numerical modelling of fluid release during metamorphic reactions in the subducting slab suggests that 20–40% of the water input may be transferred into the deep mantle². These numbers indicate that a fraction of about 10–30% of the water input flux is not yet accounted for; therefore, a possible extra sink for water flux may be these forearc conductivity anomalies (G).

Our study images fundamental hydration and dehydration processes of subduction zones beyond a regional scale. Hydration and serpentinitization of the upper mantle^{16,18} and effective dewatering of slab components in distinct steps^{2,6} have been proposed previously using different data and modelling schemes. Our results synergize these aspects into a geographically and methodologically unifying model of the fluid cycle through subduction zones in its entirety.

Furthermore, our findings suggest a possible global fluid sink in the forearc (anomaly G) that may account for the discrepancies between input and output flux along subduction zones.

Method summary

Magnetotellurics is a passive electromagnetic geophysical method for imaging the electrical-resistivity structure (reciprocal to conductivity) of the subsurface.

Naturally occurring fluctuations of the Earth's magnetic external field induce electric currents whose strength and distribution depend on the subsurface resistivity. Variations of the horizontal electric and three-component magnetic

fields are recorded on the ocean bottom and land surface to derive a spectral, complex-valued impedance tensor \underline{Z} given by $\underline{Z} \cdot \mathbf{H}_h = \mathbf{E}_h$, where \mathbf{E}_h and \mathbf{H}_h denote the frequency-dependent horizontal electric (\mathbf{E}_h) and magnetic (\mathbf{H}_h) fields. An extra spectral, complex-valued transfer function, the magnetic tipper \mathbf{T} is given by $\mathbf{T} \cdot \mathbf{H}_h = H_{\text{vertical}}$. In a homogenous half-space, the so-called skin depth δ is a crude estimate of detection depth with $\delta \approx 0.5\sqrt{\rho t}$ in kilometres (where t is the period and ρ is the bulk resistivity). At periods shorter than approximately 1 s, seafloor electromagnetic signals are very small. This is due to the high conductivity of the sea water above, which causes attenuation according to skin depth and thus reduces the resolvability of shallower sea-bottom features.

In a perfect two-dimensional setting, the strike-rotated complex impedance tensor contains only off-diagonal elements, which show two decoupled modes: the transverse-electric mode, that is, electric field parallel to strike, and the transverse-magnetic mode, that is, magnetic field parallel to strike. The transverse-electric and transverse-magnetic impedance transfer functions and the tipper contain information on the resistivity (or conductivity) distribution within the Earth and are used as input data for modelling.

For the offshore campaign we used marine magnetotellurics instruments newly developed at IFM-GEOMAR and the University of Kiel. The marine instruments contain, in addition to a three-component fluxgate magnetometer and two E -field channels, a dual-axis tilt meter for measuring pitch and roll (the displacement from the horizontal). The period bandwidths of the marine responses vary owing to the depth-dependent absorption effect of the conductive ocean as well as motion-induced noise through tidal currents and waves.

The motion-induced noise was directly visible through the tilt-meter measurement, which showed strongest motion close to the coast: station *m01* eventually tilted beyond measurement range and station *m02* was even lost (see Supplementary Fig. S2 for positions). We cut out all noisy sections as defined by the tilt-meter measurements and only used time-series sections that were uncorrelated to the tilt variations and at the same time coherent with a reference station. This resulted in shorter sections for stations close to the coast, which were more affected by tidal waves (and therefore show shorter periods in comparison to stations farther offshore, as can be seen in Supplementary Fig. S3). Nevertheless, a long recording time of several months enabled the selection of many sections, which were then processed together.

The onshore campaign was carried out by ref. 9. Dimensionality and strike analysis of land data proved the validity of a two-dimensional assumption and determination of strike angle. More technical details and resolution tests are provided in the Supplementary Information.

Received 3 March 2010; accepted 19 November 2010;
published online 19 December 2010

References

1. Peacock, S. A. Fluid processes in subduction zones. *Science* **248**, 329–337 (1990).
2. Ruepke, L. H., Morgan, J. P., Hort, M. & Connolly, J. A. D. Serpentine and the subduction zone water cycle. *Earth Planet. Sci. Lett.* **223**, 17–34 (2004).
3. Hacker, B. R., Peacock, S. M., Abers, G. A. & Holloway, S. D. Subduction factory 2. Are intermediate-depth earthquakes in subducting slabs linked to metamorphic dehydration reactions? *J. Geophys. Res.* **108**, 2030 (2003).
4. Jarrard, R. D. Subduction fluxes of water, carbon dioxide, chlorine, and potassium. *Geochem. Geophys. Geosyst.* **4**, 8905 (2003).
5. Soyer, W. & Unsworth, M. Deep electrical structure of the northern Cascadia (British Columbia, Canada) subduction zone; implications for the distribution of fluids. *Geology* **34**, 53–56 (2006).
6. Joedicke, H. *et al.* Fluid release from the subducted Cocos plate and partial melting of the crust deduced from magnetotelluric studies in southern Mexico: Implications for the generation of volcanism and subduction dynamics. *J. Geophys. Res.* **111**, B08102 (2006).
7. Shimakawa, Y. & Honkura, Y. Electrical conductivity structure beneath the Ryukyu trench-arc system and its relation to the subduction of the Philippine sea plate. *J. Geomagnetism Geoelectricity* **43**, 1–20 (1991).
8. Jiracek, G. R., Curtis, J. H., Ramirez, J., Martinez, M. & Romo, J. Two-dimensional magnetotelluric inversion of the EMLAB Lincoln line. *J. Geophys. Res.* **94**, 14145–14152 (1989).
9. Brasse, H. *et al.* Deep electrical resistivity structure of northwestern Costa Rica. *Geophys. Res. Lett.* **36**, L02310 (2009).
10. Brasse, H. *et al.* Structural electrical anisotropy in the crust at the South–Central Chilean continental margin as inferred from geomagnetic transfer functions. *Phys. Earth Planet. Inter.* **173**, 7–16 (2009).
11. Schwalenberg, K., Haak, V. & Rath, V. The application of sensitivity studies on a two-dimensional resistivity model from the Central Andes. *Geophys. J. Int.* **150**, 673–686 (2002).
12. Brasse, H. *et al.* The Bolivian Altiplano conductivity anomaly. *J. Geophys. Res.* **107**, 2096 (2002).
13. Galanopoulos, D., Sakkas, V., Kosmatos, D. & Lagios, E. Geoelectric investigation of the Hellenic subduction zone using long period magnetotelluric data. *Tectonophysics* **409**, 73–84 (2005).
14. Ichiki, M., Sumitomo, N. & Kagiya, T. Resistivity structure of high-angle subduction zone in the southern Kyushu district, southwestern Japan. *Earth Planet. Space* **52**, 539–548 (2000).
15. Mével, C. Serpentinization of abyssal peridotites at mid-ocean ridges. *C. R. Geosci.* **335**, 825–852 (2003).
16. Ranero, C. R., Morgan, J. P., McIntosh, K. & Reichert, C. Bending-related faulting and mantle serpentinization at the Middle America trench. *Nature* **425**, 367–373 (2003).
17. Grevemeyer, I. *et al.* Heat flow and bending-related faulting at subduction trenches: Case studies offshore of Nicaragua and Central Chile. *Earth Planet. Sci. Lett.* **236**, 238–248 (2005).
18. Faccenda, M., Gerya, T. V. & Burlini, L. Deep slab hydration induced by bending-related variations in tectonic pressure. *Nature Geosci.* **2**, 790–793 (2009).
19. Schmeling, H. Numerical models on the influence of partial melts on elastic, anelastic and electrical properties of rocks. Part II: Electrical conductivity. *Phys. Earth Planet. Inter.* **43**, 123–136 (1986).
20. Wannamaker, P. E. *et al.* Fluid and deformation regime of an advancing subduction system at Marlborough, New Zealand. *Nature* **460**, 733–736 (2009).
21. Evans, R. L. & Chave, A. D. On the importance of offshore data for magnetotelluric studies of ocean-continent subduction systems. *Geophys. Res. Lett.* **29**, 1302 (2002).
22. Wannamaker, P. E. *et al.* Resistivity cross section through the Juan de Fuca subduction system and its tectonic implications. *J. Geophys. Res.* **94**, 14127–14144 (1989).
23. Hensen, C., Wallmann, K., Schmidt, M., Ranero, C. R. & Suess, E. Fluid expulsion related to mud extrusion off Costa Rica—a window to the subducting slab. *Geology* **32**, 201–204 (2004).
24. Husen, S., Quintero, R., Kissling, E. & Hacker, B. Subduction-zone structure and magmatic processes beneath Costa Rica constrained by local earthquake tomography and petrological modeling. *Geophys. J. Int.* **155**, 11–32 (2003).
25. DeShon, H. R. *et al.* Seismogenic zone structure beneath the Nicoya Peninsula, Costa Rica, from three-dimensional local earthquake P- and S-wave tomography. *Geophys. J. Int.* **164**, 109–124 (2006).
26. Baba, K., Chave, A. D., Evans, R. L., Hirth, G., Mackie, & R. L., Mantle dynamics beneath the East Pacific Rise at 17°S: Insights from the Mantle Electromagnetic and Tomography (MELT) experiment. *J. Geophys. Res.* **111**, B02101 (2006).
27. Constable, S. C. & Duba, A. The electrical conductivity of olivine, a dunite, and the mantle. *J. Geophys. Res.* **95**, 6967–6978 (1990).
28. Heinson, G. Electromagnetic studies of the lithosphere and asthenosphere. *Surveys Geophys.* **20**, 229–255 (1999).
29. Stesky, R. M. & Brace, W. F. Electrical conductivity of serpentinized rocks to 6 kilobars. *J. Geophys. Res.* **78**, 7614–7621 (1973).
30. Ranero, C. R. *et al.* Hydrogeological system of erosional convergent margins and its influence on tectonics and interplate seismogenesis. *Geochem. Geophys. Geosyst.* **9**, Q03S04 (2008).

Acknowledgements

This publication is contribution No 187 of the Sonderforschungsbereich 574 'Volatiles and fluids in subduction zones' at Kiel University. The logistical support of Guillermo Alvarado and the Instituto Costarricense de Electricidad is appreciated. We would further like to thank the Costa Rican Coast Guard for providing us with ship time and the German embassy in Costa Rica for intercession. We thank B. Lewitz, Y. Dzierma, R. Kroth, P. Schroeder, T. Brandt and C. Jung for their great help in the campaign. We also thank D. Scholl and two anonymous reviewers for comments that helped to substantially improve this paper. Thanks to A. Freundt and S. Kutterolf for discussions. The study was funded by the German Science Foundation.

Author contributions

T.W. and M.J. designed this study, developed marine magnetotellurics instruments, carried out the marine experiment, analysed the data, interpreted the results and wrote the paper; H.K. interpreted the results and wrote the paper; H.B. designed this study, carried out the land experiment, analysed the data and interpreted the results; W.T. provided geologic background information and logistical support, which was vital for the whole experiment.

Additional information

The authors declare no competing financial interests. Supplementary information accompanies this paper on www.nature.com/naturegeoscience. Reprints and permissions information is available online at <http://npg.nature.com/reprintsandpermissions>. Correspondence and requests for materials should be addressed to T.W.

Section 1 contains more technical details on data analysis and resolution tests. In section 2 we are presenting details of other subduction zone surveys in which anomaly G has been observed and which confirm the global appearance of anomaly G as summarized in Fig 4. In section 3 we are providing details on flux estimations which are discussed in the main text.

1. Technical details on data analysis and resolution tests

In this section we provide further information concerning the data analysis and inversion process. The MT and tipper transfer functions over periods of 20-10,000 s were derived using magnetotelluric response function estimations after [31]. The MT data was inverted using a combination of 2-D forward modelling and automated inversion with the algorithm of ref [32].

For the inversion we used a regularization parameter of three as determined by a trade-off analysis between misfit and model roughness (Supplementary Figure 1). In Supplementary Figure 2 the positions of the marine and land stations are shown on the map for further referencing.

The data recorded during the campaigns and the data predicted by the inverted electrical resistivity model are shown in Supplementary Figure 3 (for marine responses) and Supplementary Figure 4 (for land responses). Stations close to the coast in shallower water are more affected by motion induced noise through ocean currents and tidal waves. This is observable in data quality which ranges from very good on top left (far offshore, m11) to

noisy on bottom right (closest to coast, m03). For seafloor station m06 we could only include the tipper data due to an electric field failure.

The so-called coast effect, i.e. the effect of a large conductivity contrast between ocean and land, causes a severe distortion in the marine MT data, which leads to an especially atypical TE mode phase behaviour such as a sign change in phase at certain periods. “Negative phases” have also been observed and explained by [33] and [34]. In the inversion we therefore emphasized amplitudes of TE mode apparent resistivities in the marine MT data in comparison to marine TE mode phase data. However, this leads to an artificially overall lower RMS level in the marine data compared to the land data. Seafloor bathymetry and an ocean resistivity of 0.3 Ohm m were incorporated in the inversion models as fixed constraints. Near-surface information derived from seismic profile and borehole data was used to set a priori 500 m of sediments on top of the incoming plate (after [35]) with a resistivity of ~1 Ohm m (after [36]). The initial input model for the inversion was constructed from a subducting resistive layer of 70 km thickness representing the oceanic lithosphere and then further refined by subsequent combination of individual TM, TE and Tipper inversions to assure convergence in the inversion process.

The model of Fig. 2 was then obtained by a joint inversion of Tipper, TE and TM mode data.

The most prominent conductivity anomalies of the model (B, C, D, E and G) are recovered after several inversions and various combinations of TE, TM and Tipper data. This is an indication that these anomalies can be considered as stable and required by the data.

No standard method exists in MT for resolution analysis. Our approach has been to test the requirement of anomalies B, C, D, G and E in the final resistivity model by performing forward modelling studies.

Supplementary Figure 5 panel a) shows blocks which roughly delineate the conductivity anomalies. We vary in our end model the resistivities within these blocks. In separate graphs we overlay the responses for these different models onto the data from stations which are sensitive to the feature and list the RMS of the station data (TE, TM mode and tipper) for the different models.

Supplementary Figure 5 panel b) shows the overlay of different graphs and corresponding RMS at the seafloor station m05. The box C was edited in six different runs to get different resistivity values (10; 50; 100; 500; 1000 and 10000 Ohm m). The corresponding responses are given in rainbow colours; the black lines denote the observed data. Predicted data for an average resistivity value of 50 Ohm m (yellow) in the box C produces the best overall fit for the three responses with a station RMS of 3.53 (please note that “overall” in this context denotes a combined fit for TE mode, TM mode and Tipper data at one station). Increasing resistivities (colours from red to blue) produce an increasing RMS at that station, with decreasing resistivity the RMS misfit deteriorates quickly.

The misfit of the responses to the data can be qualitatively observed in the graphs or alternatively directly by the observing changes in RMS of that station with respect to the changing resistivities in the boxes. In panels c) – e), we therefore only show the RMS changes with respect to the resistivity variations of single stations which are in each case sensitive to the conductivity anomaly.

Panel c) shows the resolution of anomaly D from sites ‘M03’ to ‘cat’, which are sensitive to anomaly D. The “overall misfit” here refers to the misfit of TE, TM mode and Tipper responses at one single station (not to be confused with the total RMS of all stations). We show the overall misfits (RMS) at each site, which are compared to the misfit produced by the final model (black line). For this we used, due to the incorporation of M03, the marine definition of the RMS. With rising resistivities (graded in light blue to deep blue), the RMS consistently increases. The best fit (smallest RMS) is reached for 5-10 Ohm m (red and orange curves). This test was also run with smoothed out blocks instead of rectangular blocks yielding the same conclusions.

In the same way, we test anomaly E in panel d) for station ‘sam’ to ‘fro’, which are sensitive to anomaly E. Again, rising resistivities (graded in light blue to deep blue) lead to increasing RMS (note that the RMS level is higher due to the use of the land definition of the RMS). The best overall fit along the station sequence is reached for a moderate resistivity of 30-100 Ohm m of anomaly E. RMS at individual stations might be reduced further if the resistivities are smaller than 30 Ohm m. But the changes in RMS are very small, since resolution is limited in this region. We would therefore only like to conclude that within this model rather a conductor than a resistor is required at these depths.

In panel e) we test the resolution of anomaly G for stations ‘mot’ to ‘maq’, which are sensitive to this anomaly. The observation is the same: With rising resistivities, the RMS consistently increases. Best fits are obtained for resistivities between 15 and 10 Ohm m,

resistivities outside of this range lead to a higher misfit, confirming that the data are sensitive to this anomaly.

In panel f) the resolution of anomaly B is investigated for stations ‘m11’ to ‘m07’, which are most sensitive to this anomaly. The best fits within this model are obtained for an average resistivity of 5 Ohm m.

2. Details on Forearc Conductivity Anomaly G as observed in other subduction zones:

Previous MT studies on mature subduction zones worldwide have shown the mid-plate conductive anomaly, termed anomaly G in this paper (“mature” refers to a fully developed volcanic arc including a visible trench, a counterexample would be the South Island of New Zealand [4], see below). It is always found at nearly the same distance from the volcanic arc and at similar depths (Figure 4). However, this global presence and thus the importance of the anomaly have not yet been recognized. As a result, anomaly G has been attributed to a variety of causes. In the following section we present a list of all respective published surveys which had sufficient resolution to image G. This should be a complete list to our knowledge. An uncertainty concerning the centre of the respective locations, as taken from these studies which present final resistivity models with varying smoothness as well as resolution, is represented by error bars assigned to anomaly G.

In South Chile, a conductor observed ~190 km landward from the trench and ~70 km seaward of the volcanic arc at a depth of 20-30 km was associated with the Lanalhue Fault [25].

In the Cascadia subduction zone of British Columbia, two major conductors were detected in a MT land survey; one of them is centred ~290 km landward from trench at ~40 km distance from the volcanic arc and at a depth of 30-50 km. Ref [5] termed this anomaly A and attributes it to free aqueous fluids being present in the mantle wedge conceding that the EMSLAB experiment had shown an anomaly of similar conductivity, though at a slightly shallower depth in the lower crust, which also had been interpreted as a zone of upward-migrating fluids released from the slab [14], [40]. The EMSLAB profile is ~450 km south from [5] in Oregon, one of the first 2-D MT inversions was performed on the land data by [15] who found a well-developed conductive zone centred at about 30-35 km depth, ~225 km landward of the trench and ~50 km seaward of the volcanic arc.

In the Mexican subduction zone a land MT profile crossing the volcanic arc (profile B-B') was inverted to a strongly horizontally smoothed resistivity model, which contains an elongated anomaly centred ~30 km at a depth of 20-50 km seaward of the volcanic arc [6]. The anomaly was associated with water freed by a series of metamorphic reactions (blueschist-eclogite, chlorite and amphibole); comparable to anomaly G here. The interpretation of conductive anomalies on a second Mexican profile (A-A') seems more difficult, as the volcanic arc on profile A-A' is not clearly visible (there is only one singular volcano at the end of the profile). Therefore, the conductive anomaly of profile A-A' is not

taken into account. Yet we would like to draw attention to a conductive zone that begins about 40 km seaward of this volcano and continues on to the end of the profile at the volcano itself, spanning up to 30 km of depth, which the authors associate with a sedimentary basin overlain on possible extinct volcanism.

In the North Chilean subduction zone, [26] and [27] observe a conductor ~230 km landward of the trench and 30 km seaward of the volcanic arc at depths of 15-25 km, with a well conducting zone underneath it at a depth of >100 km depth.

In Japan at the Philippine Sea plate subduction zone beneath Kyushu, a conductive block was observed at a depth of 30 km in the forearc region [29], ~190 km from the trench (Nankai Trough), ~40 km from the volcanic arc. The conductivity anomaly was attributed to the presence of fluids and serpentinites, however, due to the lack of marine data, this particular anomaly is not well resolved [29].

A further survey in Japan, exclusively using marine MT over the Ryukyu trench, revealed two isolated highly conductive zones [13], one of them above of the subducting plate at depths of ~20-60 km, centred between trench and volcanic arc axes (~140 km from the trench and ~40 km from the extrapolated volcanic arc).

In the Hellenic subduction zone in Greece, a long-period MT experiment with responses exceeding 50 s was conducted [28] to image mantle conductivity anomalies at depths larger

than ~35 km. Although resolution for crustal conductors is very low, a conductive zone 140-170 km landward of the trench, 30-60 km seaward of the volcano and at a depth of 50 km has been identified by the data.

Recently, MT results from New Zealand's South island, which is a very young subduction zone with neither a volcanic arc yet developed nor a clearly visible trench, have been published [4]. The lack of clear definition of the reference point chosen makes it difficult to include the results of this study into this general examination. However, it shows a similar zone of enhanced conductivities which the authors interpret to represent fluids that have migrated upward into the deep crust from source areas of progressively higher metamorphic grade along the subduction zone, creating faults and triggering earthquakes. But as conductivity zones observed there have smaller values in comparison to the conductive anomalies of all other mature subduction zones summarized above, one may infer that subduction in New Zealand's South island hasn't fed the upper mantle with enough water yet to activate volcanism.

3. Details on fluid estimation derived from resistivity data

In this section we present details on the fluid amount estimations that have been included in the main text. It should be noted beforehand, that estimations of fluid content from resistivity values are qualitative only, since they are based on assumptions about resistivities of pore fluid and matrix as well as the geometric distribution of fluids.

3.1 Fluid entry and release estimation of mineral bound water (resistivity anomaly D)

Assuming a sedimentary nature of the material in the subduction channel, we estimate the fluid content in anomaly D, which is associated with the dehydration of mineral bound water, using the experimentally derived Archie's law [41]:

$$\rho_{bulk} = a \cdot \Phi^{-m} \cdot S^{-n} \cdot \rho_{fluid} \quad (\text{Equation 1}).$$

It relates the bulk resistivity of the structure to its porosity fraction ϕ , fluid saturation S and resistivity of the pore fluid ρ_{fluid} . Parameters a and m vary depending on cementation of the sediments. We assume values of $m=1.94$ and $a=1.62$, which are compatible with well compacted sediments with a pore fraction [43] and furthermore fully fluid saturated pores, i.e. $S=1$. Anomaly D is associated with a drop of resistivity by a factor of 5 with respect to the background resistivity (from at least 50 Ohm m for the background to at most 10 Ohm m within the anomaly). Assuming that the pore fluid resistivity is the same within and outside the anomaly, the drop in resistivity requires an at least 2 fold increase in fluid-filled pore fraction independent of the absolute value of pore fraction or resistivity of fluid. Non-linear variations of physical properties along the subduction channel may account for the fluid increase. High quality seismic data of the South Ecuadorian subduction channel show a zone of undrained sediment conditions resulting in growing fluid overpressure with depth above a zone of rapid sediment compaction and subsequent release of overpressured fluids [42], which could account for a large pore fraction increase derived from our observations.

An estimate of the absolute pore fraction may be derived from the modelled bulk resistivity values if assumptions about the fluid resistivities are made using equation 1 (Archie's law). Assuming fluid resistivity values ranging from 0.01 Ohm m (derived by [49] for fluids at crustal temperature) to 0.3 Ohm m (resistivity of salt water) yield an approximate absolute pore fraction increase ranging from in total 2% (increase from 2% to 4% pore fraction) to 12% (increase from 9% to 21% pore fraction) within the anomaly.

Total volume of water per km trench may then be estimated by multiplying the pore fraction by the area of the anomaly. Assuming a minimum area of 50 km² for anomaly D, the amount of fluid produced through mineral dehydration amounts most likely to about 6 km³ of fluid per km of along strike trench but to at least 1 km³ fluid per km of along strike trench.

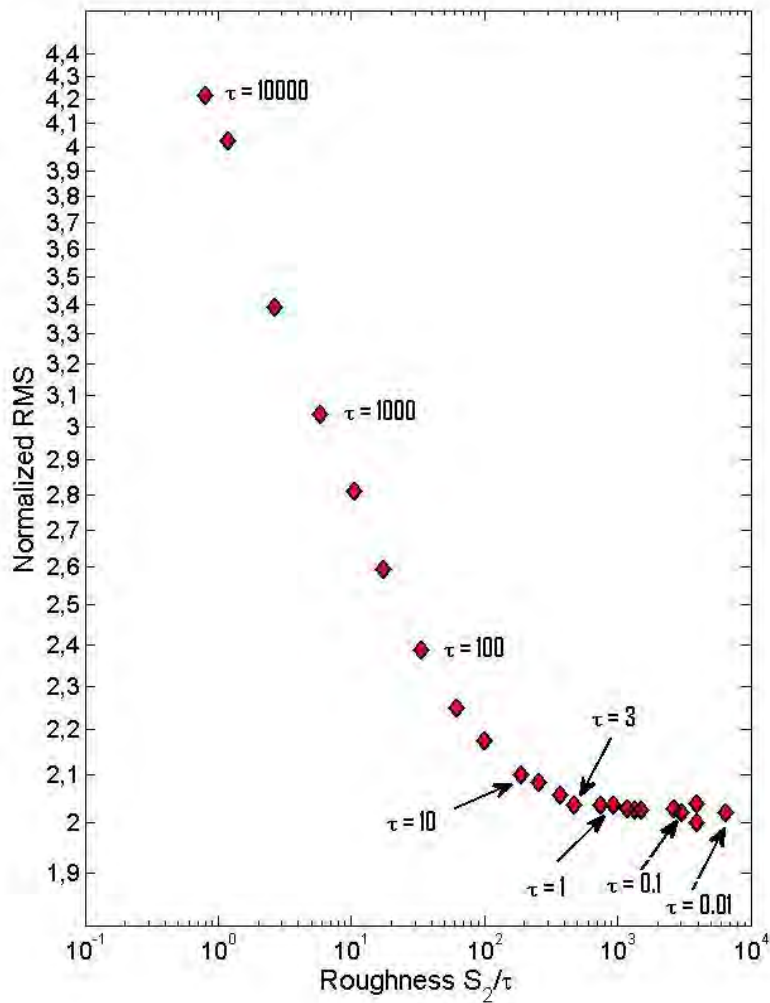
Much is known about the lithology and composition of the sediments at the Costa Rican margin based on ODP hole 170 [44] and ODP hole 205 [45] allowing for a rough estimate of the amount of mineral-bound fluids in the sediments to have entered the subduction zone. Analysis of [46] shows that on average 4% volume percent of water bound in opal and smectite is contained in the subducting sediment column. Assuming a sediment thickness of 0.5 km with 4% volume of water, a subduction rate of 88 km/Ma, we arrive at an estimate of 17.6 km³ per km trench of mineral-bound water that have entered the subduction zone within the last 10 Ma.

[16] and [23] estimate that a significant amount of fluids has been released at midslope fluid seeps. The resistivity anomaly D however suggests that approximately 6% to 34% of mineral bound water entering the subduction zone has been accumulated during this period at a depth of approx. 12 km depth at a distance of 65 km from the trench.

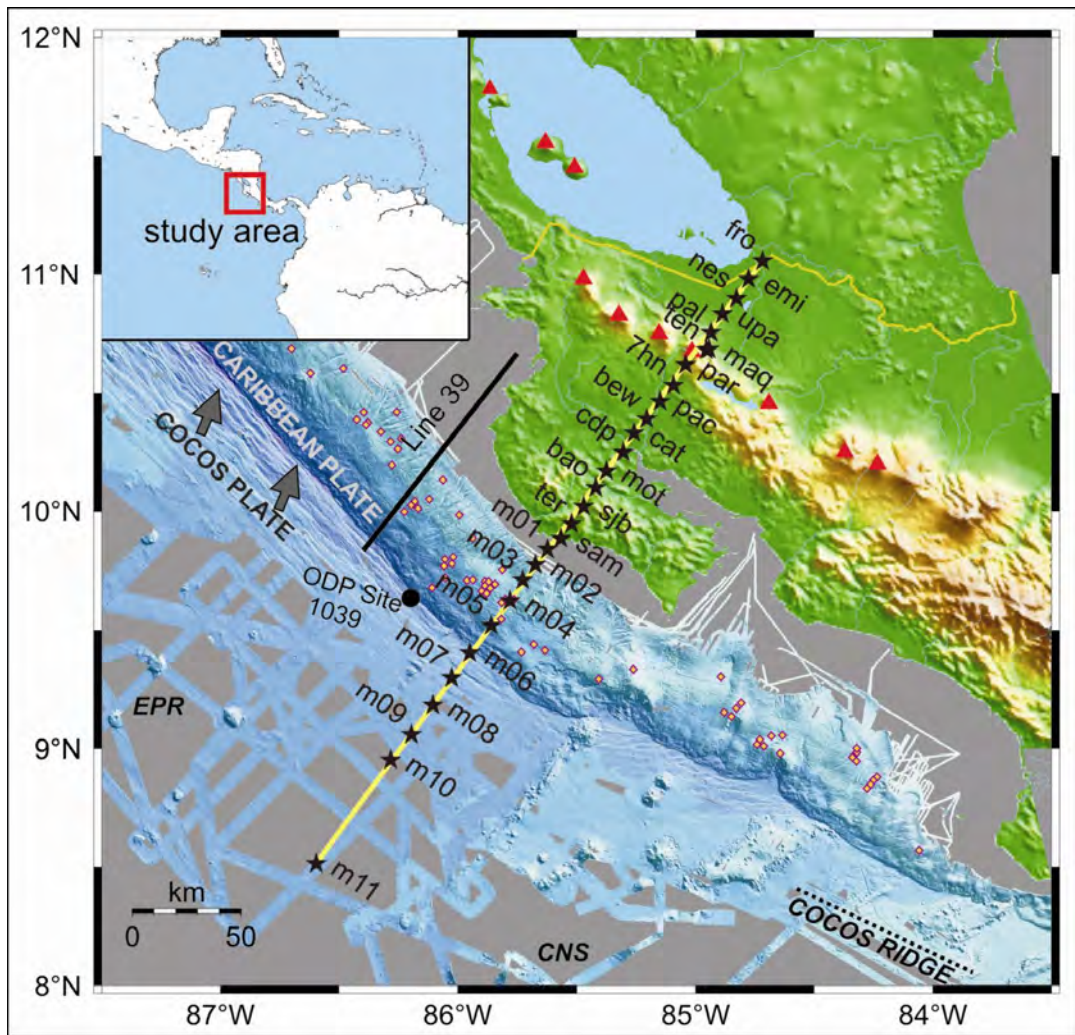
Deep crustal fluid accumulation in the forearc (resistivity anomaly G)

The most plausible explanation for the globally occurring conductivity (low resistivity) anomaly G is the existence of fluids. While Archie's Law [41] is suitable for estimation of pore fraction in sediments, a more stringent estimate of minimal fluid filled pore fraction in the crust may be derived by the lower Hashin-Shtrikman bounds [47]. This relationship between bulk resistivity, pore space fraction and resistivity of solid and fluid phase assumes that the pore space ideally connected, thus requiring the minimum pore fraction for a given resistivity. A resistivity of 15 Ohm m within anomaly G would require a fluid filled porosity of 2% to 10% percent assuming a fluid resistivity between 0.2 Ohm m and 1 Ohm m which are compatible for melt as well as crustal fluids [48]. A temperature model along this transect [49] predicts a temperature of 400° C to 500° C at this location, which is not compatible with the existence of melt, such that a water filled pore fraction is more likely. The possibility of such crustal fluid accumulation in tectonic compressional regimes has been shown by [50]. Crustal fluid accumulations at these depths have in fact been observed also in another compressive tectonic regime of Eastern Tibetan plateau through magnetotelluric data [51].

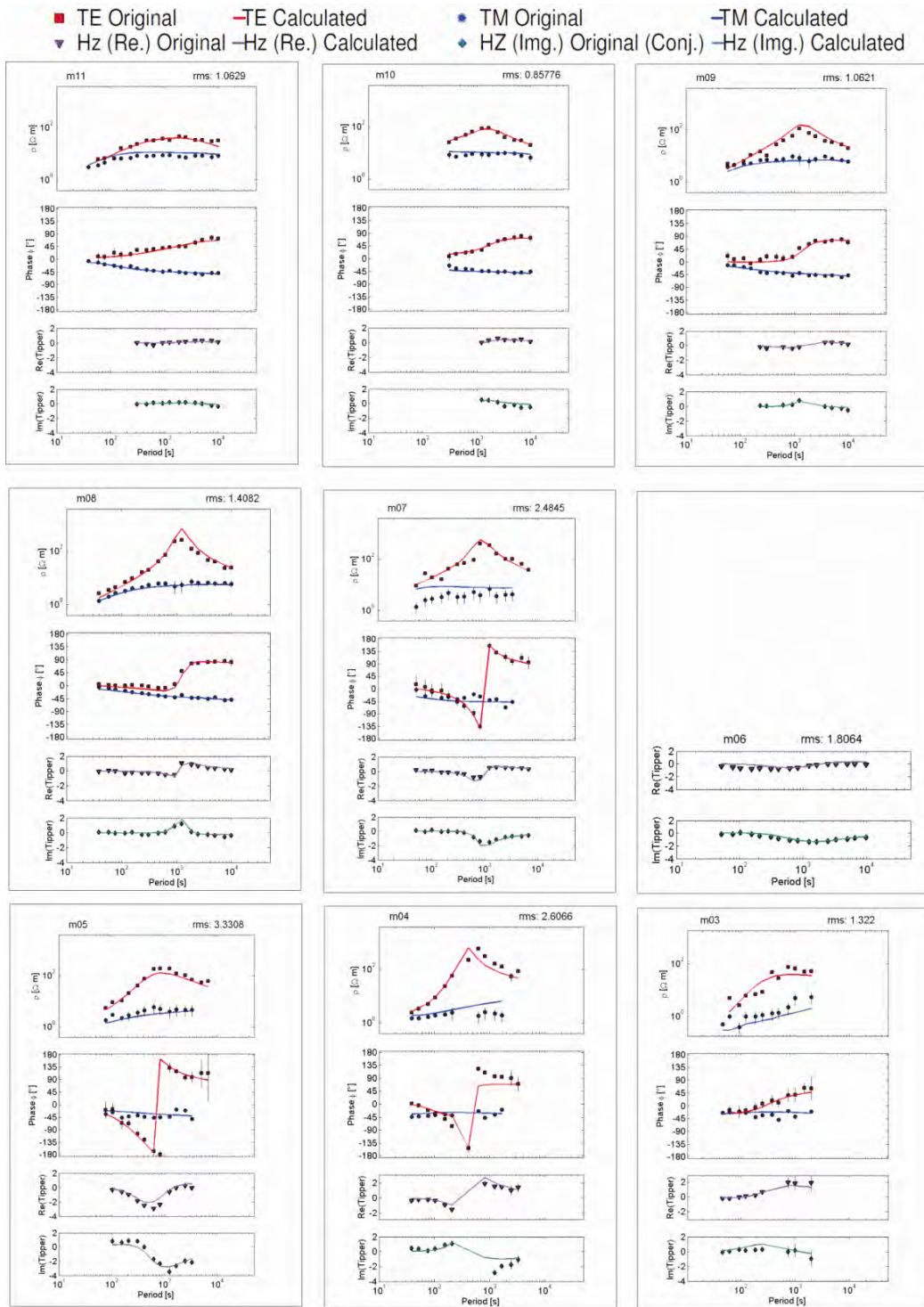
As for anomaly D, a rough estimate of the amount of fluid in G may be estimated by multiplying the pore fraction in anomaly D with its size, which we estimate to be at least 25 km², yielding a value of 0.5 to 2.5 km³ of water per km of along strike trench.



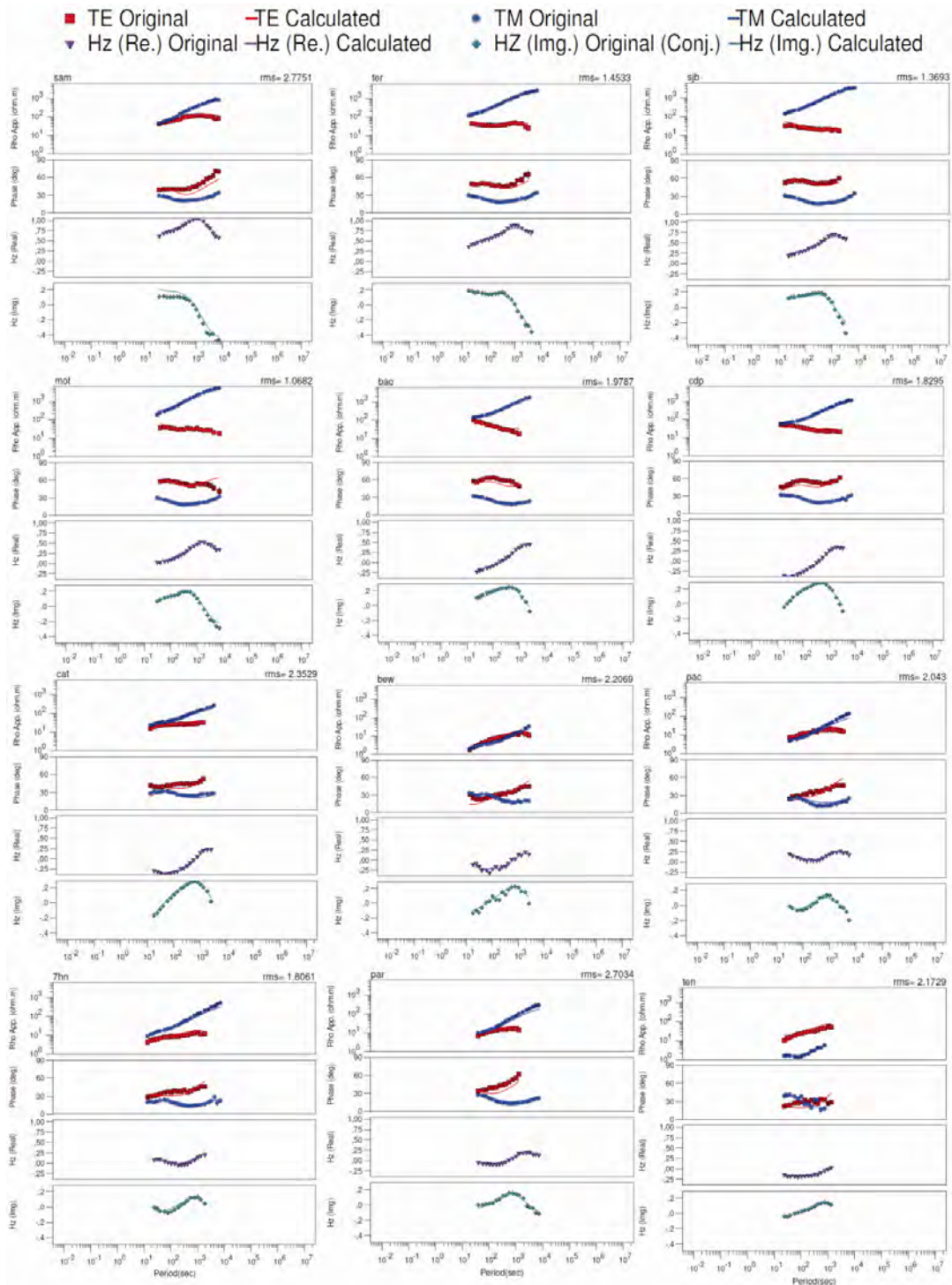
Supplementary Figure 1: L-curve derived from trade-off analysis between misfit and model roughness after 45 iterations.



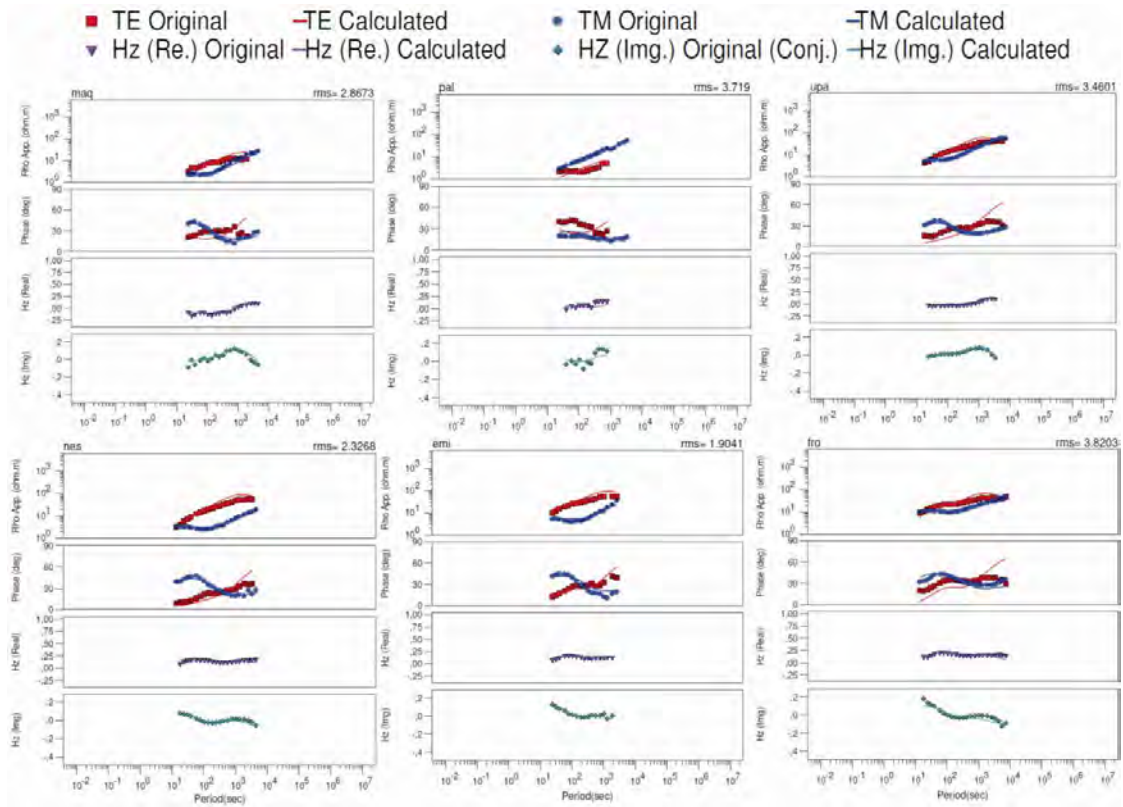
Supplementary Figure 2: Station map (like Fig.1) with station names used in other Supplementary Figures.



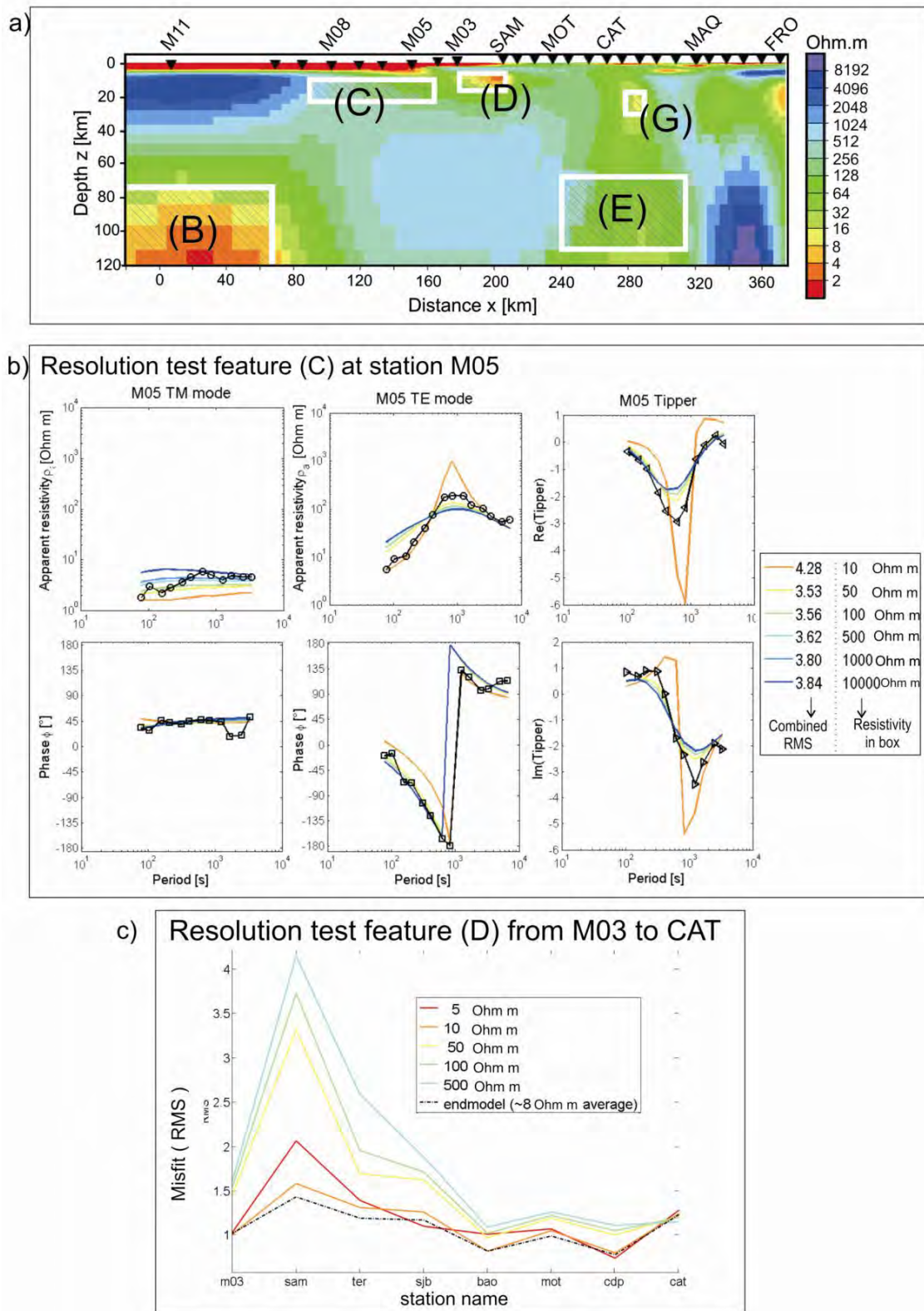
Supplementary Figure 3: Observed and modelled marine strike-rotated transfer functions for all seafloor stations.



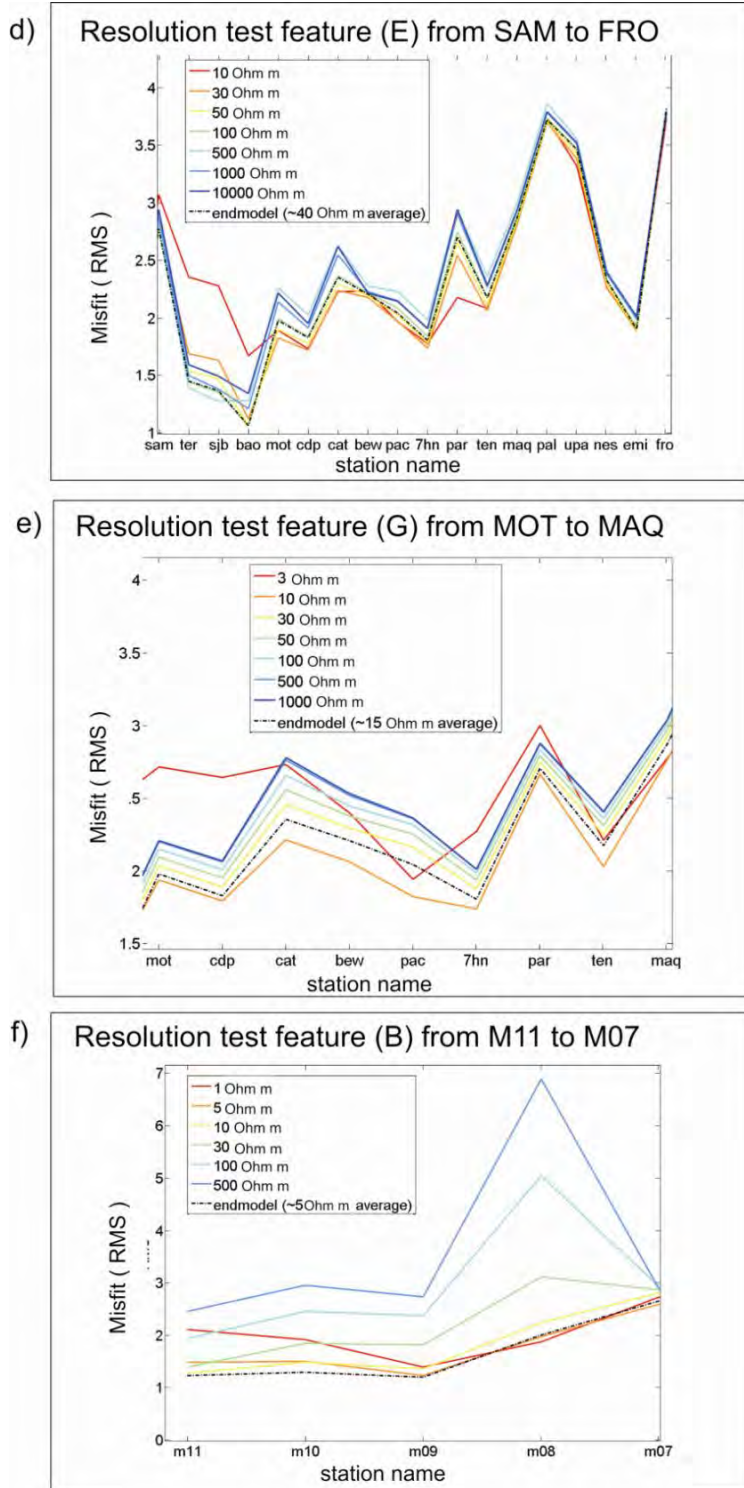
Supplementary Figure 4: Observed and modelled Strike-rotated transfer functions of land stations. Denotation same as in Supplementary Figure 3, but phases here (second panels of each station) range between 0° and 90° .



Supplementary Figure 4 Continuation



Supplementary Figure 5: Resolution tests for the most prominent conductive anomalies.



Supplementary Figure 5 Continuation.

Figure captions for Supplementary figures

Supplementary Figure 1: L-curve derived from trade-off analysis between misfit and model roughness after 45 iterations. The value $\tau = 3$ at the strongest curvature of the curve was chosen as regularization parameter.

Supplementary Figure 2: Station map (like Fig.1) with station names used in other Supplementary Figures. Orange diamonds are fluid seeps after [37]. The Cocos Plate is converging with the stable interior of the Caribbean plate at a rate of 88 km/Ma and at a 20° angle from the orthogonal direction [38]. Oceanic lithosphere subducting beneath the Nicoya Peninsula derives from both the Cocos-Nazca Spreading Center (CNS) and East Pacific Rise (EPR) [39].

Supplementary Figure 3: Observed and modelled marine strike-rotated transfer functions for all seafloor stations.

Responses are displayed by four panels, respectively, showing from top to bottom: 1.) Apparent resistivities in logarithmically spaced Ohm m (TE mode in red, TM mode in blue). 2.) Corresponding phases (-180° to 180°). 3.) Real component of tipper (purple). 4.) Imaginary component of tipper (turquoise). Markers are observed data; solid lines display predicted responses from the inversion model. Please note that for a facility of inspection TE phases were mirrored on x-axis (multiplication by -1). Station names refer to map in Supplementary Figure 2. Errors correspond to 95% confidence limits.

Supplementary Figure 4: Observed and modelled Strike-rotated transfer functions of land stations. Denotation same as in Supplementary Figure 3, but phases here (second panels of each station) range between 0° and 90° . Errors correspond to 95% confidence limits.

Supplementary Figure 5: Resolution tests for the most prominent conductive anomalies.

i) Overview of boxes that border the conductive anomalies. Resistivity of each box is varied in separate runs and the effect on the data is observed.

ii) The calculated graphs for variations of resistivity values inside box C are overlain in one plot, shown here exemplarily for station m05. Misfit of curves can also be judged by the RMS (see legend). iii) – vi) Resolution tests for anomalies D, E, G and B. Instead of displaying all curves to each station, the station's overall RMS is displayed directly (discussion see text).

Further literature for Method and Supplementary online information

[31] Chave, A. D. and Thomson, D. J., Some comments on magnetotelluric response function estimation. *J. Geophys. Res.*, 94, 14 215–14 225 (1989).

- [32] Rodi, W., and Mackie, R.L., Nonlinear conjugate gradients algorithm for 2-D magnetotelluric inversions. *Geophysics*, 66, pp. 174–187 (2001).
- [33] Constable, S., Key, K., and Lewis, L., Mapping offshore sedimentary structure using electromagnetic methods and terrain effects in marine magnetotelluric data. *Geophys. J. Int.*, 176, pp. 431–442 (2009).
- [34] Alekseev, D.A., Palshin, N.A., and Varentsov, I.M., Magnetotelluric Dispersion Relations in a Two-Dimensional Model of the Coastal Effect Physics of the Solid Earth, 2009, 45, No. 2, pp. 167–170 (2009).
- [35] Silver, E.A., Kastner, M., Fisher, A.T., Morris, J.D., McIntosh, K.D., and Saffer, D.M., Fluid flow paths in the Middle America Trench and Costa Rica margin. *Geology*, 28, pp. 679–682 (2000).
- [36] Kimura, G., Silver, E.A., Blum, P., et al., Proceedings of the Ocean Drilling Program. Initial Reports, 170, pp. 45–93 (1997).
- [37] Sahling, H., Masson, D.G., Ranero, C.R., Hühnerbach, V., Weinrebe, W., Klauke, I., Bürk, D., Brückmann, W., and Suess, E., Fluid seepage at the continental margin offshore

Costa Rica and southern Nicaragua. *Geochem. Geophys. Geosyst.*, 9, Q05S05,
doi:10.1029/2008GC001978 (2008).

[38] DeMets, C., A new estimate for present-day Cocos-Caribbean plate motion:
Implications for slip along the Central American volcanic arc. *Geophys. Res. Lett.*, 28, 21,
doi:10.1029/2001GL013518, (2001).

[39] Barckhausen, U., Ranero, C.R., von Huene, R., Cande S.C., & Roeser, H.A., Revised
tectonic boundaries in the Cocos plate off Costa Rica: Implications for the segmentation of
the convergent margin and for plate tectonic models. *J. Geophys. Res.*, 106, pp. 19 207-19
220 (2001).

[40] Wannamaker, P. E., et al., Magnetotelluric Observations Across the Juan de Fuca
Subduction System in the EMSLAB Project, *J. Geophys. Res.*, 94(B10), pp. 14 111–14 125
(1989)

[41] Archie, G.E., The electrical resistivity log as an aid in determining some reservoir
characteristics. *Petroleum Transactions of AIME* 146 pp. 54–56 (1942).

[42] Calahorrano, A.B., Sallares, V., Sage, F., Collot, J.Y., and Ranero, C.R., Nonlinear
variations of the physical properties along the Southern Ecuador subduction channel: Results

from depth-migrated seismic data. *Earth and Planetary Science Letters* 267, pp. 453-467, (2008).

[43] Keller, B.V., Rocks and mineral properties, in *Electromagnetic Methods in Applied Geophysics*. Vol. 1 (ed. M.N. Nabighian), Society of Exploration Geophysicists, pp. 13-51 (1988).

[44] Silver, E.A., Leg 170: synthesis of fluid-structural relationships of the Pacific margin of Costa Rica. In Silver, E.A., Kimura, G., and Shipley, T.H. (Eds.), *Proc. ODP, Sci. Results*, 170, pp. 1-11 (2000).

[45] Morris, J.D., and Villinger, H.W., Leg 205 synthesis: Subduction fluxes and fluid flow across the Costa Rica convergent margin. In Morris, J.D., Villinger, H.W., and Klaus, A. (Eds.), *Proc. ODP, Sci. Results*, 205: College Station TX (Ocean Drilling Program), pp. 1-55 (2006).

[46] Spinelli, G.A., and Underwood, M.B., Character of sediment entering the Costa Rica subduction zone: Implications for partitioning of water along the plate interface. *The Island Arc*, 13(3), pp. 432-451 (2004).

[47] Hashin, Z., and Shtrikman, S.: A variational approach to the theory of the effective magnetic permeability of multiphase material. *J. Appl. Phys.*, 33, pp. 3125-3131 (1962).

[48] Harris, R. N., and K. Wang, Thermal models of the Middle America Trench at the Nicoya Peninsula, Costa Rica. *Geophys. Res. Lett.*, 29(0), doi:10.1029/2002GL015406 (2002).

[49] Nesbitt, B. Electrical resistivities of crustal fluids. *J. Geophys. Res.*, 98, B3, pp. 4301-4310 (1993).

[50] Connolly, J. A. D., and Y. Y. Podladchikov, Fluid flow in compressive tectonic settings: implications for midcrustal seismic reflectors and downward fluid migration. *J. Geophys. Res.*, 109, doi:10.1029/2003JB002822 (2004).

[51] Bai, D., Unsworth, M.J., Meju, M.A., Ma, X., Teng, J. Kong, X., Sun, Yi., Sun, J., Wang, L., Jiang, C., Zhao, C., Xiao, P., Liu, M., Crustal deformation of the eastern Tibetan plateau revealed by magnetotelluric imaging. *Nature Geoscience*, 3, Issue 5, pp. 358-362 (2010).

Chapter 6

Summary - Conclusion - Outlook of thesis

This study images the water cycle in the Costa Rican subduction zone from the hydration of the subducting slab prior to entering the deep-sea trench to the dehydration of the slab at distinct depths. An amphibious magnetotelluric experiment is performed in one congruent setting, providing new insights to geologic features and also to the methodological application of marine MT at continental margins.

The marine MT data pose a particular challenge as some stations turn out to be highly disturbed by periodical noise, and must be removed by simply cutting out all noisy sections. Transfer functions are derived which, rotated to geologic strike direction, reveal unusual shapes that demand further methodological investigation. Thus, a detailed modeling study of the “coast effect” is performed, revealing that the presence of a coast produces a specific signature on the marine transfer functions. This study defines and quantifies this special signature, and derives approximations that relate physical parameters to each other (such as distance from the coast, period, ocean depth and bulk resistivity). It is shown that the most pronounced distortion due to the coast can be, quite surprisingly, helpful, because it allows the bulk resistivity to be estimated and further increases the sensitivity for detecting conductivity anomalies. The study implies that the “coast effect” may reach out over many hundreds of kilometers from the coast, and thus the presence of the coast should also be respected in the inversion of marine data which are measured far away from a continental margin.

The marine transfer functions are inverted together with the land transfer functions yielding an overall image of the hydration and dehydration cycle in a subduction zone (but not behind the volcanic arc). An electrically conductive zone in the outer

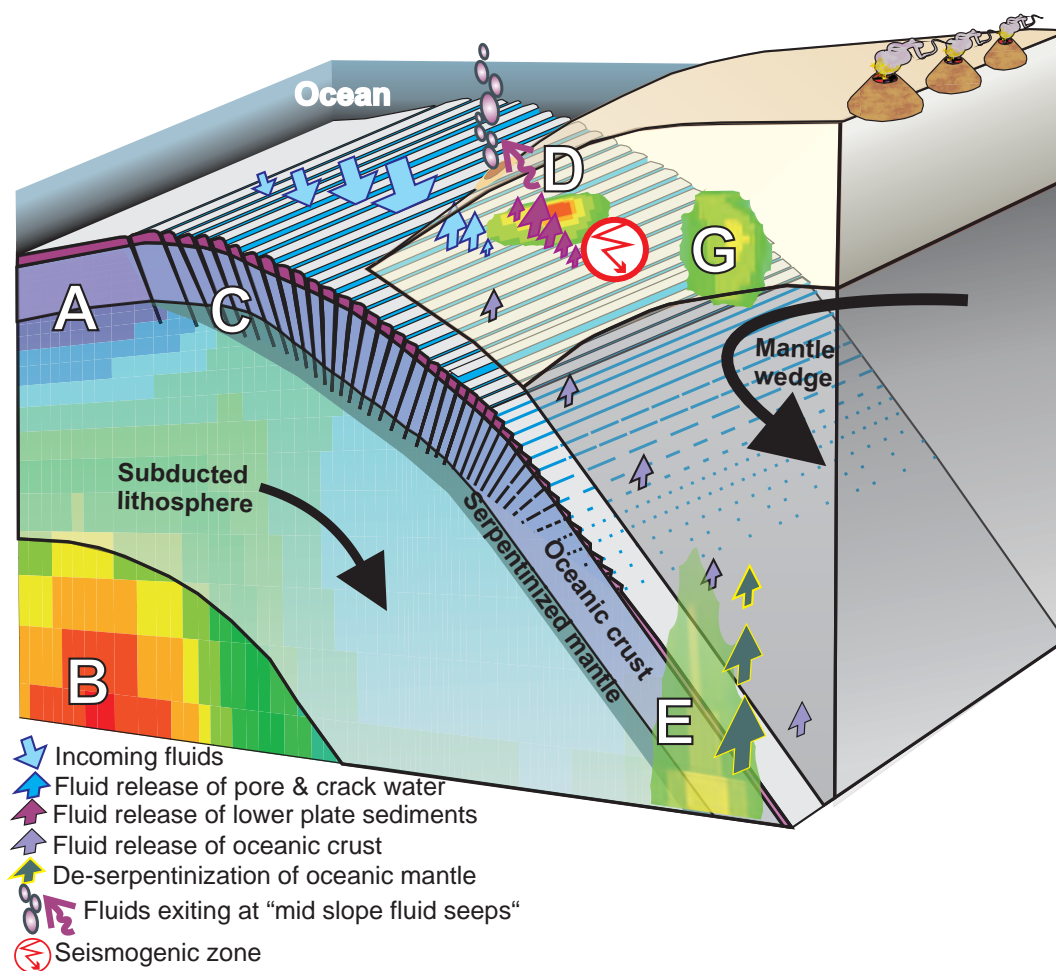


Figure 6.1: Fluid cycle in Costa Rican subduction zone

rise of the incoming plate is associated with sea water penetrating down extensional faults and cracks into the upper mantle. This is in agreement with the findings of Ranero et al. [2003]. Along the downward subducting plate, distinct conductive anomalies image fluids from dehydration of sediments, crust and mantle. This is in agreement with geochemical modeling studies by Rüpke et al. [2004]. A conductivity anomaly at a depth of approximately 12 km and at a distance of 65 km from the trench is associated with a major dehydration reaction of mineral-bound water, which correlates with the geochemically proposed source depth of fluids that exit at mid slope fluid seeps (Hensen et al. [2004]). The occurrence of the first major fluid release coincides with the updip limit of the seismogenic zone, which extends along dryer portions of the megathrust which will support seismogenesis. Another fluid accumulation is revealed by a conductivity anomaly, named G, at 20-

30 km depth and a distance of approximately 30 km seaward from the volcanic arc. Although this G-anomaly cannot be clearly attributed to either specific dehydration processes or melt processes is of particular interest: A comparison with other electromagnetic studies from subduction zones around the world reveals that such a conductivity anomaly is a global feature suggesting the presence of a global fluid sink. This sink might be a contribution to the general observed deficit between water input and output in a subduction cycle as illustrated in the introductory Fig. 1.1 -

This is where some of the water might have gone! (Fig. 6.1)

As the G-anomaly is proposed to be a global feature, its detection raises several questions, such as:

- What is its origin?
- How can fluids be maintained in the crust? and
- Is this fluid accumulation growing through time?

These open questions beg for studies of other disciplines that could contribute new ideas.

Outlook

From the electromagnetic point of view, there are 1.) geological targets, and 2.) methodological issues that need to be investigated in the future with MT methods:

1. From the geologic point of view, another particular part of the Costa Rican subduction zone should be imaged with MT:

Fluids feeding the volcanoes are found in most active subduction zones. A recent MT study on the very young subduction zone of New Zealand's South island shows several zones of enhanced conductivities, which Wannamaker et al. [2009] interpret to represent upward migrating fluids associated with dehydration processes. Neither a volcanic arc, nor a trench has developed yet in this young subduction system. As conductivity zones observed by Wannamaker et al. [2009] have smaller values in comparison to the conductive anomalies of the other mature subduction zones in the world (discussed in Chapter 5 and Appendix 7.5), one may infer that subduction in New Zealand's South island has not fed crust and upper mantle with enough water yet to activate volcanism.

The MT studies of mature subduction zones with active volcanic arcs are

discussed in this study, but what is missing is a comparison to a former subduction zone that has meanwhile stopped transporting material to the Earth's interior shutting off volcanism.

In southeastern Costa Rica, where the Cocos ridge is being thrust under the Caribbean plate, volcanism is extinct. There are controversial theories concerning the cause of extinction, and concerning the subduction of the ridge (whether as flat underplating or at steep angle as discussed in Dzierma [2008] and Section 2.1.2)). A magnetotelluric survey in that region could yield insights concerning one hypothesis stating that there might be a lack of fluids to feed the volcanoes. Further, if an anomaly was observed in southern Costa Rica that one can associate with the G-anomaly in northern Costa Rica, a direct comparison might yield insights on the role of this anomaly for volcanism and whether it is growing through time or not.

2. From the methodological point of view, further research on the marine part of the "coast effect" must be carried out. The approximations that relate physical parameters to each other still lack an analytical solution, which yet may be found. Furthermore, the approximations are derived only for the 2D- case. The next step is to perform 3D- modeling studies test the dependency of the seawater volume on distortion of transfer functions.

Last but not least, the amphibious MT results of the Nicaraguan and the Chilean subduction zones are eagerly awaited for comparison with the findings in northern Costa Rica.

Acknowledgements

I owe my deepest gratitude to my PhD-supervisor Dr. Marion Jegen-Kulcsar. *Dear Marion, you really never stopped to encourage me... Your guidance and constant support in the last five years enabled this work until its completion and provided the environment for me to scientifically “grow up”. Thanks for your endless patience, for your scientific and personal counsel, and for the homey environment you created - I really enjoyed the last couple of years working in your group. Thanks also for all the fruitful discussions we had about science, conversations about everything under the sun, and chats about “Sex and the City”.*

I am deeply grateful to my co-referee Prof. Dr. Heidrun Kopp, who also guided me to the final level. *Dear Heidrun, I am very appreciative of your generosity with your time, your enriching input, and all your advices. Your communication has become an important source of my scientific training and visions.*

There are many other people who contributed to this work, and I am grateful to all of them. In the following, they are listed in the order of appearance with respect to this study.

I would like to kindly thank Olaf Hillemaier, Ronald Kroth and Markus from Magson GmbH, who all showed great enthusiasm for the instrument development. I would like to thank them for the constructive dialog and permanent adaption of all improvement suggestions, and for the patience in explaining/repeating some electronic issues over and over... A special thanks goes to Ronald Kroth, who also joined the deployment survey - *Dear Ronald, without your inventive troubleshooting, probably not enough data would have been recorded to evaluate, so thank you for all the outstanding efforts working night and day under tough conditions!*

When one of our first developed instruments got lost during test measurements in the Baltic sea, it washed ashore the Swedish coast and was eventually recognized

by a kind Swedish geophysicist who was strolling around the beach with his Sauna club mates. Since it was vital to receive the instrument back to be used at the experiment in Costa Rica, I would like to thank him for calling us and saving the instrument de-assembled in his garage. Furthermore, thanks for the awesome trip to the giant ship of stones at Ales Stenar.

I am appreciative to the magnetic observatory in Niemegk (Adolf- Schmidt- Observatorium of GFZ Potsdam) for allowing instrument tests at their facilities, and also for kindly providing the ap-index data during the measurement period in Costa Rica.

I wish to sincerely thank Marion and Fritz Junge, lovely people who kindly allowed us to perform a few days' test measurements on their property - a magnetically undisturbed, remote and beautiful place in Schleswig Holstein, which is one of my favorite places.

I wish to express my warm and sincere thanks to my esteemed colleagues who trained and prepared me for conducting the experiment in Costa Rica, I have profited very much from their experiences (and their willingness to share them). In particular, I heartily thank Prof. Dr. Ernst Flüh for the opportunity to join the FS SONNE offshore Indonesia and for his most efficient short course into ship manners, techniques and tools. I also thank him for pleasant night watches, for adding zest to a Feierabendbier, and for his good advices.

I would like to sincerely thank Klaus-Peter Steffen and Patrick Schröder for all the technical improvements, advices and support on the ocean bottom system.

I sincerely thank Anne Krabbenhöft for taking me aside and sharing her past experiences - all her advice in planning and performing the experiment, especially on the procedure with the customs listings, turned out to be extremely important and helpful.

There were many people who contributed to the success of the experiment in Costa Rica and I am very grateful to all of them.

The planning of the experiment was facilitated very much by Ivonne Arroyo's past experiences with the customs procedures in Costa Rica, and I would like to heartily thank her for the kind help she provided by sharing her knowledge and communicating with some officials on behalf of this experiment.

During my reconnaissance trips to Costa Rica, I was very lucky to receive the kind

help of Natalia Zamora and Oskar Lücke, I am very grateful for them translating my concerns to the officials and showing me around.

I owe deep gratitude to the people from the Instituto Costarricense Electricidad (ICE) in Costa Rica - this whole experiment would not have been possible without the kind help of Prof. Guillermo Alvarado, who made all the arrangements.

I wish to express my warm and sincere thanks to Waldo Taylor from ICE, who was basically ALWAYS there to help out, troubleshoot and for maintenance. *Dear Waldo, muchas muchas gracias for your outstanding efforts to make this experiment happen - without you, it might never have happened.*

Warm thanks also go to Soto for helping to push airfreight and a container full of instruments through the local customs, which was a remarkable task- *Dear Soto, in case you ever have problems with the German customs, I shall return the favor.*

I would also like to express my gratitude to all the other guys from ICE, who so kindly supported us with their manpower - especially, thanks to Chico (also for the unforgettable Karaoke night in the Salsa-bar).

I wish to express my sincere gratitude to the German Embassy in Costa Rica, in particular to Bettina Kitzing and to Sofia Herrera. These two angels of the Embassy have helped in so many aspects, but most important they successfully communicated with the Costa Rican Secretary of Transportation, which enabled the cooperation with the Costa Rican Coast Guard.

And I would like to sincerely thank Commandante Rodrigo Peralta and the crew of the Costa Rican Coast Guard for providing us with ship time and a motivated crew to work with for the deployment cruise.

I also thank the Papagayo Seafood company for providing shiptime and a pleasant crew for the recovery cruise. I would also like to thank Anke Werner's grandparents for the donation of the original cuckoo clock, which likely contributed to opening the doors in this matter.

I am indebted to all the tough fellows who helped at the marine cruises: Ronald Kroth, Yvonne Dzierma, and Björn Lewitz, (during deployment), Marion Jegen-Kulcsar, Patrick Schröder, Claudia Jung, and Thomas Brandt (during recovery).

I would like to show my special gratitude to Yvonne Dzierma, who helped with the Spanish communication and networking, and participated in the crucial deployment survey, just to name a few of her contributions. *Dear Yvonne, during the most direful and unhealthy few days of my geophysical career on a ship that rolled*

and/or pitched from $+45^\circ$ to -45° , making me spit gall, you were literally on my side, sharing a narrow 80-cm pallet right next to the Captain. Well, thanks for not kicking me off that pallet...

I wish to heartily thank Dr. Heinrich Brasse from the FU Berlin for his support in so many aspects. *Dear Henri, thank you so much for your guidance, training and taking the time for the many discussions we had on the inversion of the data and other issues of MT. I have learned a lot from your skills, and I still am learning. I appreciate your advice and inspiration very much.*

I also wish to thank all participants of the onshore experiment that has been organized and performed by Henri.

I like to thank Prof. Dr. Alan Jones and Dr. Wolfgang Soyer for the introductory course into WinGlink which has facilitated the inversion and modeling procedure. I would like to thank Willy Weinrebe for kindly providing the bathymetric data of Costa Rica, and I also wish to thank Alexander Schmidt and Matthias Meyer for their kind help with the presentation of the bathymetric data in Fledermaus.

I sincerely thank all members of the Geodynamics Section of IFM-GEOMAR and all members of the SFB 574 for contributing to this study by profound discussions. In particular, I would like to express my gratitude to Dr. Armin Freundt and Dr. Steffen Kutterolf for their invaluable input and discussion on budget estimations, which has become an important issue of this study, and thanks also for the great Eiffel-excursion. I wish to especially thank Prof. Dr. Kaj Hoernle for his support and input, and also Dr. Heidi Wehrmann and Dr. Kiki Krüger for their input on volcanic eruptions.

I owe deep gratitude to Prof. Dr. Wolfgang Rabbel for his input and discussion. And I would also like to heartily thank Dr. Warner Brückmann for being my geoscientific Guru, broadening my horizon.

I kindly thank Prof. Dr. Martyn Unsworth and Prof. Dr. Roland von Huene for thoughtful peer-review of the manuscript which has meanwhile been published.

I sincerely thank the Nature publishing group for the permission to include the Costa Rica publication to this dissertation.

Several people have made valuable contributions to the modelling studies on the 2D-Coast Effect. First of all, I would like to acknowledge Gerhard Kapinos and Dr. Heinrich Brasse, who gave the spark to this study. During his modeling studies Gerhard encountered peaks in the apparent resistivities and drove the attention to them.

Very special thanks go to Antje Franke for providing her code for the modeling study, and for taking her time to explain it so thoroughly.

Further, I would like to especially thank Dr. Martin Thorwart, not only for all the pleasant Skat evenings with good Wetterauer Gold, but also for attentively listening to my modeling findings and thoughts on a cold January evening and bringing up the idea to search for characteristic values - *Dear Martin, you are an inspiration!*

Furthermore, I would like to thank Dr. Anna Avdeeva and Dr. Max Moorkamp for inspiring discussions and profound corrections which also contributed greatly to the Coast Effect study.

I also wish to warmly and sincerely thank all the other members of Marion's EM group for being so supportive, for making the working environment most pleasant, and for providing an encouraging, motivating atmosphere: Jin Chen, Dr. Sebastian Hölz, Dr. Björn Heincke, Romina Gehrman, Malte Sommer and Angus Rost — *Dear Anna, thank you for always taking time. Time for listening and troubleshooting, and time for drinking a decent cup of tea with me, thank you for making the time enjoyable...*

Dear Max, thank you for your consistent open ear and counsel, and the candid attempt to make a better geophysicist out of me...

Dear Sebi, thank you for your advice, helpfulness and patience. You have often saved my day, when I was planning to crush my computer, which you then debugged within only minutes...

Dear Björn H., thank you for your support and for being such a jolly good fellow...

Dear Jin, I am very lucky to have had such a fantastic co-PhD fellow like you, as you are competent in everything I adore: from geometrical 3D derivations of rotated matrices to the superb Chinese cuisine. Thanks for your help and the pleasant, delicious time...

Dear Romina, since you left for Canada, a vacuum remained. I still miss our chats, your laugh, your jokes and your green thumb to make our office plants blossom.

The soul of a group is formed by its diligent assistants, who take care also of all those formalities which tend to have an overexerting effect on many scientists. Thus I warmly thank Silke Schenck, Erna Lange and Martina Nöske for their pleasant company and constant support in making our lives easier every day. The same accounts for the kind librarian team of Angelika Finke - thank you all for providing us

so often also with rare literature. *And Dear Silke, thank you also for all the Spanish-English translations and corrections, but also for expanding my German language horizon.*

A big hug also goes to all brave proofreaders of this thesis: *Dear Gareth Crutchley, dear Andrei Swidinsky, dear Yvonne and dear Max - Thank you all so much for improving this manuscript, I owe you! Lunch?*

I wish to thank my esteemed colleagues from the ETH Zürich, and departments of Physics at Stanford, and Meteorology at FU Berlin for the exquisite time out: *Dear Lasse Rabenstein, dear Paul Zieger, dear Patrick Kirchmann, and dear Stefan Stapelberg, going to conferences is much more fun when I meet you there and we will be submerging in the outdoors.*

I wish to thank my lovely sisters Daniela and Sonja, and all my friends and jolly sports mates, especially the “Polodamen” of the KVK, for the great time I had while working on this thesis and for the vital counterbalance to the work which they always offered.

Last but not least, and most important, I wish to express my warmest gratitude to my beloved parents and my partner. I thank my parents, Wanny and Wolf, for their unconditional love and consistent support, for ever since I can think back. *Dear Mama and Daddy, I thank you for many of my personal abilities and skills that I attribute to your education, which enabled me to go through with my academic education.*

And finally I thank my partner Björn Lewitz. *My dear Björn, I surely owe you my deep gratitude for all your contributions to this study. Thanks for designing and building the test apparatus at shortest notice, and cranking the car jack back and forth for endless hours, despite the tiredness of your arms; thanks for all your hard work during the deployment survey, despite Dengue; and there is just so much more to thank. But I feel the most heartfelt gratitude to you as the person being always at my side for more than a decade, always supporting and encouraging me to hold on. Thank you for your deep love and for making me love you deeply.*

Bibliography

- D. A. Alekseev, N.A. Palshin, and Iv. M. Varentsov. Magnetotelluric Dispersion Relations in a Two-Dimensional Model of the Coastal Effect. *Physics of the Solid Earth*, 45 (2):167–170, 2009.
- S. Allerton, H. U. Worm, and L. B. Stokking. Paleomagnetic and rock magnetic properties of hole 896A. *Proc. Ocean Drill. Program Sci. Results*, 148:217–226, 1996.
- G. E. Archie. The electrical resistivity log as an aid in determining some reservoir characteristics. *Petroleum Transactions of AIME*, 146:54–56, 1942.
- K. Baba. Electrical structure in tectonic settings. *Surveys in Geophysics*, 26:701–731, 2005.
- K. Baba and A. D. Chave. Correction of seafloor magnetotelluric data for topographic effects during inversion. *Journal of Geophysical Research*, 110 (B12105): 1–16, 2005.
- K. Baba and N. Seama. A new technique for the incorporation of seafloor topography in electromagnetic modelling. *Geophysical Journal International*, 150:392–402, 2002.
- U. Barckhausen, C. R. Ranero, R. von Huene, S. C. Cande, and H. A. Roeser. Revised tectonic boundaries in the Cocos Plate off Costa Rica: Implications for the segmentation of the convergent margin and for plate tectonic models. *Journal of Geophysical Research*, 106 (NO. B9):19207–19220, 2001.
- M. N. Berdichevsky and V. I. Dimitriev. Basic principles of interpretation of magnetotelluric sounding curves. *Geoelectric and Geothermal Studies*, 1976.
- A. Berhorst. *Die Struktur des aktiven Kontinentalhangs vor Nicaragua und Costa Rica - marin-seismische Steil- und Weitwinkelmessungen*. PhD thesis, Christian-Albrechts-Universität zu Kiel, 2006.

- J. Bialas and E.R. Flüh. Ocean Bottom Seismometers. *Sea Technology*, 40 (4): 41–46, 1999.
- S. Bilek. The role of subduction erosion on seismicity. *Geology*, 38 (5):479–480, 2010. doi: 10.1130/focus052010.1.
- P. Bird. An updated digital model of plate boundaries. *Geochemistry Geophysics Geosystems*, 4:1027, 2003. doi: 10.1029/2001GC000252.
- J. R. Booker, A. Favetto, and M. C. Pomposiello. Low electrical resistivity associated with plunging of the Nazca flat slab beneath Argentina. *Nature*, 429:399–403, 2004.
- H. Brasse, P. Lezaeta, V. Rath, K. Schwalenberg, W. Soyer, and V. Haak. The Bolivian Altiplano conductivity anomaly. *Journal of Geophysical Research*, 107(B5): 10.1029/2001JB000391, 2002.
- H. Brasse, G. Kapinos, Y. Li, L. Muetschard, W. Soyer, and D.Eydam. Structural electrical anisotropy in the crust at the South-Central Chilean continental margin as inferred from geomagnetic transfer functions. *Physics of the Earth and Planetary Interiors*, 173:doi:10.1016/j.pepi.2008.10.017, 2009a.
- H. Brasse, G. Kapinos, L. Muetschard, G.E. Alvarado, T. Worzewski, and M. Jegen. Deep electrical resistivity structure of northwestern Costa Rica. *Geophysical Research Letters*, 36:doi:10.1029/2008GL036397, 2009b.
- G. V. Burbach, C. Frohlich, W. D. Pennington, and T. Matumoto. Seismicity and tectonics of the subducted Cocos Plate. *Journal of Geophysical Research*, 89: 7719–7735, 1984.
- B. Buttkus. *Spektralanalyse und Filtertheorie*. Springer-Verlag, 1991.
- J. Byerlee. Model for episodic flow of high-pressure water in fault zones before earthquakes. *Geology*, 21:303–306, 1993.
- L. Cagniard. Basic theory of the magneto-telluric method of geophysical prospecting. *Geophysics*, 18:605–635, 1953.
- T. G. Caldwell, H. M. Bibby, and C. Brown. The magnetotelluric phase tensor. *Geophysical Journal International*, 158:457–469, 2004.
- S. Carbotte and K. Macdonald. East Pacific Rise 8-10 31’N: Evolution of ridge segments and discontinuities from SeaMARC II and three-dimensional magnetic studies. *Journal of Geophysical Research*, 97:6959–6982, 1992.

- A. D. Chave and D. J. Thomson. Some comments on magnetotelluric response function estimation. *Journal of Geophysical Research*, 94 (No. B10):14215 – 14225, 1989.
- A. D. Chave and D. J. Thomson. Bounded influence magnetotelluric response function estimation. *Geophysical Journal International*, 157:988–1006, 2004.
- P. Clift and P. Vannucchi. Controls on tectonic accretion versus erosion in subduction zones: Implications for the origin and recycling of the Continental crust. *Reviews of Geophysics*, 42:1–31, 2004.
- S. Constable. Marine electromagnetic induction studies. *Surveys in Geophysics*, 11, 133–327, 1990., 11:133–327, 1990.
- S. Constable and A. Duba. The electrical conductivity of olivine, a dunite, and the mantle. *Journal of Geophysical Research*, 95:6967–6978, 1990.
- S. Constable, T. J. Shankland, and A. Duba. The electrical conductivity of an isotropic olivine mantle. *Journal of Geophysical Research*, 97:3397, 1992.
- S. Constable, K. Key, and L. Lewis. Mapping offshore sedimentary structure using electromagnetic methods and terrain effects in marine magnetotelluric data. *Geophysical Journal International*, 176:431–442, 2009.
- S. C. Constable, G. M. Hoversten, and H. F. Morrison. Marine magnetotellurics for petroleum exploration, Part II: Numerical analysis of subsalt resolution. *Geophysics*, 63 (NO. 3):826–840, 1998a.
- S. C. Constable, A. S. Orange, G. M. Hoversten, and H. F. Morrison. Marine magnetotellurics for petroleum exploration Part I: A sea-floor equipment system. *Geophysics*, 63:816–825, 1998b.
- C. S. Cox. Electromagnetic induction in the oceans and inferences on the constitution of the Earth. *Geophysical Surveys*, 4:137–156, 1980.
- C. DeMets. A new estimate for present-day Cocos-Caribbean plate motion: Implications for slip along the Central American volcanic arc. *Geophysical Research Letters*, 28:4043–4046, 2001.
- H. R. DeShon and S. Y. Schwartz. Evidence for serpentinization of the forearc mantle wedge along the Nicoya Peninsula, Costa Rica. *Geophysical Research Letters*, 31: L21611, 1–4, 2004.

- H. R. DeShon, S. Y. Schwartz, A. V. Newman, V. Gonzalez, M. Protti, L. M. Dorman, T. H. Dixon, D. E. Sampson, and E. R. Flueh. Seismogenic zone structure beneath the Nicoya Peninsula, Costa Rica, from three-dimensional local earthquake P- and S-wave tomography. *Geophysical Journal International*, 164:109–124, 2006.
- Y. Dzierma. *A Receiver Function Study of Southern Costa Rica. Indications of Steep Cocos Ridge Subduction*. PhD thesis, Christian-Albrechts-Universität zu Kiel, 2008.
- G. D. Egbert. Processing and interpretation of electromagnetic induction array data. *Surveys in Geophysics*, 23:207–249, 2002.
- G. D. Egbert. Robust multiple-station magnetotelluric data processing. *Geophysical Journal International*, 130:475–496, 1997.
- R. L. Evans, A. D. Chave, and J. R. Booker. On the Importance of Offshore Data for Magnetotelluric Studies of Ocean-Continent Subduction Systems. *Geophysical Research Letters*, 29:10.1029/2001GL013960, 2002.
- M. Faccenda, T. V. Gerya, and L. Burlini. Deep slab hydration induced by bending-related variations in tectonic pressure. *Nature Geoscience*, 2:790–793, 2009.
- I. J. Ferguson. *The Tasman Project Of Seafloor Magnetotelluric Exploration*. PhD thesis, Australian National University, 1988.
- I. J. Ferguson, F. E. M. Lilley, and J. H. Filloux. Geomagnetic induction in the Tasman Sea and electrical conductivity structure beneath the Tasman Seafloor. *Geophysical Journal International*, 102:299–312, 1990.
- G. Fisher and P. A. Schnegg. Electromagnetic response of an ocean-coast model to E-polarization induction. *Geophysical Journal of the Royal Astronomical Society*, 53:559–616, 1978.
- D. V. Fitterman and C. Yin. Effect of bird maneuver on frequency-domain helicopter EM response. *Geophysics*, 69:1203–1215, 2004.
- A. Franke, R. U. Börner, and K. Spitzer. Adaptive unstructured grid finite element simulation of two-dimensional magnetotelluric fields for arbitrary surface and seafloor topography. *Geophysical Journal International*, 171:71–86, 2007.
- D. Galanopoulos, V. Sakkas, D. Kosmatos, and E. Lagios. Geoelectric investigation of the hellenic subduction zone using long period magnetotelluric data. *Tectonophysics*, 409:73–84, 2005.

- T. D. Gamble, W. M. Goubau, and J. Clarke. Magnetotellurics with a remote magnetic reference. *Geophysics*, 44:53–68, 1979a.
- T. D. Gamble, W. M. Goubau, and J. Clarke. Error analysis for remote reference magnetotellurics. *Geophysics*, 44:959–968, 1979b.
- T. D. Gamble, W. M. Goubau, R. Miracky, and J. Clarke. Magnetotelluric regional strike. *Geophysics*, 47:932–937, 1982.
- I. Grevemeyer, N. Kaul, J. L. Diaz-Naveas, H. W. Villinger, C. R. Ranero, and C. Reichert. Heat flow and bending-related faulting at subduction trenches: Case studies offshore of Nicaragua and Central Chile. *Earth and Planetary Science Letters*, 236:238–248, 2005.
- I. Grevemeyer, C. R. Ranero, E. Flüh, D. Kläschen, and J. Bialas. Passive and active seismological study of bending-related faulting and mantle serpentinization at the Middle America trench. *Earth and Planetary Science Letters*, 258:528–542, 2007.
- B. R. Hacker, S. M. Peacock, G. A. Abers, and D. Holloway St. Subduction factory 2. Are intermediate-depth earthquakes in subducting slabs linked to metamorphic dehydration reactions? *Journal of Geophysical Research*, 108:1–11, 2003.
- Z. Hashin and S. Shtrikman. A variational approach to the theory of the effective magnetic permeability of multiphase material. *Journal of Applied Physics*, 33:3125–3131, 1962.
- G. Heinson and S. Constable. The electrical conductivity of the oceanic upper mantle. *Geophysical Journal International*, 110:159–179, 1992.
- G. Heinson and F. E. M. Lilley. An application of thin-sheet electromagnetic modelling to the Tasman Sea. *Physics of the Earth and Planetary Interiors*, 81:231–252, 1993.
- W. Heise, H. M. Bibby, T. G. Caldwell, S. C. Bannister, Y. Ogawa, S. Takakura, and T. Uchida. Melt distribution beneath a young continental rift: the Taupo Volcanic Zone, New Zealand. *Geophysical Research Letters*, 34:L14313, 2007.
- C. Hensen, K. Wallmann, M. Schmidt, C. R. Ranero, and E. Suess. Fluid expulsion related to mud extrusion off Costa Rica - A window to the subducting slab. *Geology*, 32 (No.3):201–204, 2004.
- A. Hoffmann-Rothe, O. Ritter, and V. Haak. Magnetotelluric and geomagnetic modelling reveals zones of very high electrical conductivity in the upper crust of Central Java. *Physics of the Earth and Planetary Interiors*, 124:131–151, 2001.

- G. M. Hoversten, H. F. Morrison, and S. C. Constable. Marine magnetotellurics for petroleum exploration, Part II: Numerical analysis of subsalt resolution. *Geophysics*, 63:826–840, 1998.
- S. Husen, R. Quintero, E. Kissling, and B. Hacker. Subduction-zone structure and magmatic processes beneath Costa Rica constrained by local earthquake tomography and petrological modelling. *Geophysical Journal International*, 155:11–32, 2003.
- M. Ichiki, N. Sumitomo, and T. Kagiya. Resistivity structure of high -angle subduction zone in the southern Kyushu district, southwestern Japan. *Earth, Planets and Space*, 52:539–548, 2000.
- M. R. Ingham and R. Reeves. Magnetotelluric soundings and structure of the Tokaanu geothermal-field, New-Zealand. *J. Geomagn. Geoelectr.*, 45:729–740, 1993.
- M. Ivandic. *Impact of bending related faulting on the seismic properties of the incoming oceanic lithosphere offshore of Nicaragua*. PhD thesis, Christian-Albrechts-Universität zu Kiel, 2008.
- M. Ivandic, I. Grevemeyer, A. Berhorst, E. R. Flüh, and K. McIntosh. Impact of bending related faulting on the seismic properties of the incoming oceanic plate offshore of Nicaragua. 113:B05410, 1–13, 2008.
- R. D. Jarrard. Subduction fluxes of water, carbon dioxide, chlorine, and potassium. *Geochemistry Geophysics Geosystems*, 4, 2003. doi: doi:10.1029/2002GC000392.
- G. R. Jiracek, J.H. Curtis, J. Ramirez, M. Martinez, and J. Romo. Two-dimensional magnetotelluric inversion of the EMSLAB Lincoln line. *Journal of Geophysical Research*, 94:4145–4152, 1989.
- G. R. Jiracek, V. M. Gonzalez, T. G. Caldwell, P. E. Wannamaker, and D. Kilb. Seismogenic, Electrically Conductive, and Fluid Zones at Continental Plate Boundaries in New Zealand, Himalaya, and California-USA. *Geophysical Monograph Series 175*, pages 1–22, 2007. doi: 10.1029/175GM18.
- H. Joedicke, A. Jording, L. Ferrari, J. Arzate, K. Mezger, and L. Rüpke. Fluid release from the subducted cocos plate and partial melting of the crust deduced from magnetotelluric studies in southern Mexico: Implications for the generation of volcanism and subduction dynamics. *Journal of Geophysical Research*, 111: B08102, 2007. doi: doi:10.1029/2005JB003739.
- A. G. Jones. Imaging the continental upper mantle using electromagnetic methods. 48:57–80, 1999.

- A. G. Jones and J. A. Craven. Area selection for diamond exploration using deep-probing electromagnetic surveying. *Lithos*, 77:765–782, 2004.
- A.G. Jones, A.D. Chave, G. Egbert, D. Auld, and K. Bahr. A comparison of techniques for magnetotelluric response function estimation. *Journal of Geophysical Research*, 94:14201–14213, 1989.
- A. Kelbert, A. Schultz, and G. Egbert. Global electromagnetic induction constraints on transition-zone water content variations. *Nature*, 460:1003–1006, 2009. doi: 10.1038/nature08257.
- R. Kellet, F.E.M. Lilley, and A. White. A two-dimensional interpretation of the geomagnetic coast effect of southeast Australia, observed on land and seafloor. *Tectonophysics*, 192:367–382, 1991.
- L. K. Law. Marine Electromagnetic Research. *Geophysical Surveys*, 6:1–213, 1983.
- M. Lefeldt. *Bending-Related Faulting and Mantle Serpentinization at the Nicaraguan Subduction Zone*. PhD thesis, Christian-Albrechts-Universität zu Kiel, 2008.
- P. F. Lezaeta, A. D. Chave, and R. L. Evans. Correction of shallow-water electromagnetic data for noise induced by instrument motion. *Geophysics*, 70 (No.5): G127–G133, 2005.
- F. E. M. Lilley, J. H. Filloux, I. J. Ferguson, N. L. Bindoff, and P. J. Mulhearn. The Tasman project of Seafloor Magnetotelluric Exploration: experiment and observations. *Physics of the Earth and Planetary Interiors*, 53:405–421, 1989.
- P. Lonsdale. Structural pattern of the Galapagos microplate and evolution of the Galapagos triple junction. *Journal of Geophysical Research*, 93:13551–13574, 1998.
- J. A. Madsen, D. J. Fornari, M. H. Edwards, D. G. Gallo, and M. R. Perfit. Kinematic framework of the Cocos-Pacific plate boundary from 13N to the Orozco transform fault: Results from an extensive magnetic and SeaMARC II survey. *Journal of Geophysical Research*, 97:7011–7024, 1992.
- F. A. Monteiro Santos, A. Dupis, A. R. Andrade Afonso, and L. A. Mendes-Victor. Magnetotelluric observations over the Chaves geothermal field (NE Portugal) - preliminary results. *Physics of the Earth and Planetary Interiors*, 91:203–211, 1995.
- J. D. Morris and H. V. Villinger. Leg 205 synthesis: Subduction fluxes and fluid flow across the Costa Rica convergent margin. *Proc. ODP, Sci. Results*, 205:1–55, 2006.

- C. Mével. Serpentinization of abyssal peridotites at mid-ocean ridges. *Comptes Rendus Geosciences*, 335:82–852, 2003.
- J. Nolasco, P. Tarits, J. H. Filloux, and A. D. Chave. Magnetotelluric imaging of the Society Islands hotspot. *Journal of Geophysical Research*, 103:30, 287 – 30, 309, 1998.
- A. Nur and Z. Ben-Avraham. Volcanic gaps due to oblique consumption of aseismic ridges. *Tectonophysics*, 99:355–362, 1983.
- Y. Ogawa, M. Mishina, T. Goto, H. Satoh, N. Oshiman, T. Kasaya, Y. Takahashi, T. Nishitani, S. Sakanaka, M. Uyeshima, Y. Takahashi, Y. Honkura, and M. Matushima. Magnetotelluric imaging of fluids in intraplate earthquake zones, NE Japan back arc. *Geophysical Research Letters*, 28:3741–3744, 2001.
- E. Ohtani, K. Litasov, T. Hosoya, T. Kubo, and T. Kondo. Water transport into the deep mantle and formation of a hydrous transition zone. *Physics of the Earth and Planetary Interiors*, 143-144:255–269, 2004.
- D. Oldenburg. Geophysical Inversion for Mineral Exploration. *Geophysical Inversion Facility*, pages 1–53, 2002.
- G. J. Palacky. Resistivity Characteristics of Geologic Targets. In MN Nabighian, editor, *Electromagnetic Methods in Applied Geophysics (Vol. 1)*, pages 53–129. SEG, Tulsa, 1987.
- N. A. Palshin. Oceanic electromagnetic studies: A review. *Surveys in Geophysics*, 17:455–491, 1996.
- W. Panero, L. R. Benedetti, and R. Jeanloz. Transport of water into the lower mantle: Role of Stishovite. 108 (B1):2039, 2003. doi: doi:10.1029/2002JB002053.
- S. M. Peacock. Fluid processes in subduction zones. *Science*, 248:329–337, 1990.
- S. M. Peacock, P. E. van Keken, St. D. Holloway, B. R. Hacker, G. A. Abers, and R. L. Fergason. Thermal structure of the Costa Rica - Nicaragua subduction zone. *Physics of the Earth and Planetary Interiors*, 149:187–200, 2005.
- L. B. Pedersen, M. Bastani, and L. Dynesius. Groundwater exploration using combined controlled-source and radiomagnetotelluric techniques. *Geophysics*, 70:G8–G15, 2005.
- R. H. Pilger. Plate reconstructions, aseismic ridges, and low-angle subduction beneath the Andes. *Geol. Soc. Am. Bull.*, 92:448–456, 1981.

- M. Protti, F. Gündel, and K. McNally. The geometry of the Wadati-Benioff zone under southern Central America and its tectonic significance: results from a high-resolution local seismographic network. *Physics of the Earth and Planetary Interiors*, 84:271–287, 1994.
- M. Protti, F. Gündel, and K. McNally. Correlation between the age of the subducting Cocos plate and the geometry of the Wadati- Benioff zone under Nicaragua and Costa Rica. in *Mann, P., ed., Geologic and tectonic development of the Caribbean plate boundary: Geological Society of America Special Paper*, 295:309–329, 1995.
- C. R. Ranero, J. P. M., K. McIntosh, and C. Reichert. Bending-related faulting and mantle serpentinization at the middle america trench. *Nature*, 425:367–373, 2003.
- R. P. Ranganayaki and T.R. Madden. Generalized thin sheet analysis in magnetotellurics: an extension of Price’s analysis. *Geophysical Journal of the Royal Astronomical Society*, 60:445–457, 1984.
- O. Ritter, A. Junge, and G. J. K. Dawes. New equipment and processing for magnetotelluric remote reference observations. *Geophysical Journal International*, 132: 535–548, 1998.
- A. Robock. Volcanic eruptions and climate. *Rev. Geophys.*, 38 (2):191–219, 2000. doi: 10.1029/1998RG000054.
- A. Robock and J. Mao. Winter warming from large volcanic eruptions. *Geophysical Research Letters*, 19:2405–2408, 1992.
- W. Rodi and R. L. Mackie. Nonlinear conjugate gradients algorithm for 2-D magnetotelluric inversion. *Geophysics*, 66:174–187, 2001.
- L. H. Rüpke, J. P. Morgan, M. Hort, and J. A. D. Connolly. Are the regional variations in central american arc lavas due to differing basaltic versus peridotitic slab sources of fluids? *Geology*, 30 (NO. 11):1035–1038, 2002.
- L. H. Rüpke, J. P. Morgan, M. Hort, and J. A. D. Connolly. Serpentine and the subduction zone water cycle. *Earth and Planetary Science Letters*, 223:17–34, 2004.
- S. Sadofsky, M. Portnyagin, K. Hoernle, and P. van den Bogaard. Subduction cycling of volatiles and trace elements through the Central American volcanic arc: evidence from melt inclusions Contributions To Mineralogy and Petrology. *Petrology*, 155 (4):433–456, 2008.

- H. Sahling, D. G. Masson, C. R. Ranero, V. Hühnerbach, R. W. Weinrebe, I. Klaucke, D. Bürk, W. Brückmann, and E. Suess. Fluid seepage at the continental margin offshore Costa Rica and southern Nicaragua. *Geochemistry Geophysics Geosystems*, 9 (5):1525–2027, 2008.
- V. Sallarés, J. J. Danobeitia, and E. R. Flüh. Lithospheric structure of the Costa Rican Isthmus: Effects of subduction zone magmatism on an oceanic plateau. *Journal of Geophysical Research*, 106:621–643, 2001.
- M. W. Schmidt and S. Poli. Experimentally based water budgets for dehydrating slabs and consequences for arc magma generation. *Earth and Planetary Science Letters*, 163:361–379, 1998.
- K. Schwalenberg and R. N. Edwards. The effect of seafloor topography on magnetotelluric fields: an analytical formulation confirmed with numerical results. *Geophysical Journal International*, 159:607–621, 2004.
- K. Schwalenberg, V. Rath, and V. Haak. Sensitivity studies applied to a two-dimensional resistivity model from the Central Andes. *Geophysical Journal International*, 150:673–686, 2002.
- H. Shimakawa and Y. Honkura. Electrical conductivity structure beneath the Ryukyu trench-arc system and its relation to the subduction of the Philippine sea plate. *Journal of Geomagnetism and Geoelectricity*, 43:1–20, 1991.
- E. A. Silver, G. Kimura, and T. H. Shipley. Leg 170: synthesis of fluid-structural relationships of the Pacific margin of Costa Rica. *Proc. ODP, Sci. Results*, 170: 1–11, 2000.
- F. Simpson and K. Bahr. *Practical Magnetotellurics*. Cambridge University Press, 2005.
- W. H. F. Smith and D. T. Sandwell. Global seafloor topography from satellite altimetry and ship depth soundings. *Science*, 277:1957–1962, 1997.
- A. V. Sobolev and M. Chaussidon. H₂O concentrations in primary melts from supra-subduction zones and mid-ocean ridges: implications for H₂O storage and recycling in the mantle. *Earth and Planetary Science Letters*, 137:45–55, 1996.
- W. Soyer and M. Unsworth. Deep electrical structure of the northern cascadia (british columbia, canada) subduction zone: Implications for the distribution of fluids. *Geology*, 34:53–56, 2006.
- R. S. J. Sparks. The dynamics of bubble formation and growth in magmas: a review and analysis. *J. Volcanol. Geotherm.*, 3:1–37, 1978.

- A. N. Tikhonov. On the determination of electric characteristics of deep layers of the Earth's crust. *Dokl. Akad. Nauk SSSR*, 73:295–297, 1950.
- A. N. Tikhonov. On the mathematical basis of electromagnetic sounding theory. *Comput. Math. Phys.*, 5:545–548, 1965.
- A. N. Tikhonov and V. Y. Arsenin. *Methods for Solving Ill-Posed Problems*. Nauka, Moscow, 1979.
- V. Tuncer, M. J. Unsworth, W. Siripunvaraporn, and J. A. Craven. Exploration for unconformity-type uranium deposits with audiomagnetotelluric data: A case study from the McArthur River mine, Saskatchewan, Canada. *Geophysics*, 71: B201–B209, 2006.
- P. R. Vogt. Subduction and Aseismic Ridges. *Nature*, 241:189–191, 1973.
- K. Vozoff. The magnetotelluric method. In M. N. Nabighian, editor, *Electromagnetic methods in applied geophysics*, pages 641–711. Soc. Expl. Geophys., 02 edition, 1991.
- K. Vozoff. The magnetotelluric method in the exploration of sedimentary basins. *Geophysics*, 37:98–141, 1972.
- C. Walther and E. Flueh. Remnant of the ancient Farallon Plate breakup: A low-velocity body in the lower oceanic crust off Nicoya Peninsula, Costa Rica - evidence from wide-angle seismics. *Geophysical Research Letters*, 29:45–1 – 45–4, 2002.
- P. E. Wannamaker, J. R. Booker, A. G. Jones, A. D. Chave, J. H. Filloux, H. S. Waff, and L. K. Law. Resistivity cross-section through the Juan de Fuca subduction system and its tectonic implications. *Journal of Geophysical Research*, 94:14,127–14,144, 1989.
- P. E. Wannamaker, G. R. Jiracek, J. A. Stodt, T. G. Caldwell, V. M. Gonzalez, J. D. McKnight, and A. D. Porter. Fluid generation and pathways beneath an active compressional orogen, the New Zealand Southern Alps, inferred from magnetotelluric data. *Journal of Geophysical Research*, 107:6–1 – 6–20, 2002.
- P. E. Wannamaker, T. G. Caldwell, G. R. Jiracek, G. J. Hill V. Maris, Y. Ogawa, H. M. Bibby, S. L. Bennie, and W. Heise. Fluid and deformation regime of an advancing subduction system at Marlborough, New Zealand. *Nature*, 460:733–736, 2009. doi: doi:10.1038/nature08204.

- J. T. Weaver and F. E. M. Lilley A. K. Agarwal. The relationship between the magnetotelluric tensor invariants and the phase tensor of Caldwell, Bibby and Brown. *Exploration Geophysics*, 37:261–267, 2006.
- W. Wei, M. Unsworth, A. Jones, J. Booker, H. Tan, D. Nelson, L. Chen, S. Li, K. Solon, P. Bedrosian, S. Jin, M. Deng, J. Ledo, D. Kay, and B. Roberts. Detection of Widespread Fluids in the Tibetan Crust by Magnetotelluric Studies. *Science*, 292(doi: 10.1126/science.1010580):716–719, 2001.
- P. Weidelt. The inverse problem of geomagnetic induction. *Zeitschrift für Geophysik*, 38:257–289, 1972.
- D. C. Wilson. Fastest known spreading on the Miocene Cocos-Pacific Plate boundary. *Geophysical Research Letters*, 23:3003–3006, 1996.
- L. Wilson. Explosive volcanic eruptions - III. Plinian eruption columns. *Geophysical Journal of the Royal Astronomical Society*, 45:543–556, 1976.
- T. Worzewski. Untersuchung der Dimensionalität von magnetotellurischen Daten: Mohrkreise und Rotationsinvarianten. Master's thesis, FU Berlin, Institut für geologische Wissenschaften, Fachrichtung Geophysik, 2005.
- T. Worzewski and M. Jegen. Approximations for the 2D-Coast Effect on Marine Magnetotelluric Data. *in review at Geophysical Journal International*.
- T. Worzewski, M. Jegen, H. Kopp, H. Brasse, and W. Taylor. Magnetotelluric Image of the Fluid Cycle in the Costa Rican Subduction Zone. *Nature Geoscience*, 4 (2): 108–111, 2011. doi: 10.1038/ngeo1041.

Chapter 7

Appendix

7.1 Technical data of the first-generation OBMT instrument

Magnetic field

sensor type: 3-component fluxgate, vector compensated
 Feedback coil system: Self-supported sensor construction
 expansion coefficient: 24 ppm/ $^{\circ}C$
 dimensions: height 4 cm, diameter: 5 cm
 Sensor weight: 50 g
 orientation: orthogonal (X,Y,Z)
 Measurement ranges:

- full range mode: 60.000 nT/DNL : 350 pT
- variometer mode: 2.000 nT/DNL : 20 pT

resolution: 10 pT
 noise: <10 pT/Hz at 1Hz
 long term stability: <10 nT/year
 linearity: <0.002
 offset drift <1 nT/ $^{\circ}C$ in Earth field <0.05 nT/ $^{\circ}C$ in reduced field

Electric field

ranges: ± 1.25 V Gain 1 & ± 20 mV Gain 64
 ADC: 24 Bit with programmable Gain
 noise: < 10 nV/ at 1Hz
 (short circuit without electrodes)

Tilt

range: ± 20 degrees
 accuracy: $\pm 0.01^{\circ}$; (at $\pm 10^{\circ}$: $\pm 0.06^{\circ}$)
 liquid settling time: 0.5 s at 20C, longer settling time for increasing temperature

Temperature

range / resolution: $-50^{\circ}C$ to $+100^{\circ}C$ / $0.1^{\circ}C$

Real Time Clock

Dallas RTC:
 power consumption
 50 μW
 accuracy: 2 ppm

Seascan based module:

power consumption

accuracy: (optional / under development)

25 mW

0.1 ppm

Data Logger

mass storage: Compact flash up to 8 GByte

storage frequency: 10, 5, 1 and 0.1 Hz

interface: RS232, 38.400Baud, ASCII

7.2 Table 1

<i>Ocean depth</i>	<i>Resistivity</i> →	Rho 50 Ohm m	Rho 100 Ohm m	Rho 200 Ohm m	Rho 300 Ohm m	Rho 500 Ohm m	Rho 1000 Ohm m
100m		(<2km,<1s) ---	3km 1.7 s	5 km 3 s	9 km 5 s	15 km 10 s	27 km 17 s
1 km		15 km 100 s	29 km 199 s	70 km 501 s	100 km 630 s	150 km 1122 s	300 km 1995 s
2 km		20 km 281 s	60 km 891 s	110 km 1412 s	180 km 2511 s	290 km 3981 s	590 km 8912 s
3 km		40 km 1000 s	90 km 1584 s	180 km 3981 s	260 km 5011 s	420 km 8912 s	890 km 22387 s
4 km		60 km 1584 s	110 km 2818 s	230 km 6309 s	330 km 8912 s	560 km 15848 s	1320 km 44668 s
6 km		90 km 3162 s	180 km 7943 s	330 km 12589 s	520 km 22387 s	890 km 44668 s	>100000 s
8 km		110 km 5011 s	230 km 12115 s	440 km 25118 s	680 km 39810s	1310 km 89125 s	>100000 s

Table 1 provides a summary of the observations concerning occurrence of the “maximum effect” for various settings of ocean depth and resistivity background. Location at which maximum effect in TE apparent resistivity is observed is given by L and T_{me} . All models were calculated with a vertical coast (to be comparable) with stations spaced equidistantly every 10 km - exception: from coast to 30km offshore, grid of shallow ocean (depth of 100 m and 1 km) was refined with denser station spacing every 1.5-3 km to increase the accuracy for the observation of the maximum effect. Forward models are calculated from 1s to 100,000s with 20 frequencies per decade.

For a setting with low background resistivity (50 Ohm m) and very shallow ocean (100 m), the effect cannot be observed in this discretization (effect must lie within first two km from the coast at a periods shorter than a second). A station at the seafloor of a deep ocean (>6 km) with a high resistivity background (1000 Ωm), the effect is not observable within the considered period range (>100,000 s).

Please note that the periods have odd numbers as they arise from a logarithmically equidistant graduation of the frequency band:

10; 11.220; 12.589; 14.125; 15.848; 17.782; 19.952; 22.387; 25.118; 28.183; 31.622; 35.481; 39.810; 44.668; 50.118; 56.234; 63.095; 70.794; 79.432; 89.125; $100 \cdot 10^n$ where $n \in 1, 2, 3, 4$.

7.3 Comments on resolution test

There is no default proceeding for resolution tests in MT (such as “checkerboard tests” in seismics). Consequently, resolution tests are subject to personal bias and thus are not always included or required in scientific publications. However, the resolution tests presented in the Supplementary information of Chapter 5 have been questioned, because rectangular boxes were used. Since rectangular blocks have inherent sharp boundary contrasts, this might result in E-field discontinuities in the TM mode apparent resistivity. It can be easily tested whether the choice of rectangular boxes affects the conclusions derived from the RMS-presentation in Chapter 5 by performing a smoothed anomaly resolution test to the shallowest anomaly (D), where a difference of a smoothed and non-smoothed anomaly resolution test would be most pronounced.

The test is performed as follows:

The resistivity of the anomaly D in the final model is smoothly varied. The different smoothed resistivity models are explicitly depicted. In separate graphs we overlay the responses for these different models onto the data from stations, which are sensitive to the anomaly and list the RMS of the station data (TE, TM mode and Tipper) for the different models.

Fig. 7.1 shows a model with various smooth changes in the resistivity of the anomaly D, Figs. 7.2 - 7.5 the associated responses. The fit systematically decreases if the resistivity of the anomaly is reduced or increased, confirming that the anomaly is well resolved, this is discussed in more detail in the following.

For station locations compare Fig. 3.1 in Chapter 3. The responses for anomaly D at stations “sam” (7.2) to “mot” (7.6), are arranged as follows: Black markers are observed data (for errors, see data curves in Supplementary material of Chapter 5). The area as indicated by the arrow in Figure 7.1 was edited in six different runs to get different resistivity values (1; 5; 10; 30; 100 and 500 Ωm). Calculated Responses for each of the six models are given in different colors. Fit of inversion model is shown in black.

Responses of station sam (7.2) show that increasing resistivities above 5 Ωm (colors from yellow to blue) produces a greater misfit to the observed data. This is qualitatively observable in the misfit of curves but also in the corresponding RMS. Increasing resistivities above Ωm (as well as the underestimation of resistivity by only 1 Ohm m) both produce an increasing RMS corresponding to the observable misfit of data (see legend). Resolution tests for anomaly D at station “ter”, “sjb” and “bao” (Figs. 7.3, 7.4, 7.5) infer equivalent conclusions. Yet for station “bao”,

the lowest RMS is reached for an edited resistivity of $10 \Omega m$. Obviously, varying the resistivities doesn't affect the responses at this station which owes to the fact that one is leaving the sphere of influence of anomaly D. At Station "mot" (7.6), it hardly makes any difference, whether the area around anomaly D is $5-30 \Omega m$. Only very high resistivities (above $100 \Omega m$) or a very high conductivity ($1 \Omega m$) have a small but observable effect on "misfitting" the data.

This test was run to erase concerns about using vertical boxes instead of smoothed out regions. Since it is valid for the shallowest anomaly at 12 km depth, it is also valid for the all other boxes that are placed at greater depths.

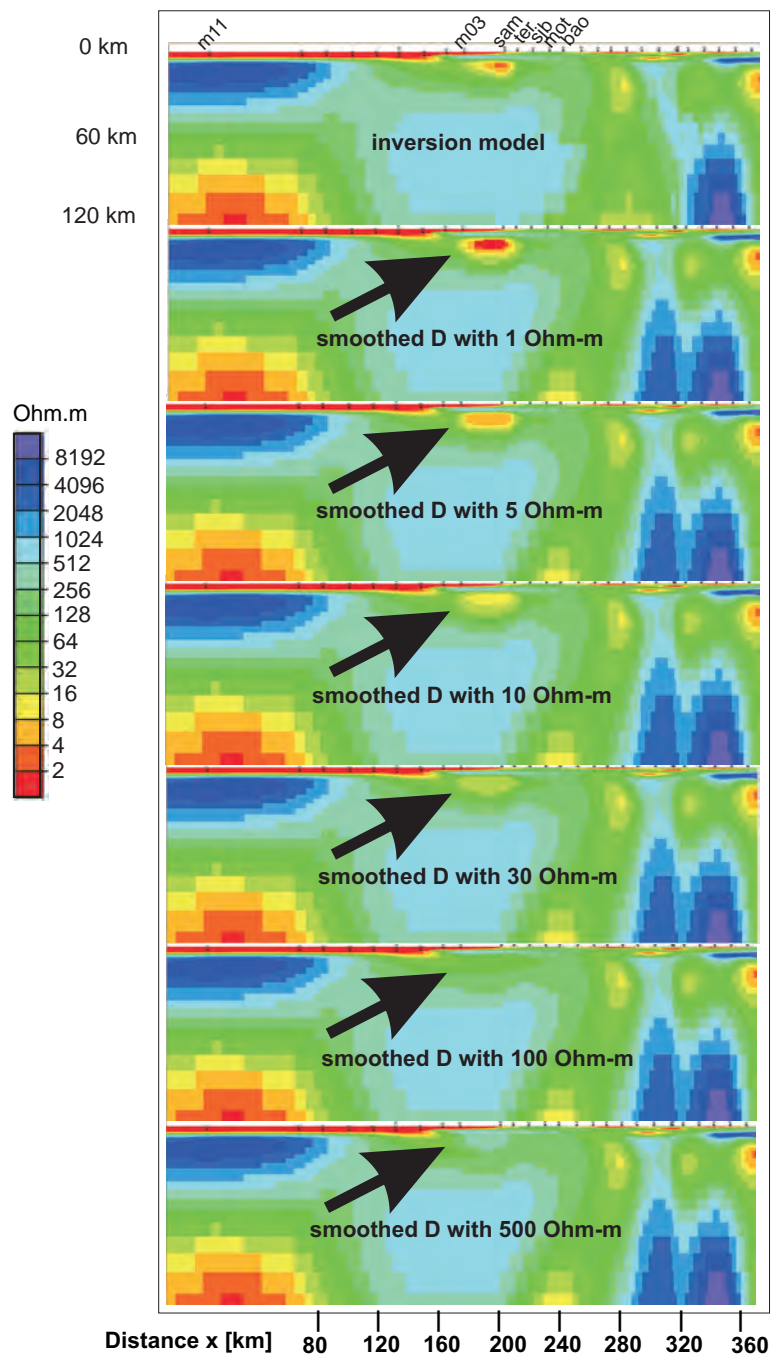


Figure 7.1: Resolution tests on anomaly D with “smoothed out” boxes. Six models are displayed with varying resistivities of smoothed anomaly D. Responses are calculated for the six models and are displayed in Figures 7.2 to 7.6. This test is run to erase concerns about using vertical boxes instead of smoothed out regions.

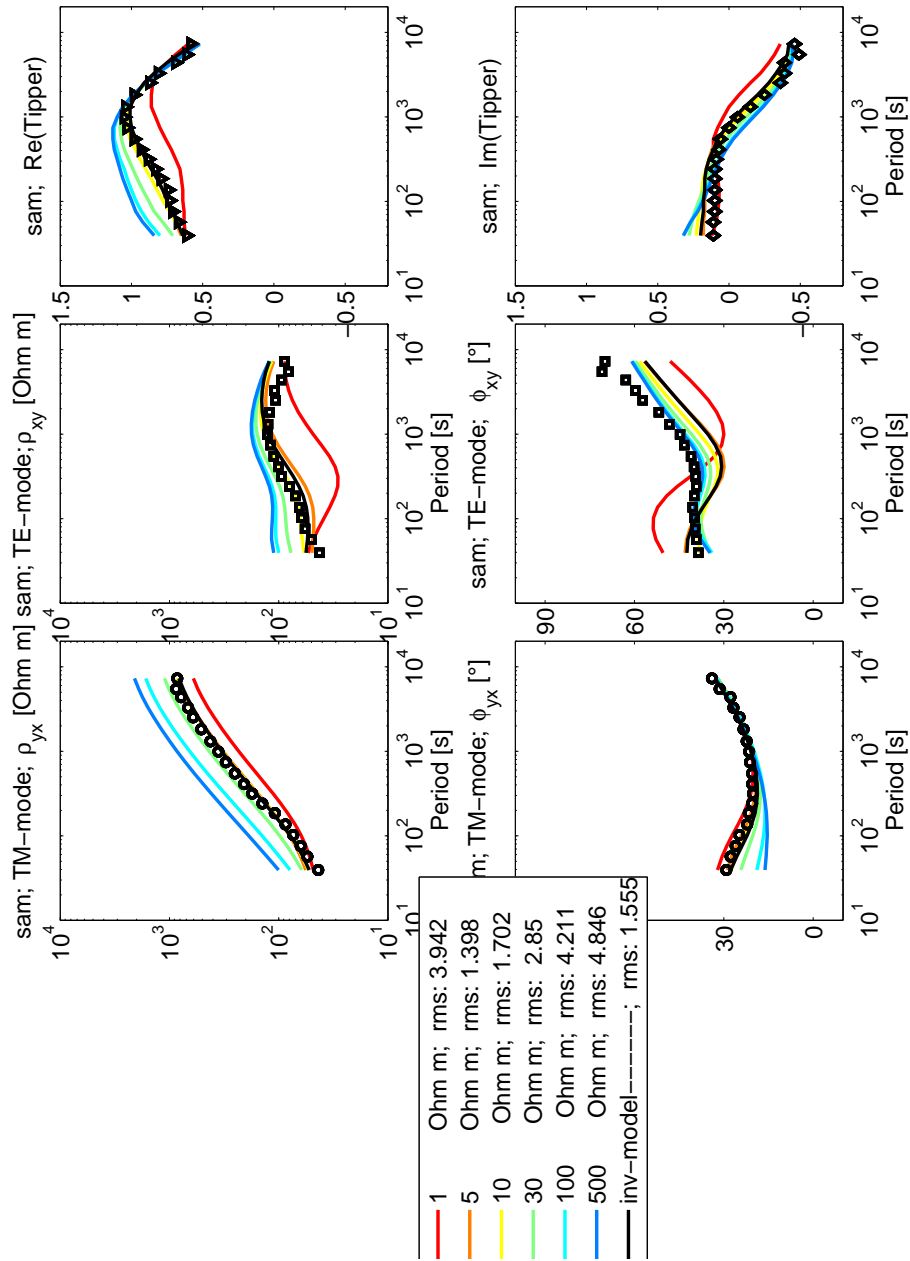


Figure 7.2: Resolution tests for anomaly D at station “sam”.

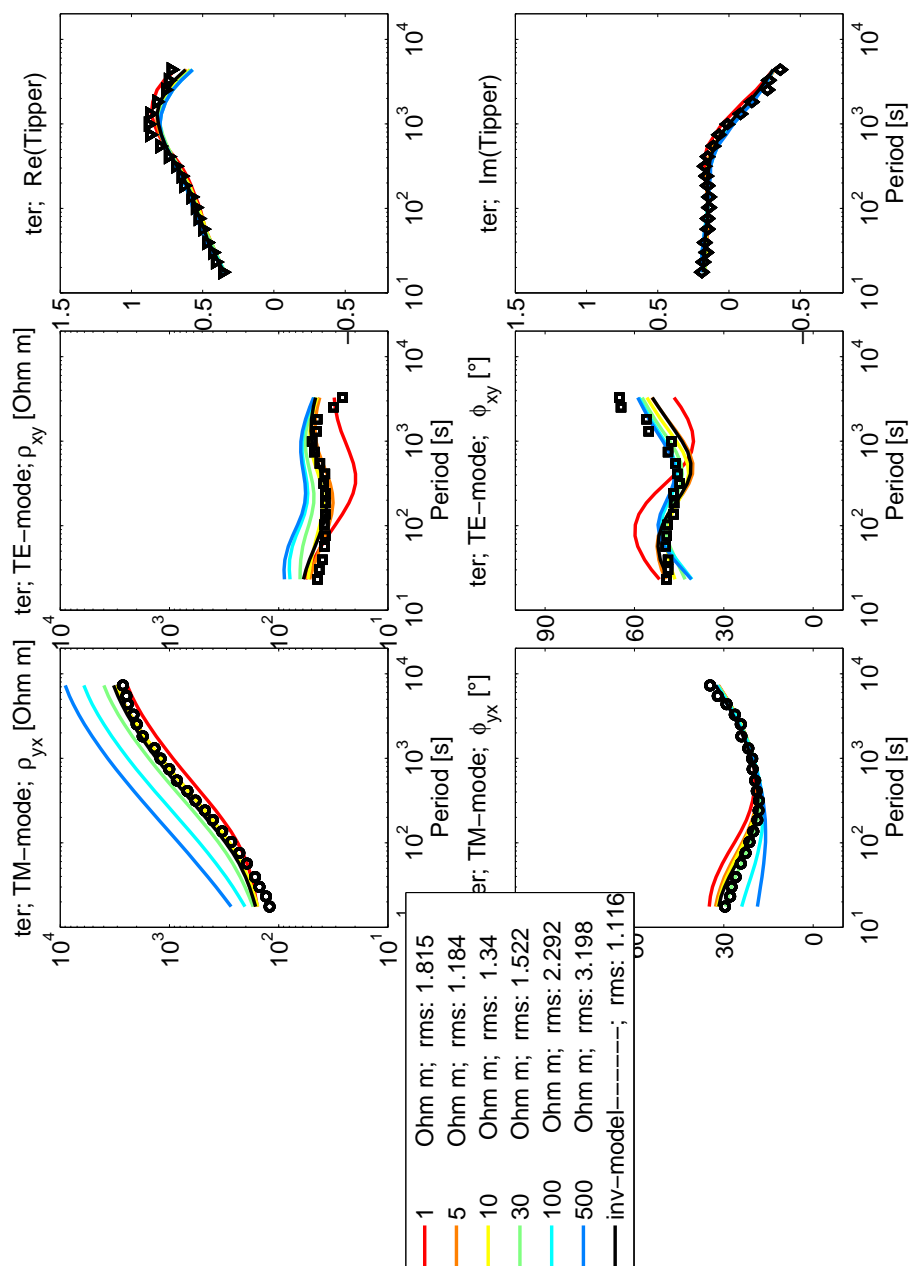


Figure 7.3: Resolution tests for anomaly D at station “ter”.

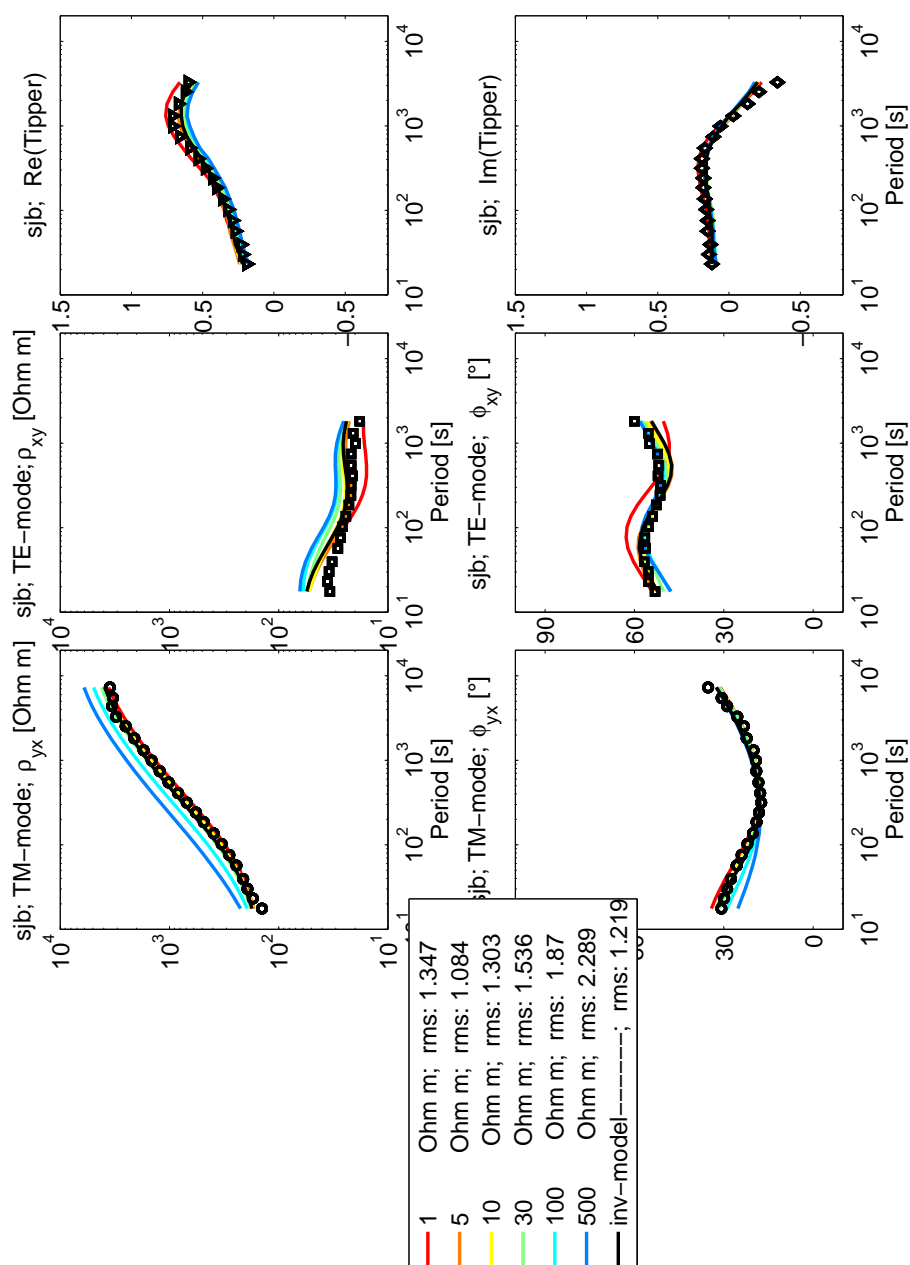


Figure 7.4: Resolution tests for anomaly D at station “sjb”.

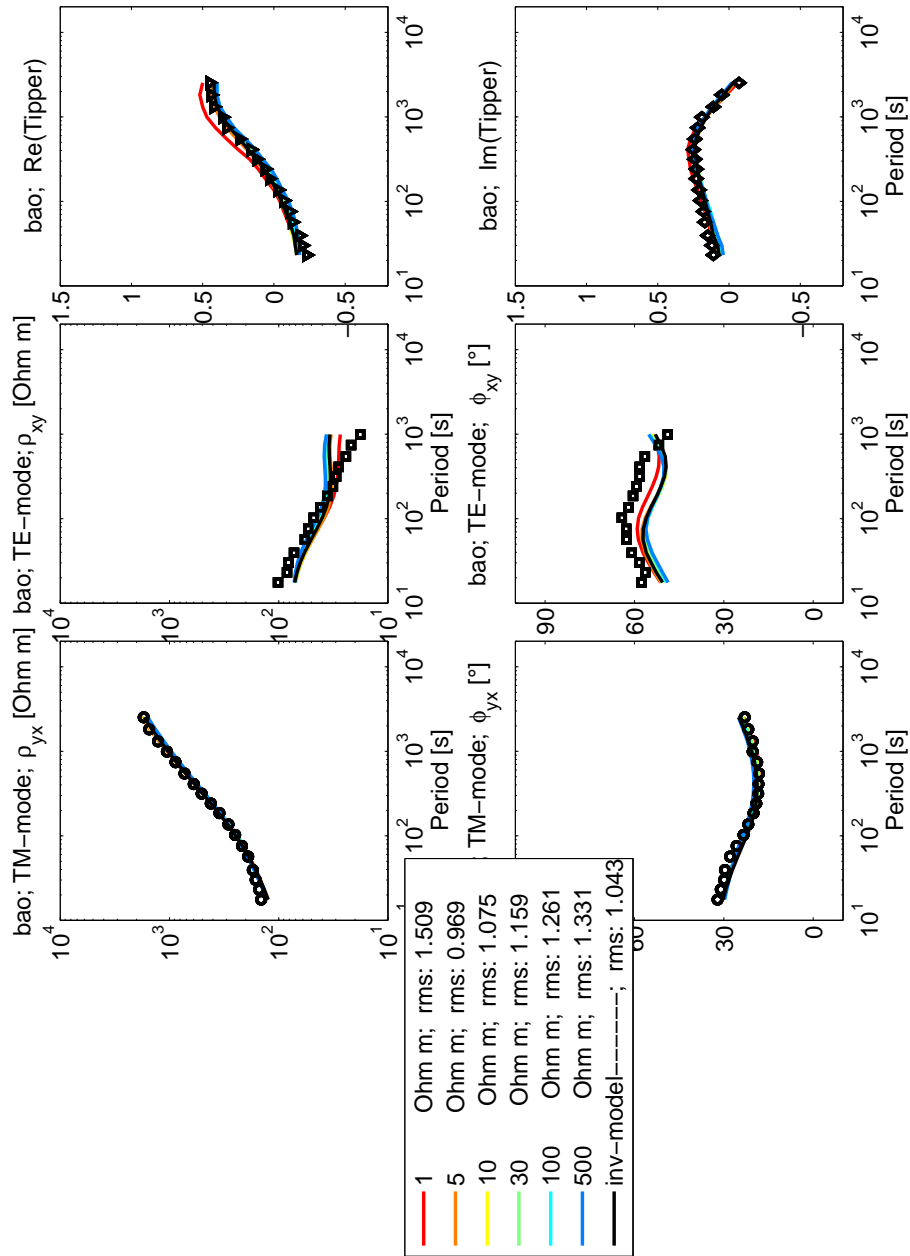


Figure 7.5: Resolution tests for anomaly D at station "bao".

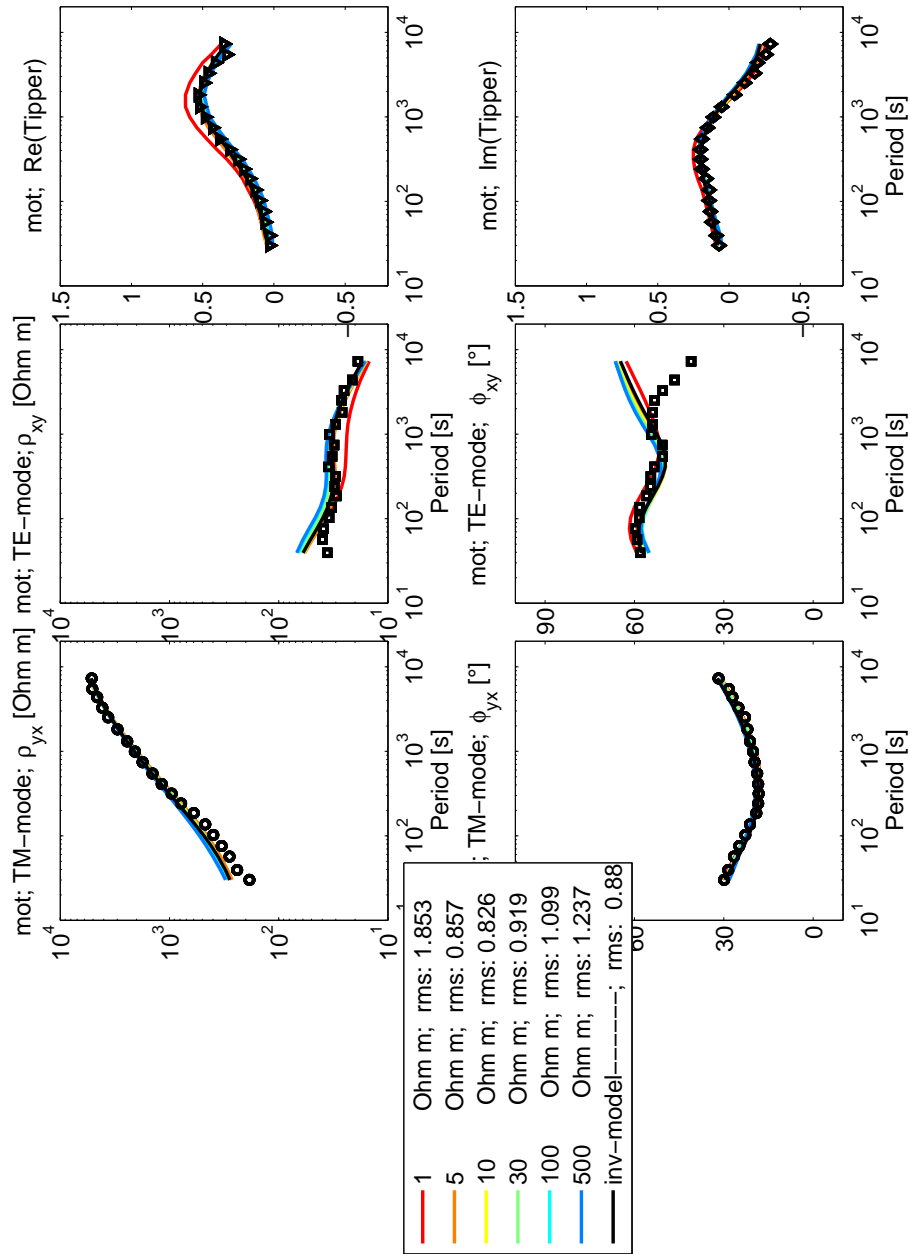


Figure 7.6: Resolution tests for anomaly D at station “mot”.

7.4 A test for Anomaly G: Blob or Line?

Many seismologic investigations at subduction zones have shown that, besides the earthquakes originating in the seismogenic zone, there are earthquakes that may be related to anomaly G. On an elongated line from the volcanic arc dipping around $\approx 30^\circ - 60^\circ$ towards the incoming plate, there are often earthquakes observed in a row that sometimes extend to the top of the subducting plate (pers. communication with W. Rabbel, University of Kiel). One hypothesis is, that a characteristic fault zone develops at subduction zones, breaking up the crust of the forearc region between the incoming plate and the volcanic arc. If such fault zones existed, they might be a pathway for fluids to the surface.

Concerning the resolvability of anomaly G, the question was raised whether the recorded data could be also explained by an Earth model that better suits the seismological perspective of the forearc region.

Therefore the question is, whether also an elongated thin conductor can produce a response, which in the inversion process would yield a feature looking like the anomaly G.

In order to test this, a model is constructed that suits the seismologic perspective: A thin and highly conducting interconnected line ($0.01 \Omega m$) is constructed with a dense grid in a subduction setting as shown in Fig. 7.7. Uppermost panel i) shows an overview of the area, panel ii) is a magnification of the conducting line, panel iii) displays the dense grid needed for constructing a thin conductor, panel iv) shows a further magnification of the conducting line together with the grid.

The model is calculated forward adding 10% of random Gaussian noise in order to simulate real data. Thereafter, the forward responses of the (noisy) model are saved as station data, while stations are placed on land around the commuting area of the anomaly (black triangles at the surface). The next step is to construct a homogeneous starting model with a coarser grid as one would normally perform without knowing the anomalies in the Earth. The “normal” starting model is displayed in Fig. 7.8 v)-vii). The magnified segment in vii) is shown in comparison to the magnified segment of the original model viii), in order to illustrate the much coarser grid of the starting model, respectively.

The next step is to perform a standard inversion with the starting model given in Fig. 7.8. Combined inversions of TE mode, TM mode and Tipper data are performed with various trade-off parameters τ . As discussed in Section 2.3.7, the trade-off parameter regularizes a compromise between smoothness of the model and data misfit, which is measured by the root mean square (rms). In Fig. 7.9 inversion

results after 200 iteration steps are shown for different values of τ . A small value for τ will yield the best data fit (smallest rms) at the expense of smoothness - the anomaly is well resolved but the model fairly rough (second panel). With increasing τ , the model becomes smoother at the expense of a higher rms (third to bottom panels). An extremely large value of τ ($\tau = 100$) in fact yields an inversion result in which the conducting line becomes “blobby”. However, this high value of τ would normally not be performed in an inversion as τ is chosen to from an L-curve at the highest curvature (a common criterion for choice of trade-off parameter). Fig. 7.10 shows the L-curve of the model shown in Fig. 7.7, the best choice for τ ranges between 0.3 and 6. For these values of tau, the nature of a conductive line can be well resolved.

The data in Costa Rica were inverted with a trade-off parameter chosen from the highest curvature of the L-curve as discussed in the Supplementary information in Chapter 5. This test here confirms that an educated choice of τ would resolve a structure as assumed from seismologic perspective. Therefore it can be assumed that the G-anomaly is not associated with a thin highly conductive line that extends from the downgoing slab’s top to the volcanic arc.

Forward model containing thin conductor calculated with dense grid. Responses are saved as station data.

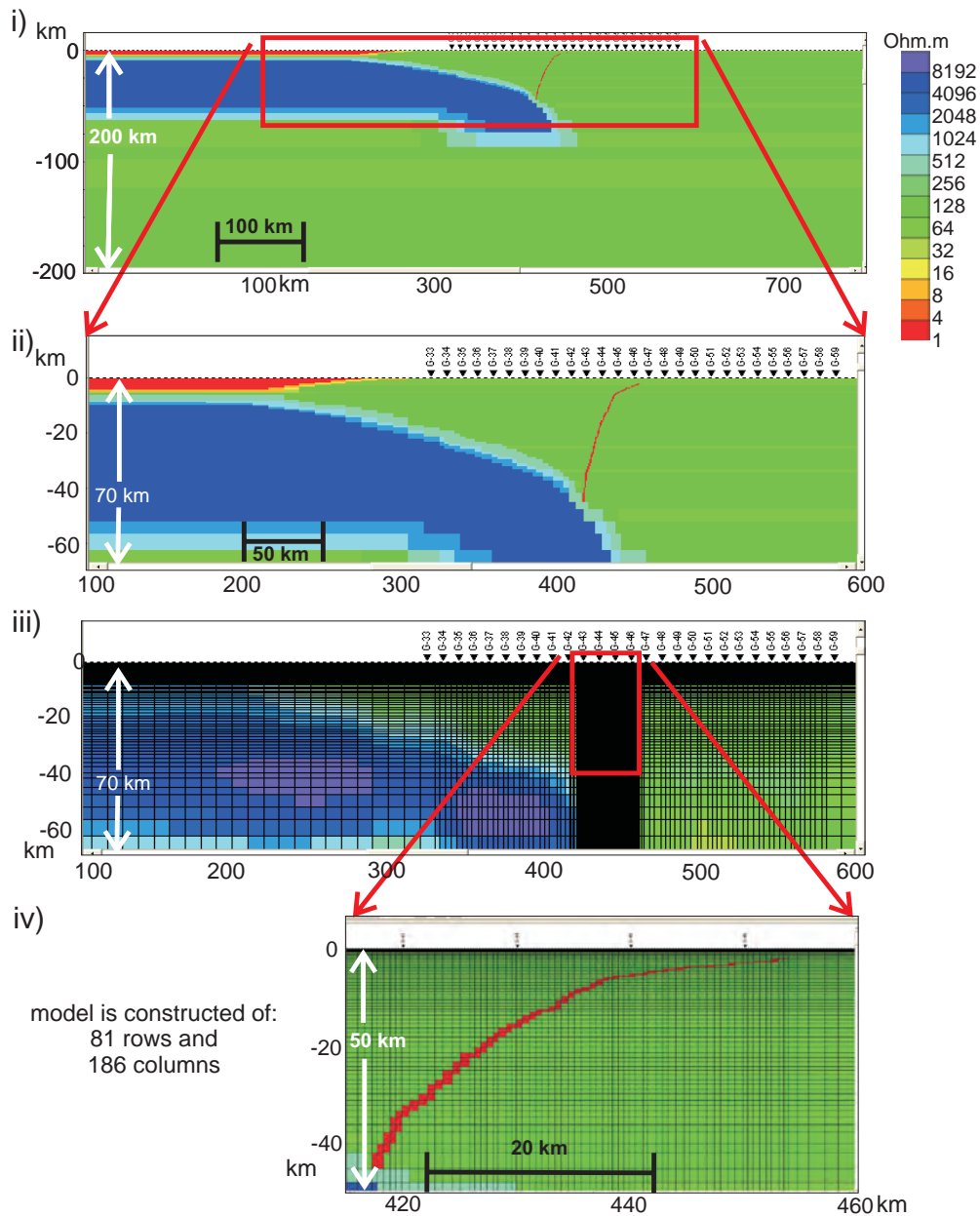


Figure 7.7: Rabbeltest page 1

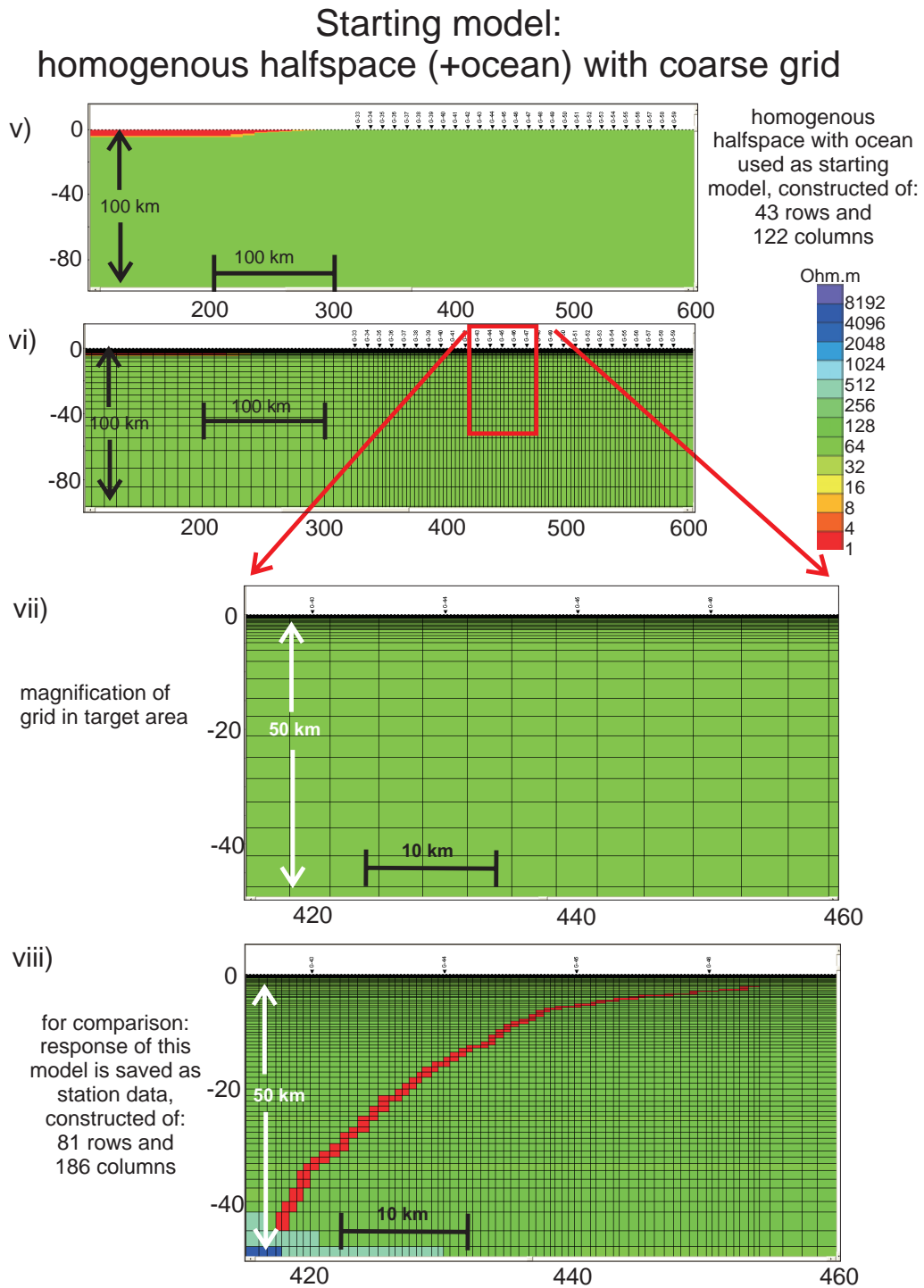


Figure 7.8: Rabbeltest page 2

Inversion tests for different smoothing parameters

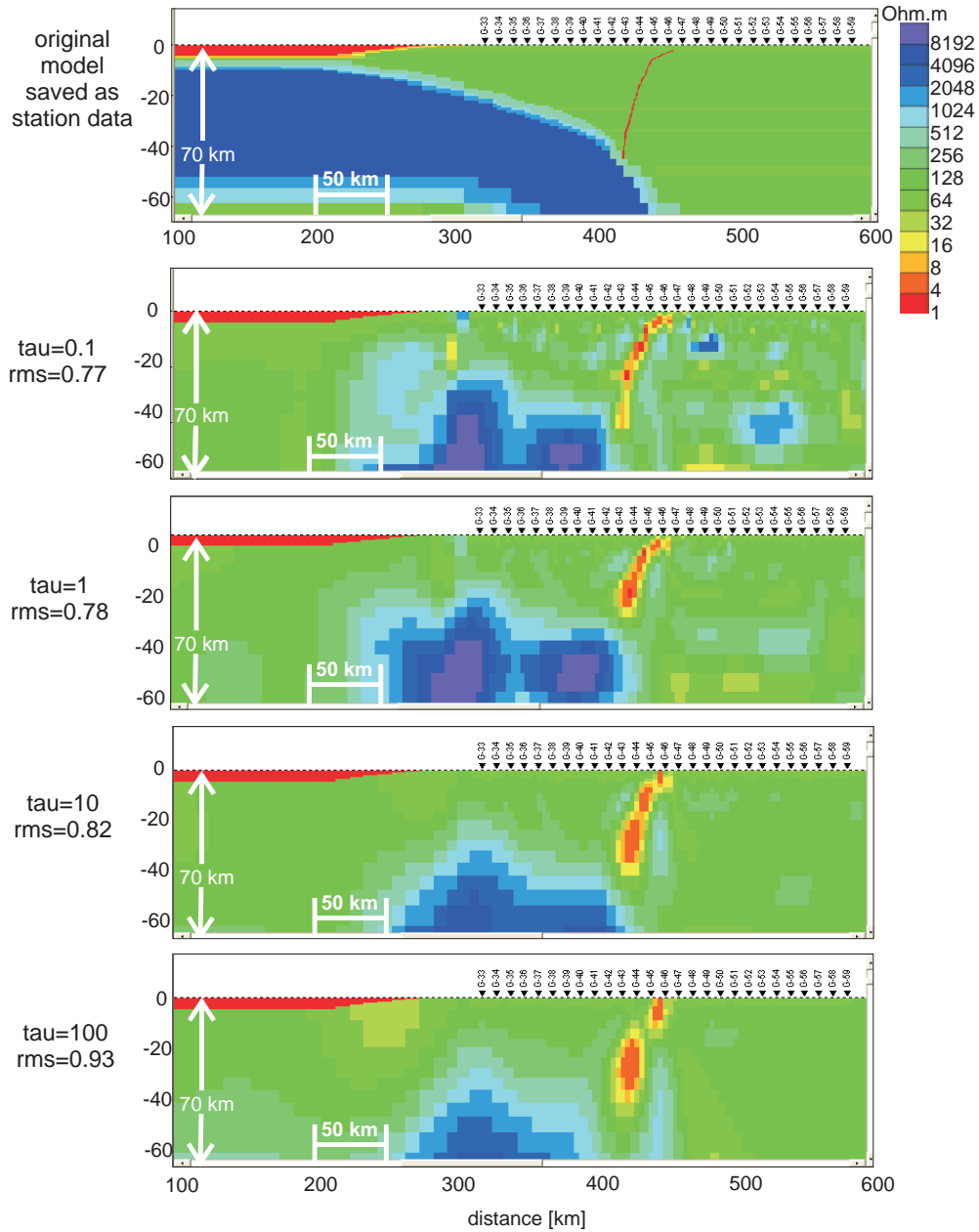


Figure 7.9: Rabbeltest page 3

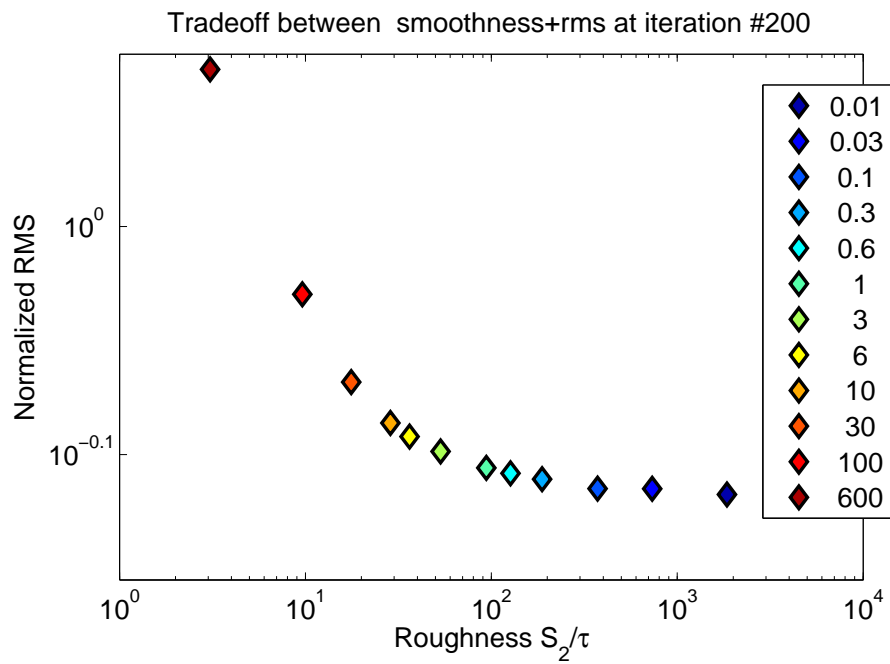


Figure 7.10: The L-curve for the inversion of model shown in Fig.7.7. The best trade-off parameter is normally chosen where the curvature of the L-curve is highest. Here the best choice is provided for values of τ between 0.3 and 6.

7.5 Anomaly G in other MT surveys

The MT surveys on subduction zones with G-anomalies in the world as discussed in Chapter 5, are now compared to each other.

The inversion results of the MT surveys are summarized in Figures 7.11 to 7.17. The models in the studies all have different quality, resolution and also very different inversion parameters (such as smoothing). In order to be on the safe side a maximum error is assigned to the G-anomalies. This means that the error bars are drawn over the whole extension of the anomaly (except for the extremely smoothed model of Mexico). Figures 7.11 to 7.17 display how the error-bars are selected, the Figure captions state the extent of the anomalies. However, the depth position may be underestimated due to the uncertainty of its depth extend but its center should lie within the error bar given.

Fig. 7.18 displays the young developing subduction zone of New Zealand's South island (volcanic arc and trench not yet developed). Conductive zones ontop of the downgoing slab are interpreted as fluids from dehydration reactions, but in comparison to all the other "mature" subduction zones, these conductivity anomalies are more resistive. This implies that incoming fluids have to yet reach a threshold value required for promoting upperplate melting required for active volcanism.

Fig. 7.19 compares other physical information on the subduction zones collected by Clift and Vannucchi [2004]. All subduction zones presented here differ from each other in terms of age, type of subduction zone (erosive or accretionary), age, convergence rates, ... However, despite differences among the subduction zones, they all display the G-anomalies.

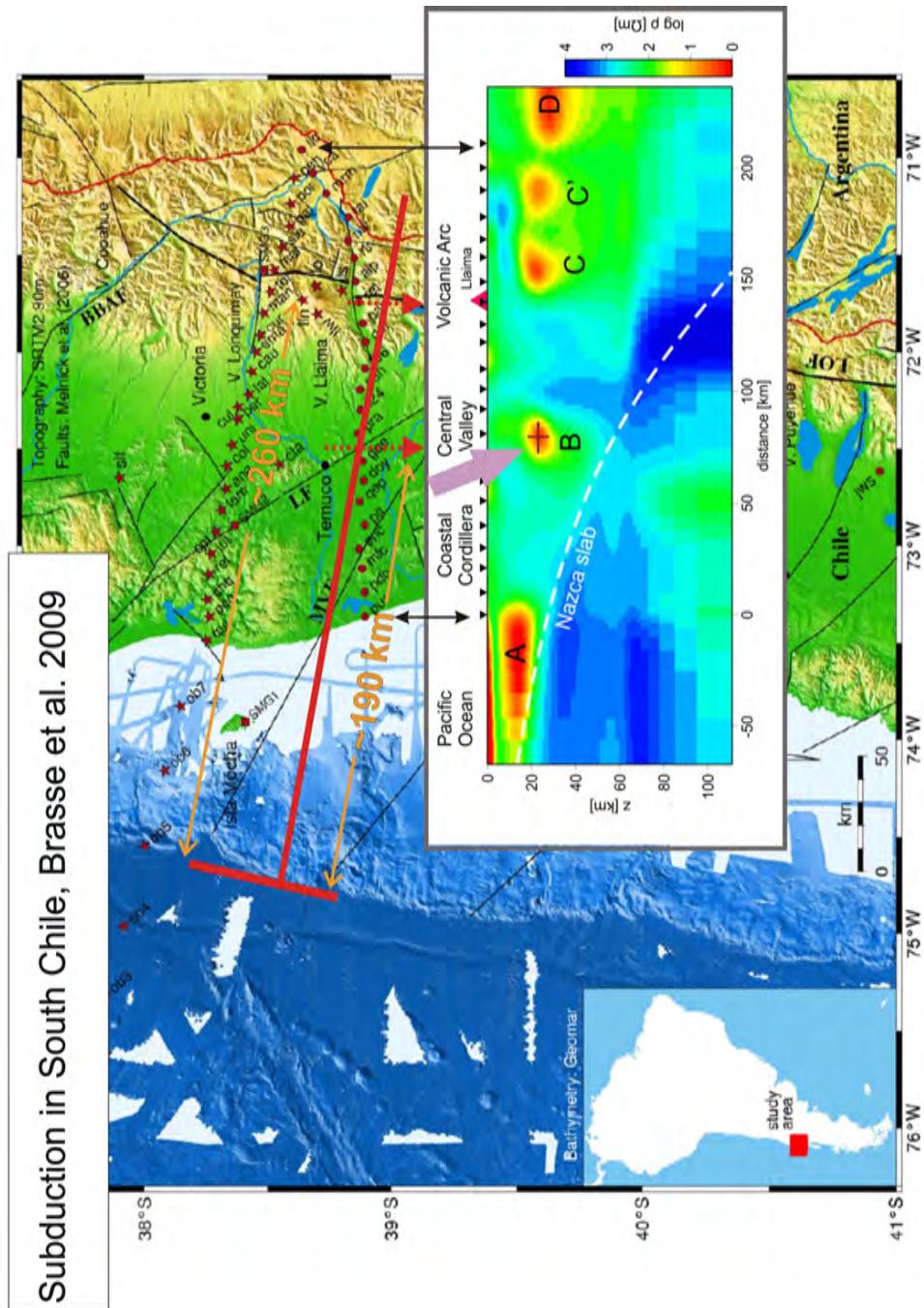


Figure 7.11: G-Anomaly with error bars in South Chile, here denoted as “B”. Brasse et al. [2009a] associated it with a fault zone. Anomaly B is approx 70 ± 5 km seaward from the volcanic arc at 25 ± 5 km depth.

Schwalenberg et al 2001
Brasse et al. 2002,

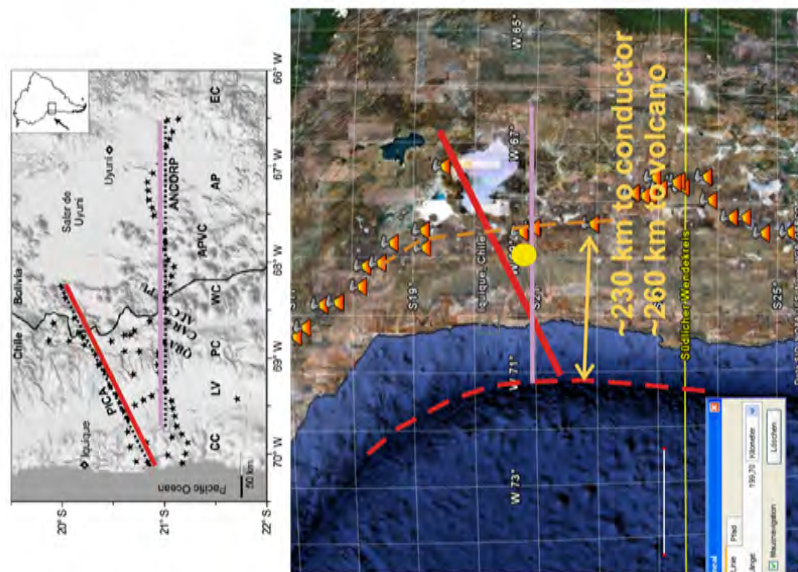


Figure 7.12: G-Anomaly with error bars in North Chile. The unnamed anomaly is approx 25 ± 5 km seaward from the volcanic arc at 20 ± 5 km depth (Schwalenberg et al. [2002]).

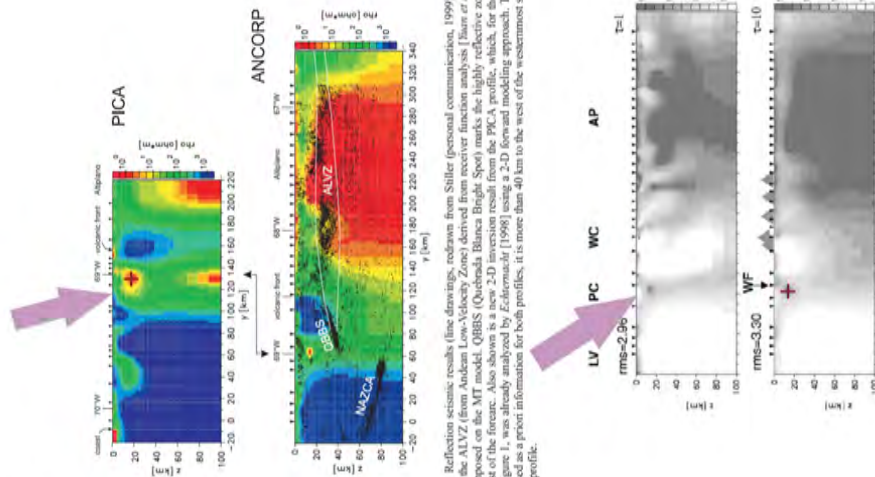


Figure 8. Reflection seismic results (line drawings, redrawn from Sillier (personal communication, 1999)) and the location of the LV and AP profiles (see Figure 1). The PICA profile is the same as the one shown in Figure 1, but inverted on the MT model. OBS (Oval) and B (Black) marks the highly reflective middle crust of the forearc. Also shown is a new 2-D inversion result from the PICA profile, which, for the Chilean side, see Figure 1, was already analyzed by Ezkura et al (1998) using a 2-D forward modeling approach. The ocean has been used as a priori information for both profiles; it is more than 40 km to the west of the westernmost site on the ANCORP profile.

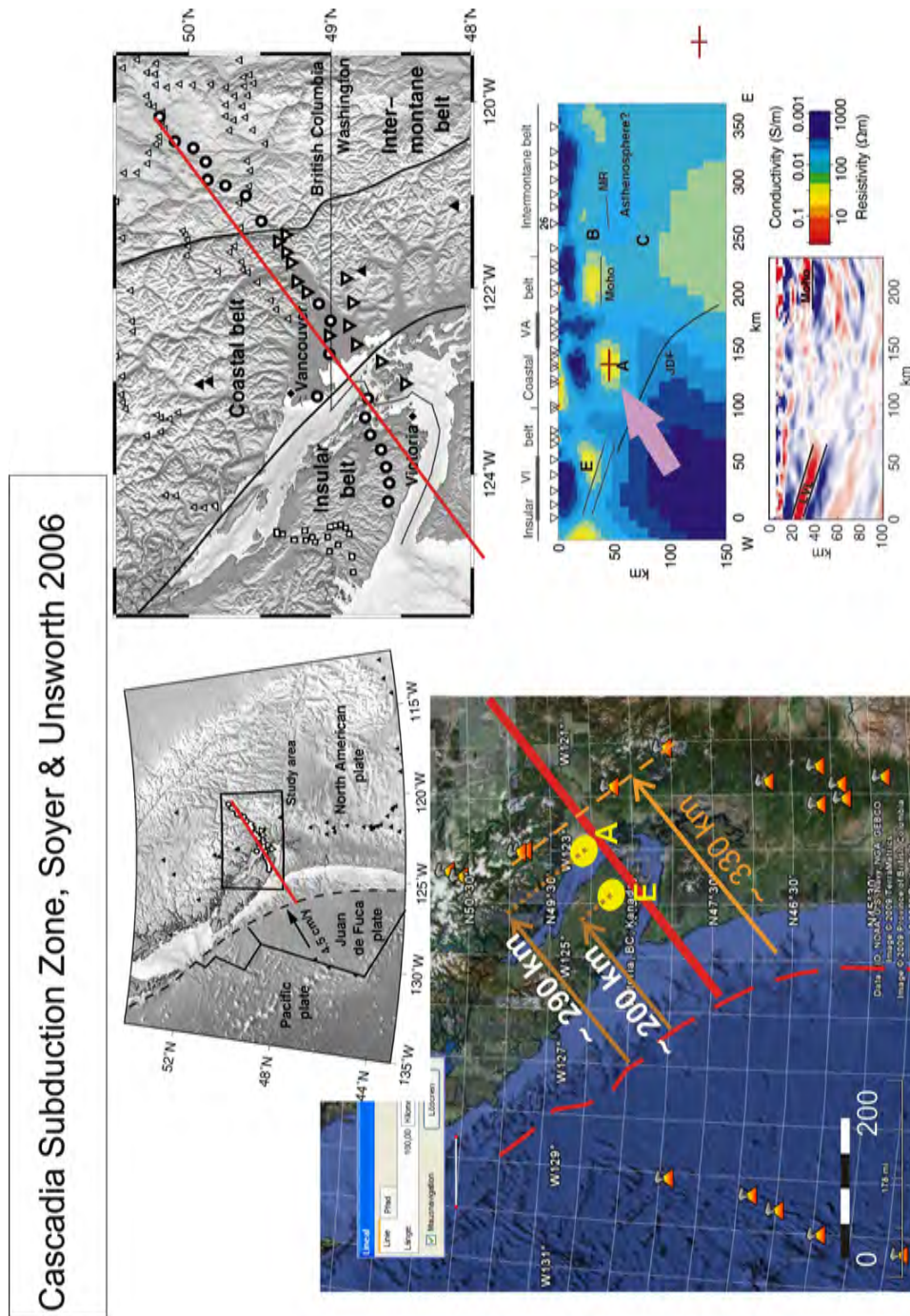


Figure 7.13: G-Anomaly with error bars in Cascadia, Oregon, here denoted as “A” (Interpreted as hydrous mantle wedge). Anomaly A is approximately 40 ± 10 km seaward from the volcanic arc at 40 ± 5 km depth.

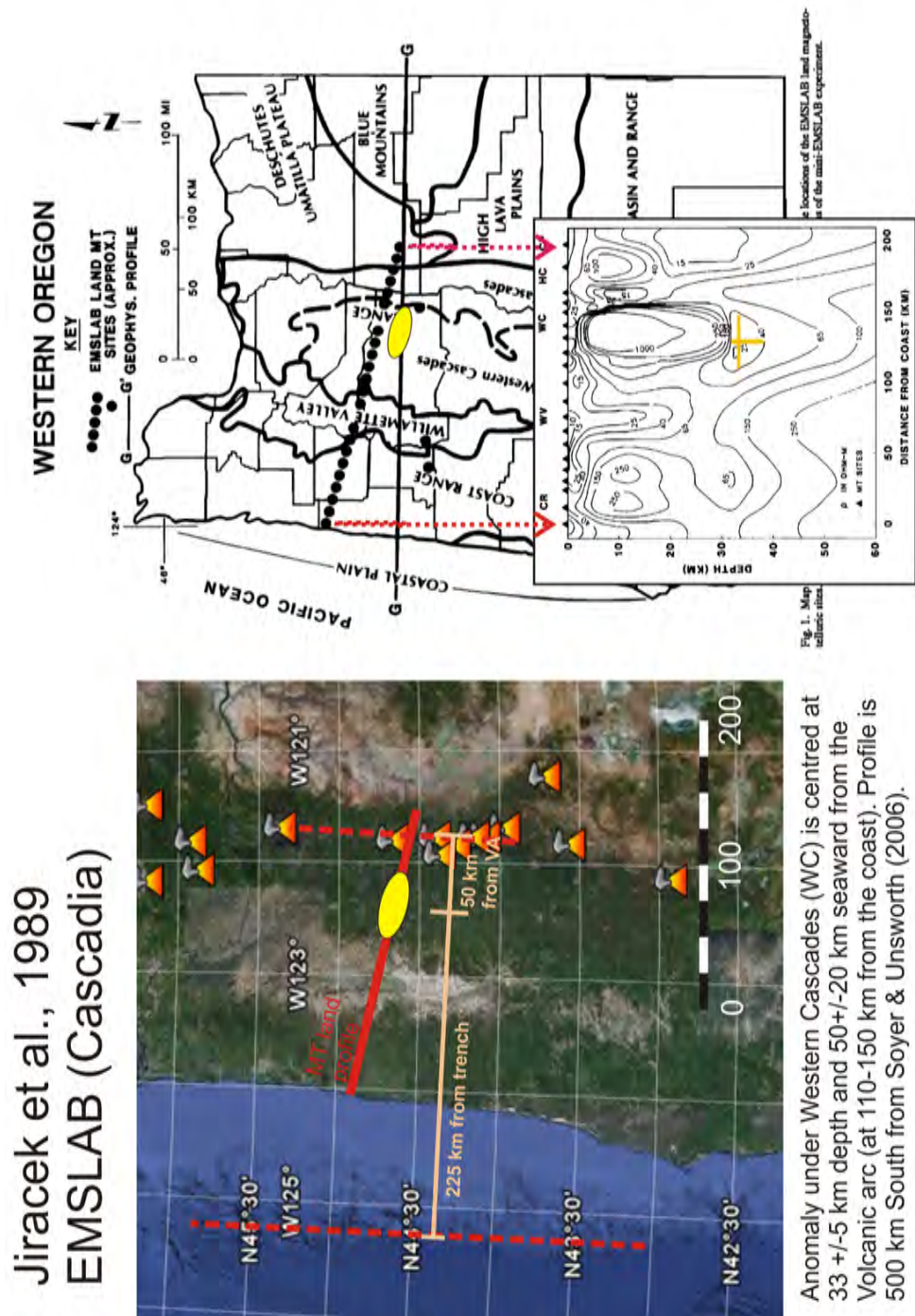


Figure 7.14: G-Anomaly with error bars in Cascadia, British Columbia (EMSLAB project, Jiracek et al. [1989]). The anomaly is approximately 50 ± 20 km seaward from the volcanic arc at 35 ± 5 km depth.

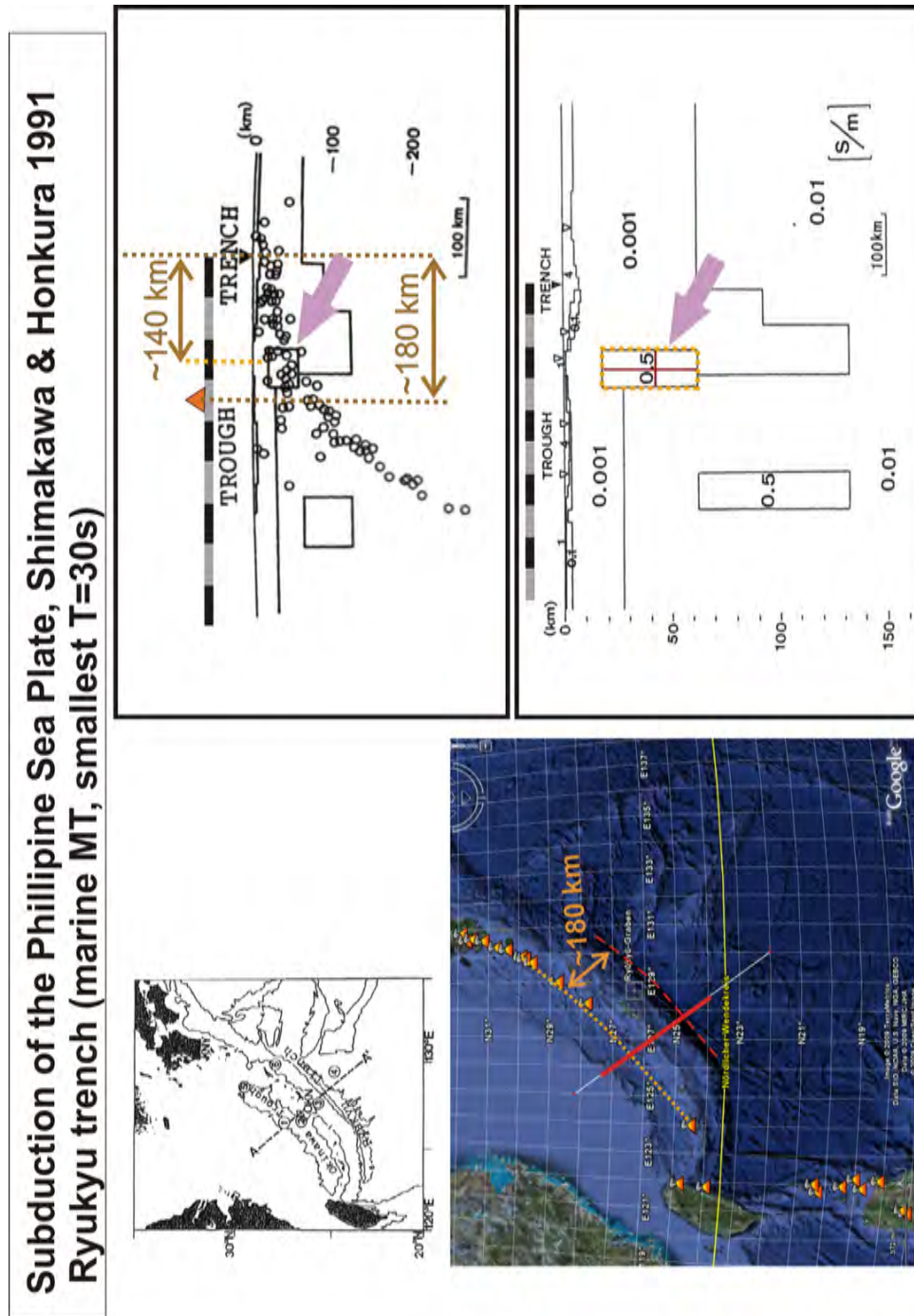


Figure 7.15: G-Anomaly with error bars of the Philippine Sea plate (Ryukyu Trough). Anomaly is approx 40 ± 25 km from the trench at 40 ± 20 km depth, Shimakawa and Honkura [1991].

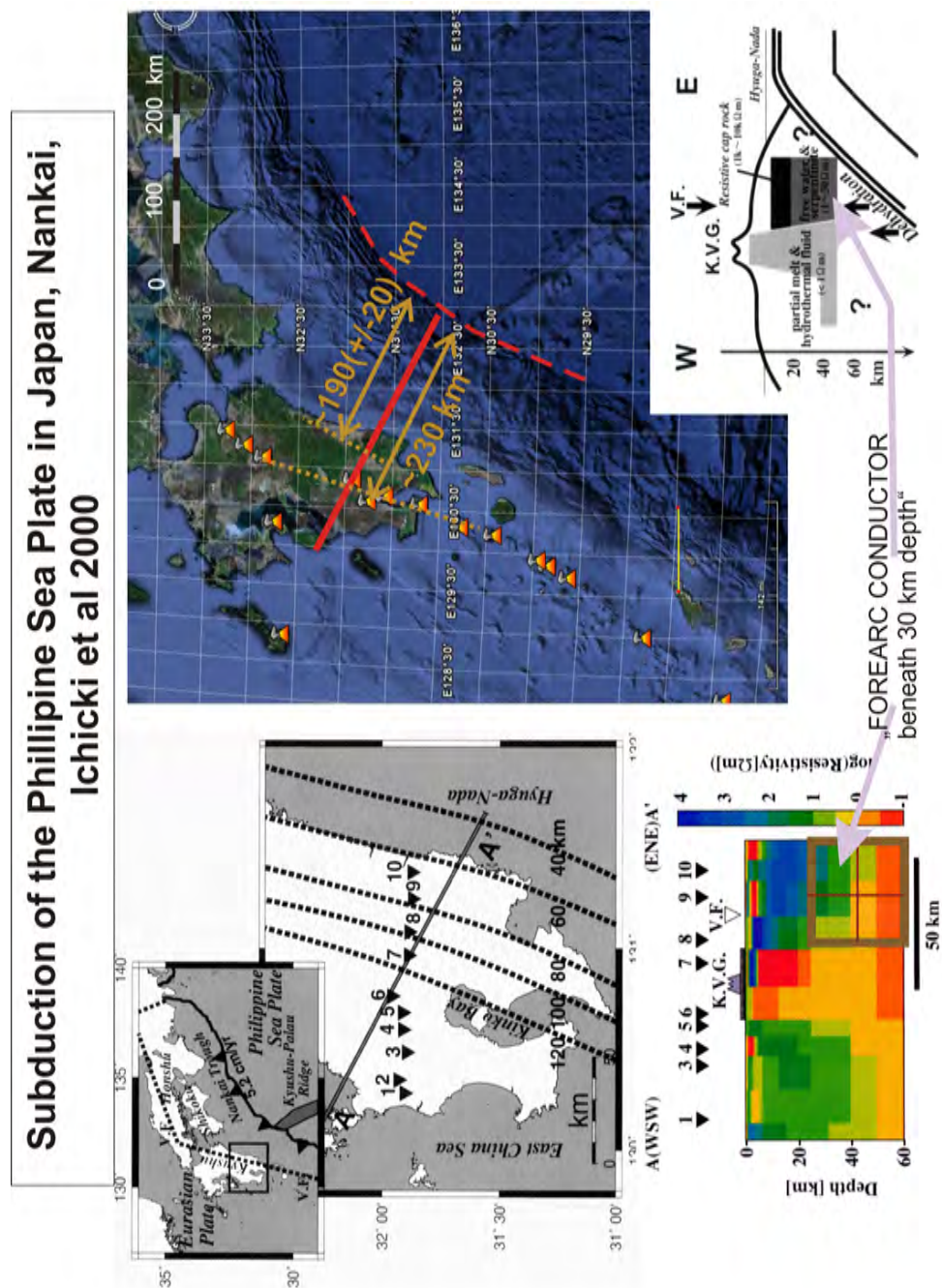


Figure 7.16: G-Anomaly with error bars in Japan (Nankai). Ichiki et al. [2000] interpret the “forearc conductor beneath 30km depth” as free water and serpentinite. The whole area defined by them is marked with a distance to volcanic arc of 40 ± 20 km at a depth of 40 ± 15 km.

Hellenic Subduction zone, Galanopoulos 2005

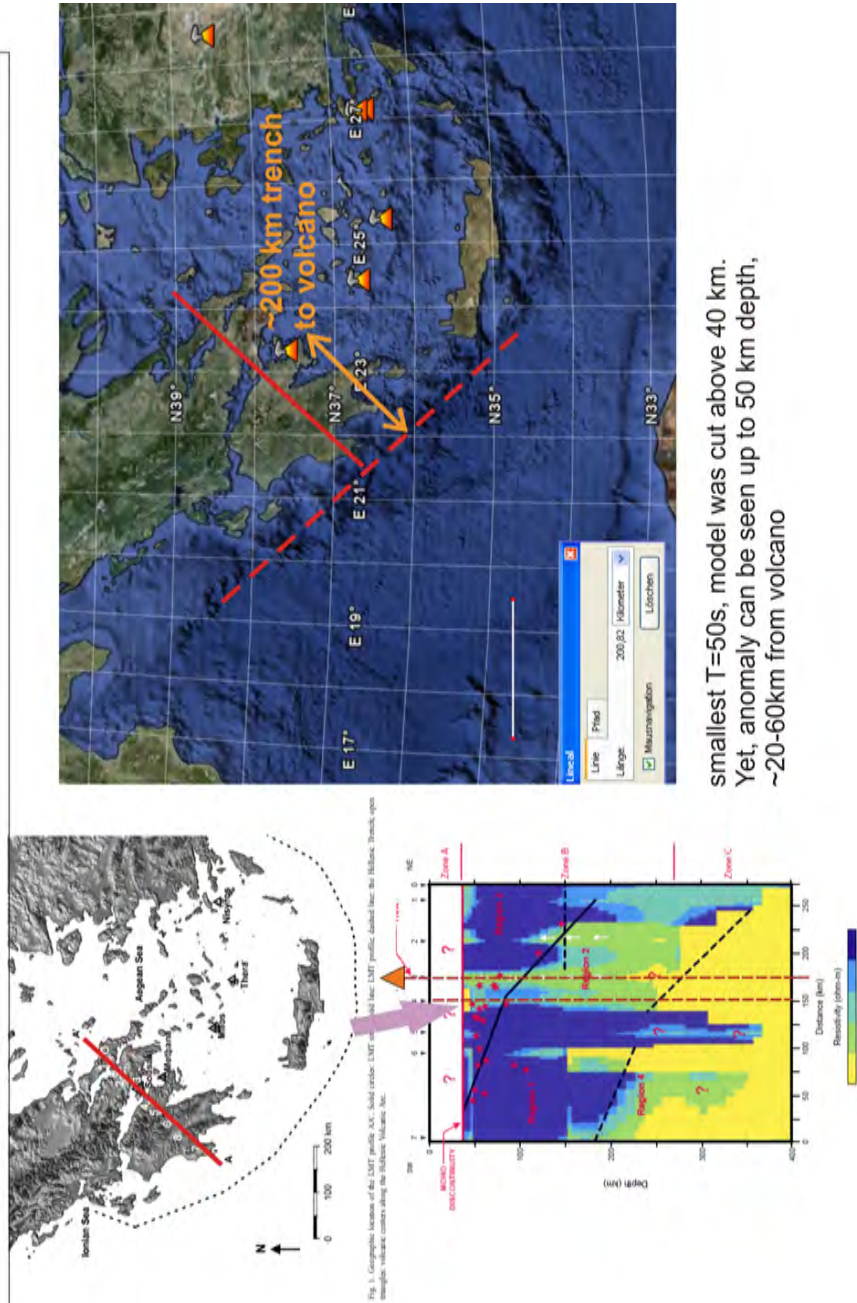


Figure 7.17: G-Anomaly with error bars in Greece, Aegean subduction zone, see inversion on left bottom (Galanopoulos et al. [2005]). G is pointed out by purple arrow on top. Anomaly is approx 30 ± 15 km from trench at $35 + 10$ km depth.

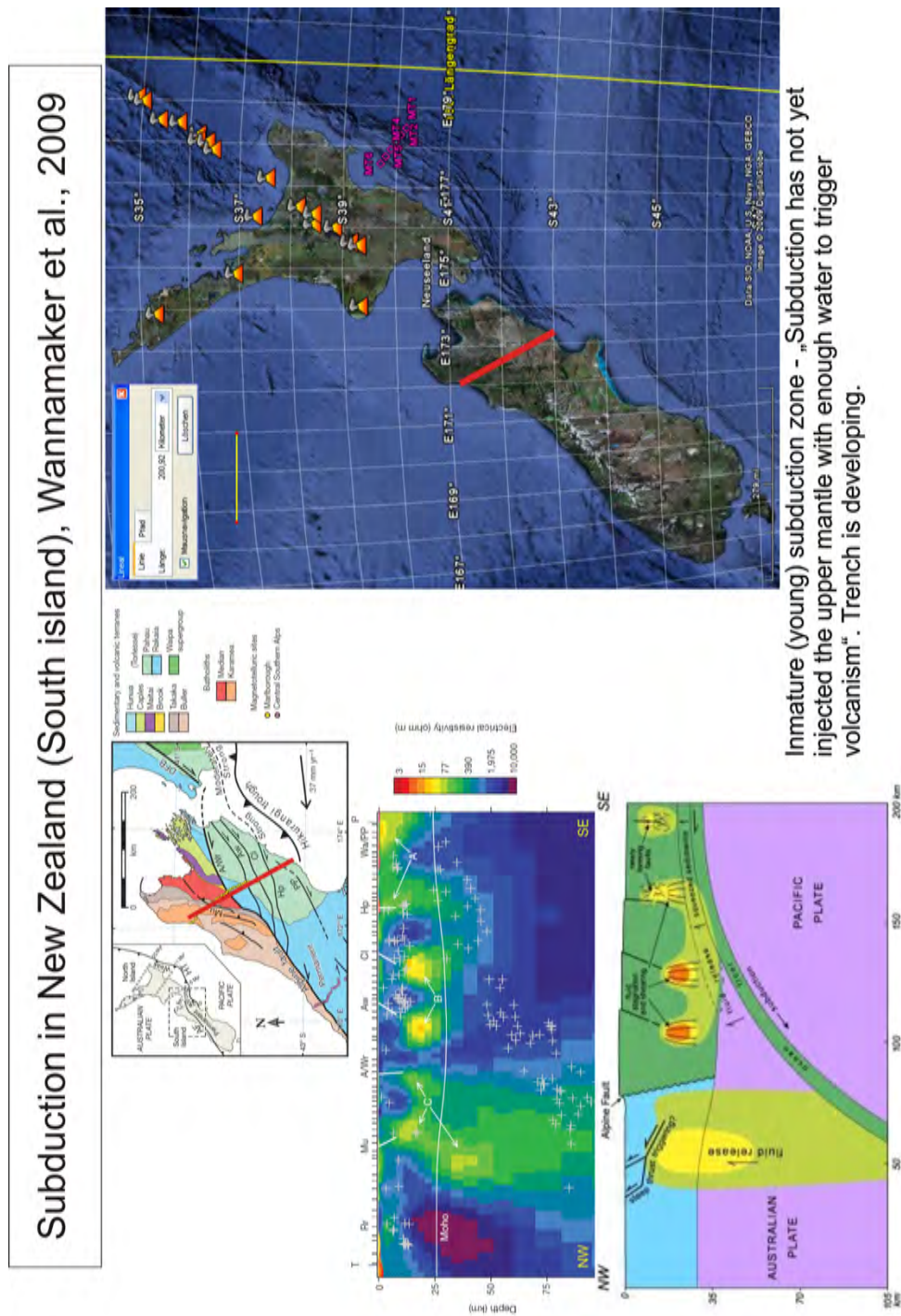


Figure 7.18: New Zealand - not yet developed subduction zone, Wannamaker et al. [2009].

where:	Latitude	Longitude	Distance [km] Anomaly - Trench	Distance [km] Anomaly-Volcanic Arc	Depth [km] Anomaly	AGE of Oceanic Plate	Erosion or Accretion	Orthogonal Conver- gence rate [mm/yr]
North Chile	39°S	73.5°W	230	25 +/-5	20 +/-5	-41	E	-83
Costa Rica	10.3°N	85.3°W	150	30 +/-5	25 +/-8	24	E	80
Mexico (B-B')	18.5°N	99.5°W	330	20 +/-10	40 +/-8	10	E	68
Ryukyu (Philippine Sea Plate)	25°N	127°E	140	40 +/-25	40 +/-20	53	E	69
South Chile	21°S	69°W	190	70 +/-5	25 +/-5	36	A	20
Cascadia	49°N	123°W	230	40 +/-10	40 +/-5	8	A	40
SW Japan (Nankai)	31°N	131°E	190	40 +/-20	40 +/-15	25	A	40
Aegean (Greece)	37.5°N	22.5°E	170	30 +/-15	35 +/-10	220	A	20

more properties of these subductin zones, information taken from Clift & Vannucci (2004), Rev. of Geophysics

where:	Taper- angle [deg]	forearc Slope- angle [deg]	Trench Retreat rate [km/Ma] AND Age of Margin [Ma]	Sediment porosity [%]	Sediment delivery rate [km ³ /Ma]	Material Subduction Rate [km ³ /Ma]	Magmatic produc- tivity [km ³ /Ma]	Net Crustal Growth Rate
North Chile	-7.6	-3.5	3 mm/a	48	~20	-155	-112	-25
Costa Rica	7.6	3.4	3 mm/a	48	17	122	108	3
Mexico (B-B')	13.4	6	1 mm/a	47	20	60	91	51
Ryukyu (Philippine Sea Plate)	11.7	5.2	3 mm/a	48	13	103	93	3
South Chile	7.6	2.2	15 Ma	33	43	36	27	34
Cascadia (feature A)	5.7	1.8	50 Ma	37	~55	-45	-49	59
SW Japan (Nankai)	9.6	2	140 Ma	27	65	41	53	77
Aegean (Greece)	3.5	0.5	35 Ma	18	131	109	27	49

Figure 7.19: Physical properties of subduction zones. Summarized from Clift and Vannucchi [2004].

7.6 Dimensionality analysis

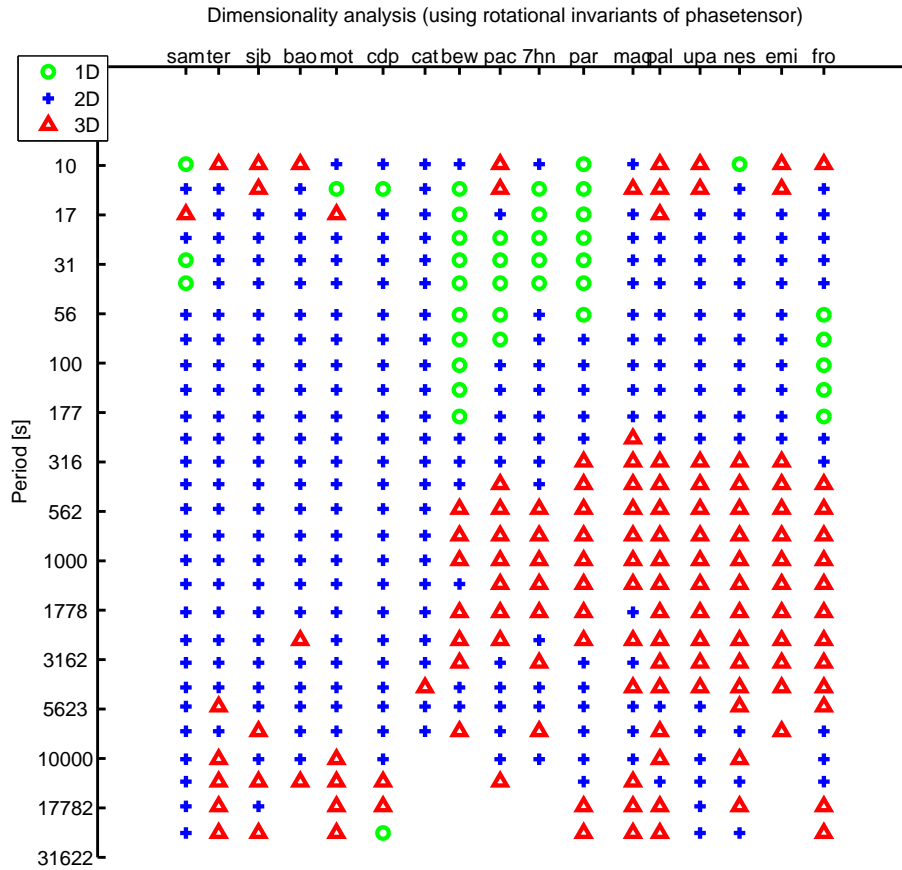


Figure 7.20: Dimensionality analysis using rotational invariants of phase tensor.

The data generally support a 2D assumption. Fig. 7.20 depicts a dimensionality analysis of the land data. It shows the modified dimensionality analysis after Weaver and A. K. Agarwal [2006] at all periods. The phase-tensor as defined by Caldwell et al. [2004] is decomposed into one-, two- and three-dimensional contribution terms, which are characterized through rotational invariants. Particular weighting of rotational invariants determines the dimensionality of the recorded fields. Flow chart diagram is modified after Worzewski [2005]. In the land a three-dimensional influ-

ence arises from the east (right) that is sensed by the easternmost land stations at higher periods (red triangles). In the inversion plot, we marked this area transparent due to the proximity to the profile end. The important anomalies discussed in this manuscript are not within the debatable section. In the marine case the phase tensor is not independent of galvanic distortions such that this dimensionality analysis may not be applied.

The geology of the incoming plate however is less complex than the continental plate, such that no severe 3D anomalies are anticipated. This hypothesis is further supported by

- Strike angle analysis (maximization of off diagonal angles) of marine data (see Fig.7.21).
- 2D nature of land MT data in direct proximity of the coast.
- The data can be fitted with a 2D model (knowing that this is not a sufficient condition for two-dimensionality, only a necessary condition).

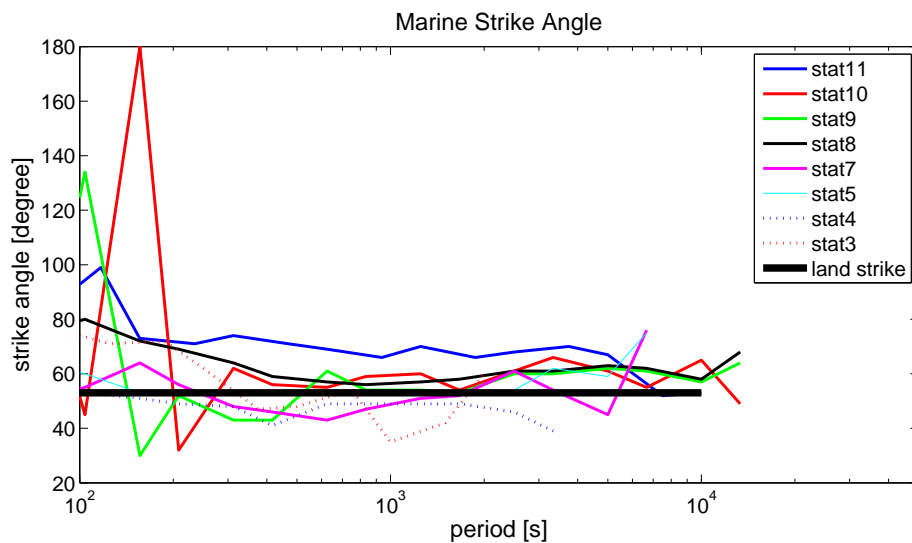


Figure 7.21: Strike analysis of marine impedance tensor for periods. Strike angle of 53° as found by Brasse et al. [2009b] fits well to marine responses.

7.7 Shaking apparatus for testing motion induced noise in Viehdamm

In order to test the OBMT instrument for the effects of motional noise and static rotations, a simple rough-and ready apparatus was constructed that, on the one hand, allows for the rotation of the instrument by 360° , and on the other hand allows for a controlled shaking of the instrument at different periods. The aim of the test was to displace the instrument from the Earth magnetic normal coordinate system under known conditions, so the theoretical rotation equations could be tested for validity. Further, a controlled shaking of the station should yield a dataset, which enables to test several noise-reduction techniques, a static reference station nearby yielded reference values for comparison.

The shaking apparatus, the OBMT sensor, different types of batteries, and a reference magnetometer were taken to a remote place of the Schleswig Holsteinsche Schweiz, Viehdamm, where human noise is negligible and the total magnetic field is homogeneous. The homogeneity can be easily checked by comparing values of the total magnetic field vector at varying sites some meters apart, if the field was inhomogeneous due to conducting effects, the total field vector changes. Pictures of the experiment and the shaking apparatus are provided in Fig. 7.22, the building draft is shown in Figs. 7.23 and 7.24.

In Fig. 7.22 a) the remote place is illustrated, where the experiment has been conducted. Fig. 7.22 b.1-3) and c.1-2) provide pictures of the non magnetic apparatus. The apparatus consists of three wooden planes.

The lowest of the wooden planes is adjusted to the horizontal plane with levels. The second wooden plane is connected to the lowest one over a wedge, allowing the upper plane to be tilted or luffed with respect to the lower plane. A circular wooden plane on top allows for a rotation within the second plane. The magnetic sensor in the titan cylinder is fixed on top, and thus can be tilted or rotated to any position.

The second wooden plane is attached to a aluminum rod which connects a car jack in several meters distance from the magnetic sensor (some meters distance are necessary to assure that neither the steel car jack nor the human operator affect the magnetic field around the sensor). Operating the car jack up and down produces a tilt of the second wooden plane in respect to the horizontal (bottom) plane, which is sensed by the tiltmeter sensors.

The recordings of the moving sensor in the titan cylinder is observed on a screen some meters away from the apparatus. While one operates the car jack, another operator observes the response in tilt meter and magnetic sensors and gives com-

mands on frequency and extent of to the operation of the car jack. d) pictures the experiment itself. Test were also run with the magnetic sensor head and the battery as shown in e): both were removed from the titan cylinder and placed in different distances to each other to quantify the effect that lithium and alkali battery have at different distances. In comparison to the reference magnetometer it could be approved, that lithium batteries hardly affect the magnetic recordings, whereas alkali batteries badly distort the magnetic field registrations depending on the distance to the sensor.



Figure 7.22: Pictures of Shaking Apparatus and test measurements at Viehdamm, apparatus was designed and build by Björn Lewitz.

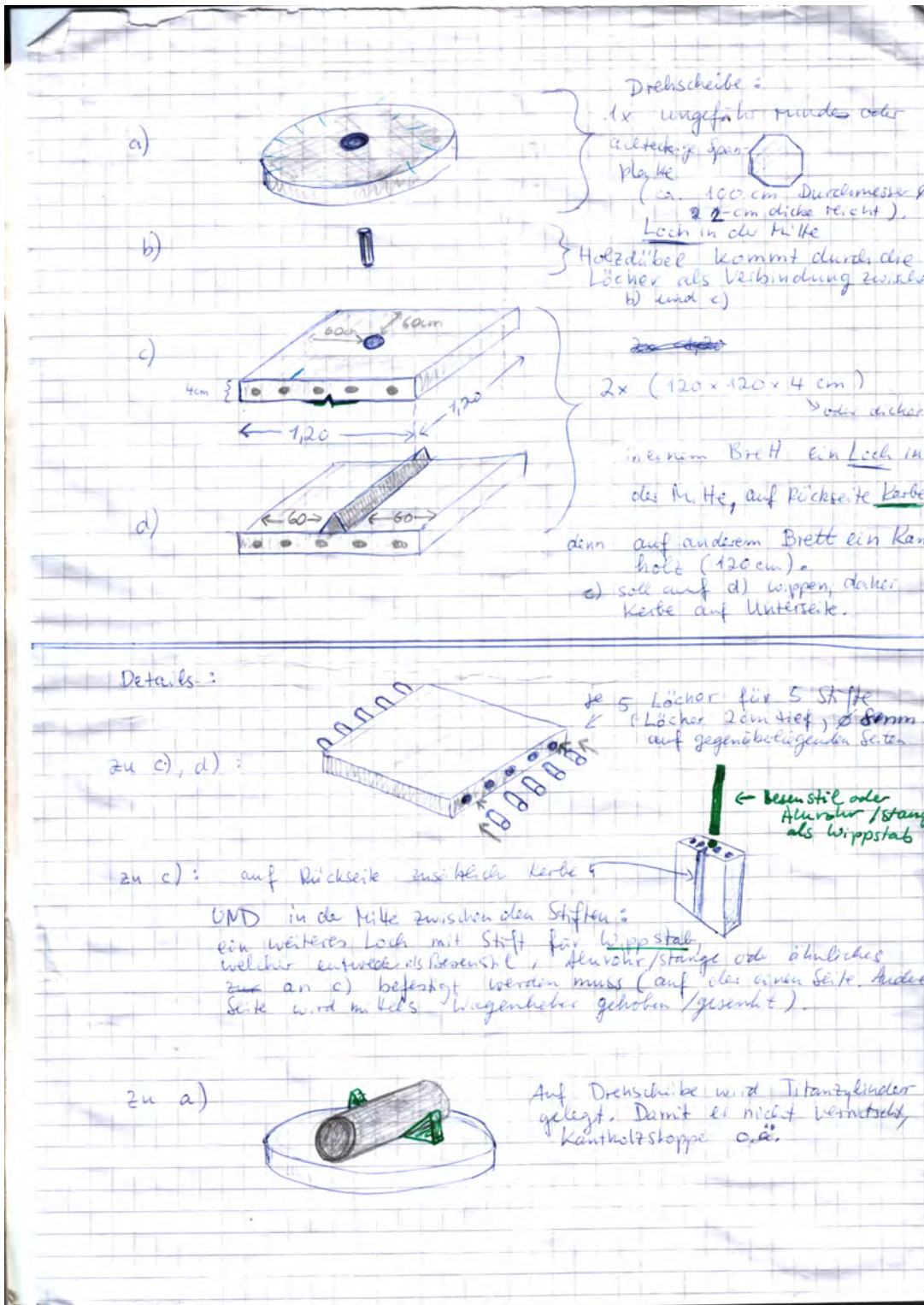


Figure 7.23: Draft of Shaking Apparatus, designed and build by Björn Lewitz.

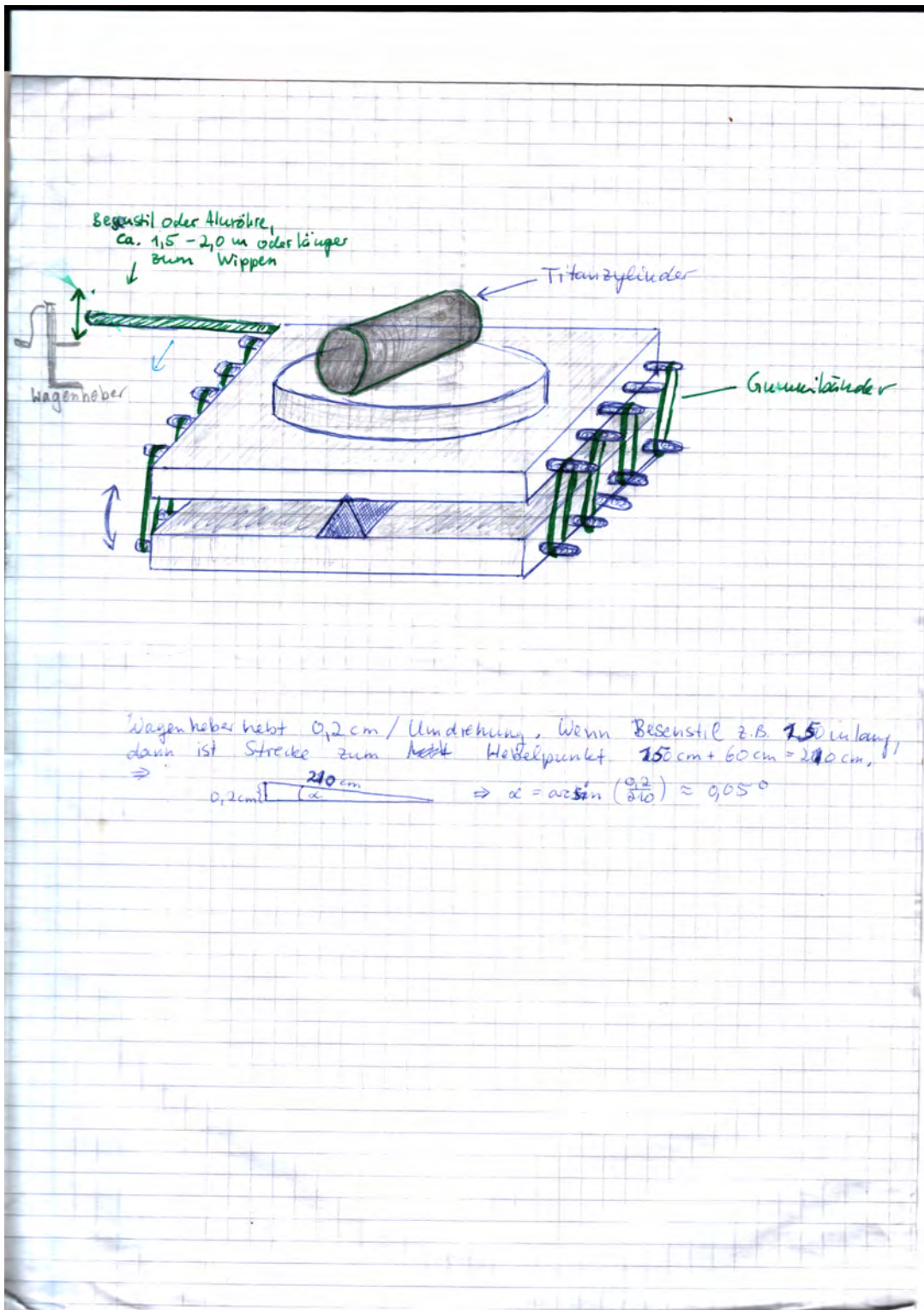


Figure 7.24: Draft of Shaking Apparatus (Continuation).



Lebenslauf

Tamara W. D. Worzewski wurde am 18.01.1979 in Berlin geboren. 1998 erhielt sie ihr Abitur am Schadow-Gymnasium Berlin. Sie begann 1999 das Studium der Geophysik an der Freien Universität (FU) Berlin, wo sie 2001 ihr Vordiplom und 2005 ihr Diplom erhielt. Seit 2006 arbeitet sie im Sonderforschungsbereich 574 am Leibniz Institut für Meereswissenschaften und der Christian-Albrechts-Universität zu Kiel als wissenschaftliche Angestellte. Diese Doktorarbeit entstand aus dieser Tätigkeit.

Privatanschrift:

Harmsstr. 57, 24114 Kiel

Staatsangehörigkeit:

deutsch

Hiermit erkläre ich, dass die vorliegende Abhandlung, abgesehen von der Beratung der Betreuer nach Inhalt und Form, meine eigene Arbeit ist. Bisher ist die Arbeit noch nicht an anderer Stelle im Rahmen eines Prüfungsverfahrens vorgelegt worden. Die Arbeit ist unter Einhaltung der Regeln guter wissenschaftlicher Praxis der Deutschen Forschungsgemeinschaft entstanden.

Tamara W. D. Worzewski